Multiscale modeling of excitations in polymeric systems

Citation for published version (APA):
Bagheri Varnousfaderani, B. (2017). *Multiscale modeling of excitations in polymeric systems*. Technische Universiteit Eindhoven.

Document status and date:
Published: 11/01/2017

Document Version:
Publisher's PDF, also known as Version of Record (includes final page, issue and volume numbers)

Please check the document version of this publication:

• A submitted manuscript is the version of the article upon submission and before peer-review. There can be important differences between the submitted version and the official published version of record. People interested in the research are advised to contact the author for the final version of the publication, or visit the DOI to the publisher's website.
• The final author version and the galley proof are versions of the publication after peer review.
• The final published version features the final layout of the paper including the volume, issue and page numbers.

Link to publication

General rights
Copyright and moral rights for the publications made accessible in the public portal are retained by the authors and/or other copyright owners and it is a condition of accessing publications that users recognise and abide by the legal requirements associated with these rights.

- Users may download and print one copy of any publication from the public portal for the purpose of private study or research.
- You may not further distribute the material or use it for any profit-making activity or commercial gain
- You may freely distribute the URL identifying the publication in the public portal.

If the publication is distributed under the terms of Article 25fa of the Dutch Copyright Act, indicated by the "Taverne" license above, please follow below link for the End User Agreement:

www.tue.nl/taverne

Take down policy
If you believe that this document breaches copyright please contact us at:

openaccess@tue.nl

providing details and we will investigate your claim.

Download date: 31. Aug. 2023

Multiscale Modeling of Excitations in Polymeric Systems

Behnaz Bagheri Varnousfaderani

Cover art: B. Bagheri Varnousfaderani

A catalogue record is available from the Eindhoven University of Technology Library

ISBN: 978-90-386-4195-9

Multiscale Modeling of Excitations in Polymeric Systems

PROEFSCHRIFT

ter verkrijging van de graad van doctor aan de
Technische Universiteit Eindhoven, op gezag van de
rector magnificus prof.dr.ir. F.P.T. Baaijens, voor een
commissie aangewezen door het College voor
Promoties, in het openbaar te verdedigen
op woensdag 11 january 2017 om 16:00 uur

door

Behnaz Bagheri Varnousfaderani

geboren te Khomini Shahr, Iran

Dit proefschrift is goedgekeurd door de promotoren en de samenstelling van de promotiecommissie is als volgt:

voorzitter:	prof.dr. J. de Vlieg
1e promotor:	prof.dr. M.E.J. Karttunen
2e promotor:	dr.Dipl.-Phys. B. Baumeier
leden:	prof.dr. K. Kremer (Johannes Gutenberg Universität Mainz)
	prof.dr. M. Müser (Universität des Saarlandes)
	prof.dr. P.A.J. Hilbers
	dr. C. Storm
	prof.dr. B. Koren

Het onderzoek of ontwerp dat in dit proefschrift wordt beschreven is uitgevoerd in overeenstemming met de TU/e Gedragscode Wetenschapsbeoefening.

To my mother

Contents

Chapter 1

Introduction

The word polymer originates from two Greek words: *poly* meaning *many* and *meres* meaning *parts*. It implies that a polymer consists of a large number of repeating units. Proteins, cellulose, and silk are examples of polymers found in nature, and polystyrene, polyethylene, and nylon are examples of synthetic polymers. Figure 1.1 shows the chemical structure of ethylene and polyethylene. The repeating unit is the CH_2-(methylene-) group and the number of them is called *the degree of polymerization*. The name polyethylene denotes that the polymerization is based on ethylene [1, 3].

The electronic structure of carbon atoms, $1s^2 2s^2 2p^2$, allows for each carbon atom to form four bonds (σ bonds) [4, 5, 6]. Polymers that are built from carbon atoms with four bonds are called *non-conjugated* polymers, such as polyethylene, figure 1.1. Non-conjugated polymers have a large electron band gap, resulting in them being insulators and not optically active. For example, the optical band gap of polyethylene is of the order of 8 eV.

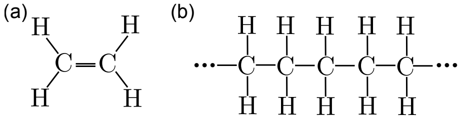

Figure 1.1: (a): ethylene. (b): polyethylene. The repeating unit is the CH_2-(methylene-) group and the number of them is called *the degree of polymerization*. The name polyethylene denotes that the polymerization is based on ethylene. In polyethylene each carbon atom makes four bonds, and hence is a *non-conjugated* polymer [1]. The most common industrial use of polyethylene is in packaging (plastic, plastic bags, ...) [2].

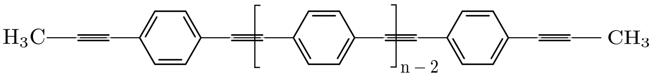

Figure 1.2: Chemical structure of *poly para phenylene ethynylene* (poly-PPE). n is the number of repeat units along the polymer (degree of polymerization). Poly-PPEs are a class of strongly conjugated polymers with a rigid backbone consisting of aromatic phenyl rings bridged by alternating single and triple carbon bonds.

Polymers that have connected π-orbitals with delocalized electrons, and alternating single and multiple bonds are called *conjugated*. The π-overlap network results in the formation of π electronic states extended along the polymer chain. The electronic band gap of conjugated polymers is of the order of 1-4 eV. As such, they exhibit low energy excitations and semiconductor behaviour [4, 5, 6].

Conjugated polymers have attracted a lot of interest due to their variable functional properties and application potential, e.g., in biochemical sensors [7, 8, 9, 10, 11, 12], lasers [13], light emitting diodes (LEDs) [14, 15], organic transistors [16], and photovoltaic devices [17, 18]. The ease of processability and band gap tunability of polymeric semiconductors facilitates the realization of this potential, since it provides the opportunity for targeted manipulation of electronic and morphological properties of single polymer chains and their aggregates. This, in turn, can be achieved by synthetic strategies, exploitation of properties of functional side chains, and/or solvent-induced transitions [19]. One specific example in which both morphological and electro-optical properties of polymers are purposefully modified is highly fluorescent conjugated polymer dots for fluorescence imaging in live cells [20]. Less toxicity together with flexibility and biocompatibility make these *polydots* attractive substitutes for their inorganic counterparts [19, 21].

Among fluorescent polymers, *poly para phenylene ethynylenes* (poly-PPE) (see the chemical structure in figure 1.2) are a class of strongly conjugated polymers with a rigid backbone consisting of aromatic phenyl rings bridged by alternating single and triple carbon bonds. They absorb and emit light in a range from ultraviolet (absorption) to visible (emission) [19]. Poly-PPEs can be prepared in a variety of morphologies, ranging from extended single chains to polydots, depending on the choice of functionalizing side chains and solvent combinations for processing. In particular, poly-PPEs can be used in fluorescence imaging and sensing [20, 19, 21] since their fluorescence intensity is sensitive to the presence of other co-solutes. Due to the significance of polymer conformations for the photophysical properties of functionalized PPEs, it is desirable to steer the tendency of the polymer to stay in single strands or to aggregate in a particular solvent by rational manipulations [22]. It has been shown [19, 21, 22] that modification of side chain functionalization by, e.g., substituting surfactants with varying degree of hydrophobicity and solute-solvent or solvent-air interactions, can lead to controlled morphologies and, concomitantly, optical properties. In flexible and semi-flexible polymers conjugation along a single chain may be broken [23, 24, 25] due to a substantial out-of-plane torsion angle between two adjacent repeat units. However, such a simple criterion may be insufficient to describe and interpret the complex interplay between the actual chemistry of the backbone, functionalization by side chains, solute-solvent interactions and their cumulative effect on the localization characteristics of excitations, and hence, the electronic and optical properties of polymer.

Our goal is to model the optical properties of poly-PPE in complex morphologies [19, 22, 26] using a computational multiscale approach which allows the analysis of the interplay between morphology and electronic excitations.

Upon an external perturbation, a quantum mechanical system is promoted from its ground state (lowest energy state) to an excited state with higher energy. The possible processes of direct and inverse photoemission, as well as absorption are sketched in figure 1.3.

In direct photoemission, by perturbing the system by an incoming photon with energy $h\nu$, an electron at its initial state with energy E_i absorbs the energy, moves to a state with higher energy E_f, and leaves the sample with kinetic energy E_{kin}. The level with energy E_i that was occupied by an electron previously, is called the *hole*. In inverse photoemission, injection of an electron into the sample leads to a photon being released, accompanied by the electron dropping to a lower energy state. In both direct and inverse photoemission the electron can be considered as a free electron separated from the other electrons in the sample. Direct and inverse photoemission spectra can be interpreted as the densities of the occupied and unoccupied states and can be described by employing single particle Schrödinger-like equations with an effective potential. In absorption an electron is excited from an occupied energy level (valence state) to an unoccupied level (conduction state) [27]. Therefore, the excited electron and hole cannot be considered separately and

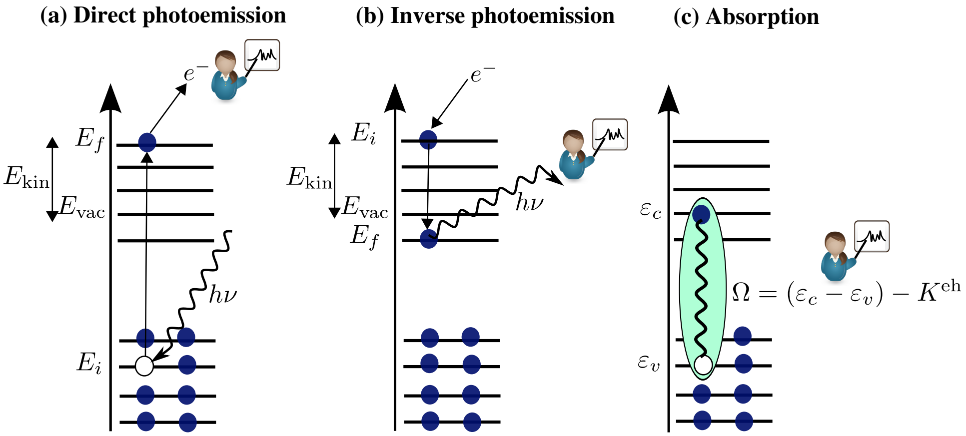

Figure 1.3: Schematic representation of (a) direct photoemission (b) inverse photoemission and (c) absorption in a molecule [27]. E_i is the initial and E_f is the final energy of the electron. E_{vac} is the energy of the free electron at rest. E_{kin} denotes the kinetic energy, ε_c (ε_v) indicates conduction (valence) energy level, and K^{eh} denotes electron-hole interaction.

effective two-particle equations including the interaction between the electron and hole are required to properly describe coupled excitations [27].

In this thesis, multiscale modeling techniques are utilized. On *ab initio* level, the ground state properties of the molecules are well described by *Density Functional Theory* (DFT). The treatment of electronic excitations poses a significant challenge [28, 29, 30, 31, 32, 33, 34, 35, 36]. To describe absorption which involves coupled electron-hole pairs, one needs to go beyond static DFT [27]. One possible approach is to calculate electronically excited states is to couple DFT to *Many-Body Green's Function Theory*. This approach is based on a set of Green's function equations, which contain the nonlocal, energy-dependent electronic self-energy Σ. Starting from an effective one-particle Hamiltonian, such as the *Kohn-Sham* [37, 38] Hamiltonian in DFT as a zero-point solution, Σ can be approximated using Hedin's [39] *GW* approach (*G*: Green's function, *W*: screening potential). Electron-hole interactions can then be captured using the *Bethe-Salpeter* (BSE) equation (*GW*-BSE) [40, 41, 42, 27, 43, 44]. The application of the *GW*-BSE technique has recently received a lot of attention in typical quantum-chemical studies and has been shown to hold advantages over more traditional approaches [45, 42, 46, 47]. This is why in this work [48, 49], the *GW*-BSE method was the method of choice to describe electronic excitations.

After discussing basic polymer theory in *chapter 2*, the many-body problem of electronic structure theory is introduced in *chapter 3* and the conceptual and practical aspects of DFT are summarized. The basics of Green's function theory, Hedin's equations and the *GW* approximation, as well as Bethe-Salpeter equation are explained in *chapter 4*.

For the purpose of designing organic materials with desired optoelectric properties, molecular conformations are an important factor [50, 51]. Due to the very high computational cost of quantum chemical approaches, one inevitably needs to employ *classical* techniques, *molecular mechanics* (MM) or *molecular dynamics* (MD), to obtain the required information about conformational properties. This is particularly the situation for macromolecules, such as solvated polymer chains. Classical techniques use *force fields*, with atoms, or groups of atoms, represented by point masses interacting via empirical potentials.

In order to investigate the effects of morphology, side chains, and solvents on electronic excitations in poly-PPE, strategies are required to couple quantum mechanical techniques to classical environments [52, 53, 54]. In this work, a quantum-classical QM/MM approach based on a combination of *GW*-BSE and a polarizable force field is used to evaluate electronic excitations in solvated poly-PPE with different side chains [48]. Linking *GW*-BSE to a classical environment represented at atomistic resolution by a polarizable force field allows for the determination of optical properties in realistic environments from the self-consistent solution of the coupled QM/MM system. With this new approach, it is possible to disentangle the conformational (as a result of side chain-solvent interactions) and electronic (due to local electric fields and polarization effects) contributions to the absorption spectra. The details of our QM/MM approach is described in *chapter 5*.

In this thesis, the aim is to obtain structural information of solvated poly-PPE using MM/MD techniques and to use the MM/MD geometries for further quantum mechanical calculations of optical excitations. In multiscale simulations the structural descriptions at different levels of resolution must be compatible with each other. For example, bond length deviations or fluctuations in angles and torsions can lead to substantial artifacts if the backmapped/fine-grained geometries do not match the *potential energy surfaces* (PES) of the underlying quantum mechanical system.

Due to the above reasons, existing all-atom force fields may need to be

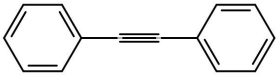

Figure 1.4: Chemical structure of *diphenylethyne* (DPE). It consists of two aromatic rings bridged by a sequence of single bonds and very stiff triple bond.

refined for new compounds. Such a situation regularly arises for conjugated polymers, since conjugation can depend sensitively on conformation. In (semi)flexible polymers, conjugation along a single chain can be broken due to large out-of-plane torsions between two repeat units [23, 24, 25]. In general, details are specific to the backbone chemistry, functionalization by side chains, and solute-solvent interactions. Characteristics of conjugation are also directly influenced by the localization behavior of electronic excitations and hence the electronic and optical properties of the polymer. Some of the underlying challenges related to reconciling atomistic detail between quantum and all-atom resolutions are discussed in *chapter 6*. Due to the importance of backbone torsions in poly-PPE on conjugation and hence excitations, we compare PESs [48] for phenyl rotations in *diphenylethyne* (DPE, see figure 1.4) obtained using DFT to the ones from all-atom simulations using a standard force field and experimental data. Significant discrepancies were found [48] and we discuss the observed discrepancies and their implications in determining of excited state properties using GW-BSE [48]. To eliminate the differences, the atomistic force field needed to be re-parameterized. Furthermore, equilibrium geometries of n-PPE oligomers with $n = 1, 2, \ldots, 10$ were obtained using the modified force field in vacuum. The associated excitation energies using GW-BSE were then benchmarked.

In *chapter 7* our investigations of optical properties of *2,5-dinonyl poly para phenylene ethynylene* oligomers in dilute solutions with toluene and water are discussed. Using our modified force field [48], conformations of 2,5-dinonyl-10-PPE are explored in different solvents with classical MD simulations. Electronic excitations are calculated based on GW-BSE. The results indicate that the electronic environment contributions are negligible compared to the conformation dynamics of the conjugated poly-PPE [49].

In *chapter 8* conformations of 2,5-dinonyl-10-PPE in water are studied using MD simulations. The results show that 2,5-dinonyl-10-PPE exhibits an extended backbone with nonyl side chains aggregated toward the backbone. The backbone exhibits bending. MD simulations of 2,5-diethylhexyl-10-PPE in water show that the backbone forms an extended structure and the ethylhexyl side chains are aggregated toward the backbone. The optical spectra for different structures of 2,5-dinonyl-10-PPE are investigated using our QM/MM techniques and presented in this chapter.

Finally, conclusions and open questions are presented in *chapter 9*.

Chapter 2

Basic polymer concepts

2.1 Introduction

In this chapter we present the basic concepts in polymer physics. We briefly describe the ideal chain models to study the sizes and shapes of polymers in solutions. Some of these concepts are required for the analysis of conformations of polymers in solutions obtained by classical MD in chapter 8. This chapter is based on Refs. [55, 56, 57].

2.2 Polymer conformation

A polymer is a molecule consisting of many repeating units called monomers (chemical monomers), see figure 2.1 and 2.2, that are linked together through covalent bonds. Figure 2.1 shows a schematic representation of a linear polymer using a simple bead and stick model. Each bead represents a monomer connected to its two nearest neighbours (sticks in figure 2.1). Many properties of polymers are determined by their degree of polymerization n, which defines the number of monomers (the number of beads in figure 2.1). The chemical composition of the constituent monomers and the polymer microstructure are important factors in determining their properties. Structurally, polymers are either *homopolymers*, consisting of one type of monomer, or *heteropolymers*, consisting of different types of monomers. Polymers can also have different types of architectures: linear, ring, star-branched, H-branched, comb, ladder, dendrimer, randomly-branched (see figure 2.2), to mention some [55, 56].

Analogously to the secondary structure of proteins, polymers can take different conformations. Conformation is controlled by three factors: the flexibility of the polymer chain, interactions between monomers, and interactions with environment. The strength of these interactions can be changed, for in-

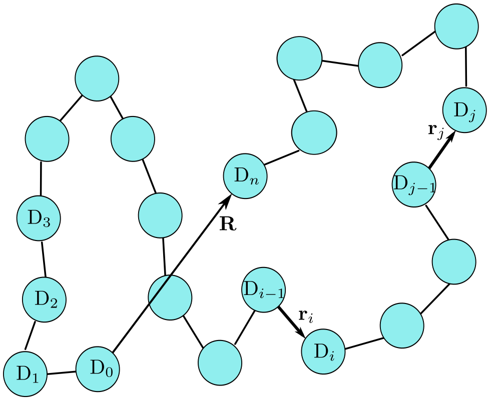

Figure 2.1: The bead and stick model. Each bead represents a monomer that are connected to each other with covalent bonds (sticks).

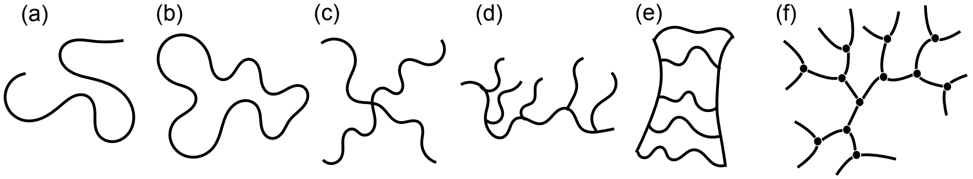

Figure 2.2: Schematic representations of polymer architectures: (a) linear, (b) ring (c) star-branched, (d) comb, (e) ladder, and (f) a dendrimer [55].

stance by temperature, and as a result the conformation of the polymer chain changes.

In order to study polymer conformations, one can start from an ideal chain model. In the ideal chain model there are no interactions between the monomers (see figure 2.1). A polymer is then considered as $n+1$ backbone atoms $\{\mathrm{D}\}$ connected to each other with a bond vector $\{\mathbf{r}\}$. A bond vector $\mathbf{r}_i$ connects atom D_{i-1} to D_i. By summing over all the bond vectors, the end-to-end distance can be measured as

$$\mathbf{R}_n = \sum_i^n \mathbf{r}_i. \tag{2.1}$$

Considering a conformational ensemble, the average end-to-end vector is zero since there is no preferred orientation. However, the mean square end-to-end distance can be calculated as

$$\langle R^2 \rangle = \sum_{i,j=1}^{n} \langle \mathbf{r}_i \cdot \mathbf{r}_j \rangle. \tag{2.2}$$

$\langle R^2 \rangle$ is an important quantity in describing flexibility of polymers. If one considers that all the bond vectors have the same length $l = |\mathbf{r}_i|$ and that the angle between adjacent bond vectors is ξ_{ij}, the mean square end-to-end distance reads

$$\langle R^2 \rangle = \sum_{i,j=1}^{n} \langle \mathbf{r}_i \cdot \mathbf{r}_j \rangle = l^2 \sum_{i,j=1}^{n} \langle \cos{(\xi_{ij})} \rangle. \tag{2.3}$$

Several models based on ideal chains are presented in the following sections. The interactions between monomers that are far apart from each other along the polymer chain are ignored in these models. Each model makes its own particular assumptions about the allowed values of bond angles (ξ) and torsions (ϕ).

The Freely Jointed Chain Model

In the freely jointed chain model the bond length is constant ($l = |\mathbf{r}_i|$) and there are no correlations between the orientations of different bond vectors ($\langle \cos(\theta_{ij}) \rangle = 0$ for $j \neq j$). Therefore

$$\langle R^2 \rangle = nl^2, \tag{2.4}$$

which only includes the n non-zero values for $i = j$.

In a real chain there are correlations between the bond vectors. As such, one can consider that there are no correlations between the bond vectors that are far apart from each other, that is,

$$\lim_{|i-j| \to \infty} \langle \cos(\xi_{ij}) \rangle = 0. \tag{2.5}$$

One can then write eq. 2.3 as

$$\langle R^2 \rangle = C_n nl^2, \tag{2.6}$$

where the coefficient C_n is called *Flory's characteristic ratio* [58], which is the ratio of the end-to-end distance of a real chain to the end-to-end distance of a freely jointed chain with the same number of monomers as the real one. It can be written as [55]

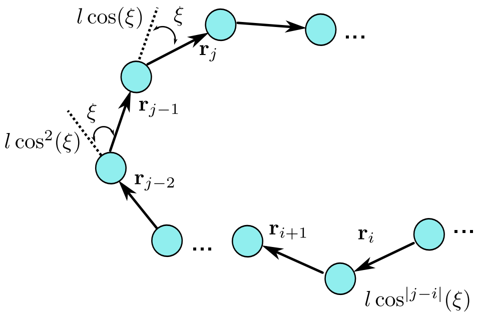

Figure 2.3: Schematic representation of freely rotating chain model. ξ is the bond angle. The correlation between bond vectors $\mathbf{r}_i$ and $\mathbf{r}_j$ that are separated from each other by distance $|i-j|$, is $l^2\cos(\xi)^{|i-j|}$.

$$C_n = \frac{1}{n}\sum_{i=1}^{n}\underbrace{\sum_{j=1}^{n}\langle\cos(\xi_{ij})\rangle}_{C'_i}. \tag{2.7}$$

C'_i is a number defined for any bond vector i. For an infinite chain, $C'_i = C_\infty$ and hence the mean square end-to-end distance for an infinite ideal chain is

$$\langle R^2\rangle \cong C_\infty n l^2. \tag{2.8}$$

Polymers have many universal properties that do not depend on their chemical composition. A simple universal description of all ideal polymers can be given by an *equivalent* freely jointed chain [55]. The mean-square end-to-end distance $\langle R^2\rangle$ and the contour length (maximum end-to-end distance R_{max}) of the *equivalent* freely jointed chain are the same as the real polymer, however, the equivalent freely jointed chain has $N = \frac{R_{max}^2}{C_\infty n l^2}$ effective bonds of length $b = \frac{\langle R^2\rangle}{R_{max}}$. The quantity b is called the *Kuhn length* [59]. The Kuhn length is the length scale that gives the segment size or the effective monomer size. For synthetic polymers the value of Kuhn length is around 1 nm. For DNA it is 100 nm [57]. Persistence length, l_p, describes the length scale in which the polymer chain bends and loses its memory [57]. It is related to b as

$$b = 2l_p. \tag{2.9}$$

The Freely rotating chain model

In the freely rotating chain model all the bond vectors have the same length l but the bond angles between neighbouring bond vectors are fixed (ξ) (see figure 2.3). Different torsion angles are, however, equally probable. As a result, there are correlations between the bond vectors,

$$\langle \mathbf{r}_i \cdot \mathbf{r}_j \rangle = l^2 \cos(\xi)^{|i-j|}. \tag{2.10}$$

By increasing the distance between i and j, $\cos(\xi)^{|i-j|}$ decays rapidly and can be written as

$$\cos(\xi)^{|i-j|} = \exp\Big(- \frac{|i-j|}{s_p} \Big), \tag{2.11}$$

where s_p is the persistence segment [55]

$$s_p = -\frac{1}{\ln(\cos(\xi))}. \tag{2.12}$$

Then, the mean square end-to-end distance can be written as

$$\langle R^2 \rangle = nl^2 \frac{1+\cos(\xi)}{1-\cos(\xi)}. \tag{2.13}$$

By multiplying s_p with the segment length (l), the persistence length can be obtained as

$$l_p \equiv s_p l = -\frac{l_p}{\ln(\cos(\xi))}. \tag{2.14}$$

Worm-like chain model

The freely jointed chain model has no bending rigidity. The Worm-like chain model includes it. It assumes the bond angles ξ to be very small. It is used to describe semi-flexible chains. By expanding $\cos(\xi)$ around $\xi = 0$, the persistence segment can be written as

$$s_p = -\frac{1}{\ln(\cos(\xi))} \cong -\frac{1}{\ln(1-\frac{\xi^2}{2})} \cong \frac{2}{\xi^2}, \tag{2.15}$$

and the *persistence length* l_p can then be obtained as

$$l_p = l s_p \cong \frac{2l}{\xi^2}. \tag{2.16}$$

Due to the addition of bending regidity, the worm-like chain model has a large Flory's characteristic ratio,

$$C_\infty = \frac{1+\cos(\xi)}{1-\cos(\xi)} \cong \frac{1+1-\frac{\xi^2}{2}}{1-1+\frac{\xi^2}{2}} \cong \frac{4}{\xi^2}, \tag{2.17}$$

and its Kuhn length is $b = \frac{\langle R^2 \rangle}{R_{\max}} = \frac{C_\infty n l^2}{R_{\max}} = C_\infty l = 2l_p$. The mean square end-to-end distance for worm-like chain can be written as

$$\langle R^2 \rangle = 2l_p R_{max} - 2l_p^2 \Big(1 - \exp\Big(-\frac{R_{max}}{l_p}\Big)\Big). \tag{2.18}$$

In the limit of a very long worm-like chain ($R_{max} > l_p$), the mean square end-to-end distance can be approximated as $\langle R^2 \rangle \cong bR_{max}$ and in the limit of the chain being much shorter than persistence length ($R_{max} \ll l_p$), it can be approximated as $\langle R^2 \rangle \cong R_{max}^2$.

2.3 Radius of gyration

For a linear chain, the mean square end-to-end distance is a good measure of the size of the polymer. However, for a branched polymer or a ring it is not obvious what the ends are. In this case the radius of gyration can be employed. The radius of gyration can be determined by experimental techniques such as static light scattering, small angle neutron scattering, and/or X-ray scattering. The radius of gyration is defined as the average square distance between the monomers and the center of mass of the polymer $\mathbf{R}_{\text{com}}$ as

$$R_g^2 \equiv \frac{1}{N} \sum_{i=1}^{N} (\mathbf{R} - \mathbf{R}_{\text{com}}). \tag{2.19}$$

This quantity is usually averaged using an ensemble of conformations

$$\langle R_g^2 \rangle \equiv \frac{1}{N} \sum_{i=1}^{N} \langle (\mathbf{R} - \mathbf{R}_{\text{com}}) \rangle. \tag{2.20}$$

For a polymer consisting of identical monomers it can be written as

$$\langle R_g^2 \rangle \equiv \frac{1}{N^2} \sum_{i=1}^{N} \sum_{j=i}^{N} \langle (\mathbf{R}_i - \mathbf{R}_j)^2 \rangle. \tag{2.21}$$

2.3.1 Excluded volume

The aforementioned models are based on the assumption that the interactions between monomers that are far apart along the chain can be neglected. In reality, these monomers interact with each other if they come close together. Each monomer has a volume that other monomers cannot occupy (steric effect). This is referred to as excluded volume. Kuhn [59] and Flory [60] realized that the statistical properties of the chains change by considering excluded volume. As a consequence, $\langle R^2 \rangle$ is proportional to higher values of n

$$\langle R^2 \rangle \propto n^{2\nu}, \tag{2.22}$$

where n is the degree of polymerization and ν is the excluded volume parameter. Theoretical modelling of excluded volume chains is complicated due to the inclusion of steric effects, van der Waals interactions, and interactions with solvent. Historically, P. G. de Gennes (1972) [61] used renormalization group to include excluded volume effects. However, even with computer simulations modelling non-ideal chains remains a challenge [62].

2.4 Thermodynamics of polymers in solutions

In the previous section the excluded volume interaction ($\varepsilon_{\mathrm{ev}}$) was briefly discussed. This interaction depends on the type of polymer chain and the solvent [57]. Depending on temperature, this interaction can make the polymer either to be dispersed ($\varepsilon_{\mathrm{ev}} \ll k_{\mathrm{B}}T$, excluded volume effect) or collapsed ($\varepsilon_{\mathrm{ev}} \gg k_{\mathrm{B}}T$). Different kinds of solvents exist for a polymer. If the solvent dissolves the polymer well it is called a *good solvent*. This effect is similar to swelling of polymer chain due to excluded volume effect at high temperatures. If the solvent does not dissolve the polymer it is called a *nonsolvent*, *poor solvent* or *bad solvent*.

There is a temperature, at which the repulsive and attractive interactions cancel out and the polymer chain behaves like an ideal chain. This temperature is called the Θ-temperature. If $T > \Theta$ the polymer chain swells like in a good solvent. If $\Theta < T$, the chain shrinks as in a bad solvent [57, 63, 55]. Polymer solutions in good solvent are examples of *homogeneous* mixtures. If the mixture includes several different regions with different composition is called a *heterogeneous* mixture [55, 56].

Considering a polymer solution, the properties of the mixture and its thermodynamics depend on the quality of the solvent and the interactions between the solvent and the polymer. The competition between entropy and energy determines whether the equilibrated solution is homogeneous or heterogeneous. These properties can be described within the *mean-field lattice model of Flory-Huggins* [64, 65].

In this model two species with volume fraction Φ (for polymer chain) and $(1-\Phi)$ (for solvent) are considered. By assuming that there is no volume change upon mixing the two species, the entropy of mixing can be obtained by counting the number of microstates on a lattice. The average pairwise energy interaction of mixing in constant volume can be calculated by the interaction between neighbouring lattice sites. Finally, the free energy ($\Delta F_{\text{mix}} = \Delta E_{\text{mix}} - T\Delta S_{\text{mix}}$) reads [55, 56]

$$\Delta F_{\text{mix}} = k_{\text{B}}T\Big[\frac{\Phi}{n}\ln(\Phi) + (1-\Phi)\ln(1-\Phi) + \chi\Phi(1-\Phi)\Big], \tag{2.23}$$

where n is the number of monomers in the polymer chain. The first two terms in eq. 2.23 have an entropic origin and the last term is due to the energy of mixing. χ is the Flory-Huggins parameter which characterizes the difference of interaction energies of the two species in the mixture. $\chi < 0$ ($\chi > 0$), means that there is a net attractive (repulsive) interaction between the solvent and polymer. In case of net zero interaction, the Θ-solvent (Θ defines the temperature that the net interaction is zero). For a detailed derivation of the free energy of mixing, please see Ref. [55, 56].

In the Flory-Huggins theory, the volume does not change by mixing species. However, in real polymers volume changes. This effect and other deviations from the lattice model can be added to the χ parameter. χ depends on polymer compositions, chain lengths, and temperature [55]. The temperature dependence of χ can be written empirically, as a sum of temperature independent entropic part and temperature dependent enthalpic part as

$$\chi(T) \cong A + \frac{B}{T}. \tag{2.24}$$

The parameters A and B are weakly depend on the lengths of the chains and their compositions [55].

2.5 Polymer dynamics

Considering a small particle in a liquid, the velocity $\mathbf{v}$ of the particle under an applied force $\mathbf{f}$ reads as

$$\mathbf{f} = \zeta\mathbf{v}, \tag{2.25}$$

where ζ is the *friction coefficient*. The *Einstein relation* gives the relation between the friction (ζ) and the diffusion (D) coefficients of the particle,

$$D = \frac{k_{\mathrm{B}}T}{\zeta}. \tag{2.26}$$

If the size of the particle is R, then the time τ that it takes for the particle to move a distance of R is proportional to the friction coefficient,

$$\tau \approx \frac{R^2}{D} \approx \frac{R^2}{k_{\mathrm{B}}T}. \tag{2.27}$$

If the particle is spherical and has radius R and it moves in a *Newtonian liquid* (the stress σ is proportional to the shear rate $\dot{\gamma}$, $\sigma = \eta\dot{\gamma}$, η is viscosity coefficient), the relation between the friction coefficient and the viscosity and radius of sphere is given by *Stokes' law*

$$\eta = 6\pi\eta R. \tag{2.28}$$

The *Stokes-Einstein relation* then gives the diffusion coefficient as

$$D = \frac{k_{\mathrm{B}}T}{6\pi\eta R}. \tag{2.29}$$

The Stokes-Einstein relation can be employed in order to determine the size of a spherical particle R from the measured diffusion coefficient D. The measured size is called the *hydrodynamic radius* [55]. The aforementioned calculation is for a particle moving in a liquid.

Rouse model

Rouse [66] developed the first model for the dynamics of polymers in implicit solvent, using a bead and spring model (see figure 2.4). In this model, the polymer chain is represented by n beads which are interacting with each other by springs. Each bead has a friction coefficient ζ independent from others, and the total Rouse chain friction coefficient ζ_{R} can be given as

$$\zeta_{\mathrm{R}} = n\zeta. \tag{2.30}$$

Using Einstein relation, the diffusion coefficient of the Rouse chain is given as

$$D_{\mathrm{R}} = \frac{k_{\mathrm{B}}T}{n\zeta}. \tag{2.31}$$

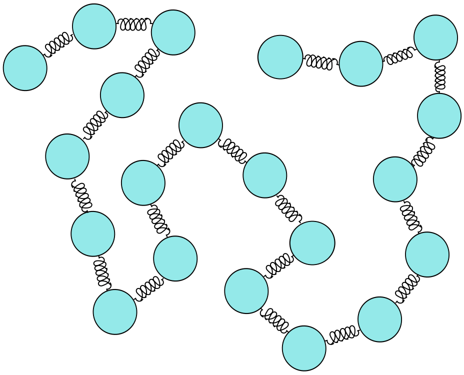

Figure 2.4: A bead and spring model. The polymer chain is represented by n beads, which are interacting with each other by springs with root-mean-square size of l.

The *Rouse time*, τ_R, is defined as the time that the polymer moves a distance of the order of its size R is:

$$\tau_{\mathrm{R}} \approx \frac{R^2}{D_{\mathrm{R}}} = \frac{\zeta n R^2}{k_{\mathrm{B}} T}. \tag{2.32}$$

From the scaling argument the size of a polymer chain is:

$$\langle R^2 \rangle \approx l n^{\nu}.$$

where ν is the scaling exponent [63]. For an ideal linear chain $\nu = \frac{1}{2}$. The Rouse time can then be written as [55]

$$\tau_{\mathrm{R}} \approx \frac{\zeta l^2 n^{1+2\nu}}{k_{\mathrm{B}} T}, \tag{2.33}$$

and the time scale for movement of each bead in polymer chain, the *Kuhn monomer relaxation time*, [55] is

$$\tau_0 \approx \frac{\zeta b^2}{6\pi^2 k_{\mathrm{B}} T} n^2. \tag{2.34}$$

The polymer does not move at time scales smaller than τ_0 (elastic response), and it exhibits a diffusive motion on time scales longer than τ_{R}. $\tau_0 < t < \tau_{\mathrm{R}}$, is the viscoelastic response regime [55].

The Rouse model disregards *hydrodynamic interactions* due to the movement of the other beads and it assumes that the beads interact with each other only via connecting springs.

Zimm model

The Zimm [67] model includes hydrodynamic interactions between the monomers. They are important for polymers in dilute solutions. The Zimm diffusion coefficient is given as

$$D_{\mathrm{Z}} \approx \frac{k_{\mathrm{B}}T}{\eta_s l n^{\nu}}. \tag{2.35}$$

The *Zimm time*, τ_{Z}

$$\tau_{\mathrm{Z}} \approx \tau_0 n^{3\nu}, \tag{2.36}$$

is different from the one provided by the simpler Rouse model, eq. 2.33.

Chapter 3

Density Functional Theory

3.1 Introduction

Understanding of many-body interacting system of electrons and nuclei requires electronic structure methods such as *Density Functional Theory* for the description of electronic and structural properties of systems. This chapter introduces the many-body particle Hamiltonian of a system of interacting electrons and nuclei and reviews the essential definitions and formulations that yield the single particle *Kohn-Sham* equations. For detailed description, see Refs. [68, 69, 70, 71].

3.2 The Many-Body Hamiltonian

The question of how to describe a system of many-body interacting electrons traces back to decades ago [38, 37]. The difficulty is not because the related equations of motions are not known, but in how to solve them. The non-relativistic Hamiltonian of a system of interacting electrons and nuclei can be written as

$$\begin{aligned} \hat{H} &= \sum_{I=1}^{N_\mathrm{n}} \frac{\hat{\mathbf{P}}_I^2}{2M_I} + \frac{1}{2}\sum_{I=1}^{N_\mathrm{n}} \sum_{\substack{I'=1 \\ I'\neq I}}^{N_\mathrm{n}} \frac{Z_I Z_{I'} e^2}{|\mathbf{R}_I - \mathbf{R}_{I'}|} \\ &+ \sum_{i=1}^{N} \frac{\hat{\mathbf{p}}_i^2}{2m_i} + \frac{1}{2}\sum_{i=1}^{N} \sum_{\substack{j=1 \\ j\neq i}}^{N} \frac{e^2}{|\mathbf{r}_i - \mathbf{r}_j|} - \sum_{i=1}^{N} \sum_{I=1}^{N_\mathrm{n}} \frac{Z_I e^2}{|\mathbf{r}_i - \mathbf{R}_I|} \qquad (3.1) \\ &= \underbrace{\hat{T}_\mathrm{n} + \hat{V}_\mathrm{nn}}_{\hat{H}_\mathrm{n}} + \underbrace{\hat{T}_\mathrm{e} + \hat{V}_\mathrm{ee} + \hat{V}_\mathrm{en}}_{\hat{H}_\mathrm{el}} . \end{aligned}$$

The system consists of N_n atomic nuclei with mass M_I and charge Z_I at positions $\mathbf{R}_I$ and N electrons with mass m and charge $-e$ ($e > 0$) at positions $\mathbf{r}_i$. Index I runs over nuclei and i over electrons. In eq. 3.2 , $\hat{T}_\mathrm{n}$ ($\hat{T}_\mathrm{e}$) is the kinetic energy of the nuclei (electrons). $\hat{V}_\mathrm{nn}$ ($\hat{V}_\mathrm{ee}$) is the internuclear (interelectronic) Coulomb repulsions. $\hat{V}_\mathrm{en}$ is the electron-nuclear Coulomb interaction.

The obstacle is how to solve the time-independent Schrödinger equation for a system of $N + N_\mathrm{n}$ interacting particles in which the number of electrons and nuclei is of the order of Avogadro's number $\sim 10^{23}$:

$$[\hat{H}_\mathrm{n} + \hat{H}_\mathrm{el}]\Psi(\{\mathbf{r}\},\{\mathbf{R}\}) = E\Psi(\{\mathbf{r}\},\{\mathbf{R}\}). \tag{3.2}$$

where E is the eigenvalue and $\Psi(\{\mathbf{r}\},\{\mathbf{R}\})$ is the eigenfunction of the coupled electronic-nuclear system which is a function of all electronic ($\{\mathbf{r}\} = \mathbf{r}_1, \mathbf{r}_2, \ldots, \mathbf{r}_N$) and nuclear ($\{\mathbf{R}\} = \mathbf{R}_1, \mathbf{R}_2, \ldots, \mathbf{R}_{N_\mathrm{n}}$) variables. E gives the total energy of the system and $\Psi(\{\mathbf{r}\},\{\mathbf{R}\})$ yields the electron distribution.

One way out of this dilemma is to simplify the Hamiltonian [68, 69, 70, 71].

3.3 Born-Oppenheimer approximation

Since the masses of electrons (m_i) are much less than the masses of nuclei (M_I), $\frac{m_i}{M_I} \sim \mathcal{O}(10^{-4} - 10^{-5})$, electrons move much faster than nuclei and they quickly *adjust* to any nuclear displacement. This is the basis of the so-called *Born-Oppenheimer approximation* [72]. As such, one can separate the electronic and nuclear motions. Within this approximation, the inverse mass of a nucleus ($\frac{1}{M_I}$) can be considered as a small perturbation parameter and one can perform a perturbation series with respect to $\frac{1}{M_I}$. As a consequence, the nuclear kinetic energy ($\hat{T}_\mathrm{n} = -\sum_I \frac{\hbar^2}{2M_I}\nabla_I^2$) and the nuclear-nuclear potential (V_nn) can be taken independent of the electrons. Hence, they can be considered fixed during the motion of electrons. Therefore, the Schrödinger equation for electrons can be written as:

$$\hat{H}_\mathrm{el}\Psi_\mathrm{el}(\{\mathbf{r}\};\{\mathbf{R}\}) = E_\mathrm{el}\Psi_\mathrm{el}(\{\mathbf{r}\};\{\mathbf{R}\}). \tag{3.3}$$

where nuclear coordinates $\{\mathbf{R}\}$ can be considered as *fixed parameters* of the Hamiltonian for the electronic system. E_el is eigenvalue of the electronic Schrödinger equation and is called the *electronic energy* [68, 69, 70, 71]. The electronic Hamiltonian of the system $\hat{H}_\mathrm{el}$ is:

$$\hat{H}_\mathrm{el} = \hat{T}_\mathrm{e} + \hat{V}_\mathrm{ext} + \hat{V}_\mathrm{int}, \tag{3.4}$$

in which $\hat{T}_e$, $\hat{V}_{\text{ext}}$, and $\hat{V}_{\text{int}}$ are:

$$\hat{T}_{\text{e}} = \sum_i -\frac{\hbar^2}{2m}\nabla_i^2, \tag{3.5}$$

$$\hat{V}_{\text{ext}} = \hat{V}_{\text{en}} = -\sum_{i=1}^{N}\sum_{I=1}^{N_n}\frac{Z_I e^2}{|\mathbf{r}_i - \mathbf{R}_I|}, \tag{3.6}$$

$$\hat{V}_{\text{int}} = \hat{V}_{\text{ee}} = \frac{1}{2}\sum_{i=1}^{N}\sum_{\substack{j=1 \\ j\neq i}}^{N}\frac{e^2}{|\mathbf{r}_i - \mathbf{r}_j|}, \tag{3.7}$$

From now on, we use Hartree atomic units $\hbar = m = e = \frac{4\pi}{\epsilon_0} = 1$.

3.4 Kohn-Sham Equations

The electronic Schrödinger equation within the Born-Oppenheimer approximation, eq. 3.3 is not exactly solvable because of electron-electron interactions. Several quantum chemistry approaches have been proposed in order to solve it. Methods include Hartree [73], Hartee-Fock [74], configuration interaction [75] method, variational Monte Carlo [76, 77], etc. which are based on optimizing many-body wave-functions. These methods severely suffer from the dimensionality bottleneck as the computational cost grows as $\sim N^{4-6}$ with system size N. Furthermore, exchange and electron correlations are not considered in the Hartree method. Electron correlations are not included in Hartree-Fock method, however, the exchange effects are included in terms of a single Slater determinant to account for the Pauli exclusion principle. All these approaches aim to predict and explain experimental measurements and, therefore, one needs to calculate the expectation values of observables. For this the knowledge of the full wave-function is not mandatory [68, 69, 70, 71].

DFT is based on the original works of Hohenberg and Kohn [38, 37] in which they indicate that all the information of the correlated many-body system can be described as a functional of the ground state density. The Hohenberg-Kohn theorems [38, 37] for a system of N interacting fermions are the following:

1. There is a one-to-one correspondence between the ground state density $n_0(\mathbf{r})$ and external potential $V_{\text{ext}}(\mathbf{r})$ applied to a system of interacting fermions.

2. The energy of a system of interacting particles is a universal functional of its density $n(\mathbf{r})$, $E[n(\mathbf{r})]$, and the exact ground state energy of the

system is the global minimum of this energy functional.

According to the second theorem there is a variational principle acting on density. The ground state density in terms of the ground state wave-function of an N-electronic system $\Psi_0(\mathbf{r}_1, \mathbf{r}_2, ..., \mathbf{r}_N)$ is given by

$$n(\mathbf{r}) = N \int d\mathbf{r}_2 ... d\mathbf{r}_N |\Psi_0(\mathbf{r}, \mathbf{r}_2, ..., \mathbf{r}_N)|^2. \tag{3.8}$$

where N is the number of electrons. In order to find the functional form of the total energy in terms of density one can start to take out the parts that have obvious functional form and try to make the unknown parts as small as possible. As such, the total ground state energy can be written in terms of ground state density as

$$\begin{aligned} E[n(\mathbf{r})] &= \langle\Psi_0| H |\Psi_0\rangle && (3.9) \\ &= \langle\Psi_0| \hat{T}_\mathrm{e} |\Psi_0\rangle + \langle\Psi_0| \hat{V}_\mathrm{int} |\Psi_0\rangle + \int d\mathbf{r}\ V_\mathrm{ext}(\mathbf{r}) n(\mathbf{r}). && (3.10) \end{aligned}$$

The electron-electron Coulomb interaction (V_int or V_ee) can be written in terms of the known Hartree part (V_H) and an unkown term called exchange-correlation term ($E_\mathrm{xc}[n(\mathbf{r})]$). Subsequently, one can rewrite eq. 3.10 as

$$\begin{aligned} E[n(\mathbf{r})] &= \langle\Psi_0| \hat{T}_\mathrm{e} |\Psi_0\rangle + E_\mathrm{H} + E_\mathrm{xc}[n(\mathbf{r})] + \int d\mathbf{r}\ V_\mathrm{ext}(\mathbf{r}) n(\mathbf{r}) && (3.11a) \\ &= \langle\Psi_0| \hat{T}_e |\Psi_0\rangle + \frac{1}{2} \int d\mathbf{r} d\mathbf{r}'\ \frac{n(\mathbf{r}) n(\mathbf{r}')}{|\mathbf{r} - \mathbf{r}'|} + E_\mathrm{xc}[n(\mathbf{r})] \\ &+ \int d\mathbf{r}\ V_\mathrm{ext}(\mathbf{r}) n(\mathbf{r}). && (3.11b) \end{aligned}$$

In eq. 3.11b the unknown terms are kinetic energy functional ($\langle\Psi_0| \hat{T}_\mathrm{e} |\Psi_0\rangle$) and the exchange-correlation functional ($E_\mathrm{xc}[n(\mathbf{r})]$).

In order to find the functional form of kinetic energy, Kohn and Sham [37] offered a procedure in 1965 that replaces the original interacting many electron problem with a system of independent auxiliary electrons subjected to an effective potential called the Kohn-Sham potential (V_KS) in a way that the ground state density of the original interacting system is equal to that of non-interacting one. In this way, one can write the kinetic energy term in terms of auxiliary single particle wave functions ($\phi_i(\mathbf{r})$) of the non-interacting system:

$$T_0 = \sum_{i=1}^{N} \int d\mathbf{r} \phi_i(\mathbf{r})^* \frac{-\nabla_\mathbf{r}^2}{2} \phi_i(\mathbf{r}), \tag{3.12}$$

and the correlation part of kinetic energy can be added to the unknown exchange-correlation term (E_{xc}).

The Kohn-Sham (KS) energy functional is written as:

$$\begin{aligned} E[n(\mathbf{r})] = T_0[n(\mathbf{r})] + \int d\mathbf{r}\ n(\mathbf{r})V_{\text{ext}}(\mathbf{r}) \\ + \frac{1}{2}\int d\mathbf{r}d\mathbf{r}^{'}\ \frac{n(\mathbf{r})n(\mathbf{r}^{'})}{|\mathbf{r}-\mathbf{r}^{'}|} + E_{\text{xc}}[n(\mathbf{r})], \end{aligned} \tag{3.13a}$$

where $n(\mathbf{r})$ is the total electron density of the system which can be written in terms of single-particle wave-functions $\phi_i(\mathbf{r})$ as

$$n(\mathbf{r}) = \sum_{i=1}^{N} |\phi_i(\mathbf{r})|^2. \tag{3.14}$$

By variation of the total energy functional $E[n(\mathbf{r})]$ with respect to density $n(\mathbf{r})$ at a fixed particle number N and by using eq. 3.14 one can obtain the Euler equations of a system of non-interacting particles, the *Kohn-Sham equations*:

$$\Big\{-\frac{\nabla^2}{2} + \int d\mathbf{r}^{'}\frac{n(\mathbf{r}^{'})}{|\mathbf{r}-\mathbf{r}^{'}|} + V_{\text{ext}}(\mathbf{r}) + V_{\text{xc}}(\mathbf{r})\Big\}\phi_i(\mathbf{r}) = \varepsilon_i\phi_i(\mathbf{r}) \tag{3.15a}$$

$$\underbrace{\Big\{-\frac{\nabla^2}{2} + \underbrace{[V_{\text{H}} + V_{\text{ext}}(\mathbf{r}) + V_{\text{xc}}(\mathbf{r})]}_{V_{\text{KS}}}\Big\}}_{H_{\text{KS}}}\phi_i(\mathbf{r}) = \varepsilon_i\phi_i(\mathbf{r}), \tag{3.15b}$$

where ε_i is the Lagrange multiplier coming from the normalization of the single-particle wave function as a constraint. By obtaining eq. 3.15 the original many-particle equation is transformed to a system of N single particle equations. All effects due to exchange of electrons and electron correlations are included in the exchange-correlation potential $V_{\text{xc}}(\mathbf{r})$ in eq. 3.15:

$$V_{\text{xc}}[n(\mathbf{r})] = \frac{\delta E_{\text{xc}}[n(\mathbf{r})]}{\delta n(\mathbf{r})}. \tag{3.16}$$

H_{KS} in eq. 3.15 is the Kohn-Sham Hamiltonian and V_{KS} the Kohn-Sham potential. If one knows the exact form of exchange-correlation (xc) functional the mapping is exact. However, there is no exact expression for exchange-correlation potential and therefore approximation needs to be used for it [68, 69, 70, 71].

3.5 Exchange Correlation Functional

The simplest approximation one can make for exchange correlation part is the *Local Density Approximation* (LDA) which was described in seminal paper of Kohn and Sham [37]. Energy of a system of non-interacting electrons (electron gas) at position $\mathbf{r}$ and density $n(\mathbf{r})$ can be approximated by the energy of a homogeneous electron gas having the same density as the electron gas at position $\mathbf{r}$

$$E_{\text{xc}}^{\text{LDA}}[n(\mathbf{r})] = \int d\mathbf{r}\; n(\mathbf{r})\varepsilon_{\text{xc}}^{\text{hom}}(n(\mathbf{r})), \tag{3.17}$$

in which $\varepsilon_{\text{xc}}^{\text{hom}}(n(\mathbf{r}))$ is the energy of homogeneous electron gas with density $n(\mathbf{r})$ at position $\mathbf{r}$ [37, 78].

In LDA the system is considered to be homogeneous. This makes it a good approximation for systems such as metals and *sp*-bonded semiconductors, in which electronic density changes slowly [79]. For atoms and small molecules and systems where the gradient of the electronic density is not small, LDA overestimates binding energies and bond lengths [69]. In order to consider inhomogeneities in the system, it is reasonable to consider derivatives of density in the exchange correlation functional. In the Generalized Gradient Approximation (GGA) [80, 81], the exchange correlation functional is assumed to be a functional of density ($n(\mathbf{r})$) and its gradient ($\nabla n(\mathbf{r})$). GGA gives better agreement with experimental structural parameters for this kind of systems [82]. GGA can be extended by considering higher derivatives of density. The Meta-GGA approximation [83, 84] accounts for $\nabla^2 n(\mathbf{r})$. Meta-GGA is computationally expensive and is not widely used [68, 69, 70, 71].

Another form of functionals can be constructed by combining a portion of exchange energy from the Hartree-Fock and other approximations [85, 86]. These are the most accurate functionals available to the chemistry community so far [69]. There are other functionals, such as the self-interaction corrected functionals [87] where non-local corrections that reduce the self-interaction error of local functionals are introduced [68, 69, 70, 71].

3.6 Density Functional Theory in Practice

3.6.1 Norm-conserving pseudopotential

There is another term in the KS Hamiltonian which includes the electron-nuclear Coulomb interactions and this is $V_{\text{ext}}(\mathbf{r})$. Electron-nuclear Coulomb interactions are singular near the nuclear core. However, core electrons are localized around each atom and they have a weak interaction with the core electrons of other atoms. Therefore, the external potential generated by the core electrons behave like a nucleus core. One can replace the external potential of the original all electron problem, including those of nucleus and the core electrons by a smooth non-singular potential known as *pseudopotential* which only acts on the valence electrons. Then, the Kohn-Sham calculations become limited to valence electrons

$$\Big\{-\frac{\nabla^2}{2}+V_{\text{eff}}^{\text{ps}}([n^{\text{ps}}],\mathbf{r})\Big\}\phi_i^{\text{ps}}(\mathbf{r})=\varepsilon_i\phi_i^{\text{ps}}(\mathbf{r}). \tag{3.18}$$

where ϕ_i^{ps} are the pseudo wave-functions with effective screened pseuodopotential

$$V_{\text{eff}}^{\text{ps}}=V_{\text{n}}^{\text{ps}}(\mathbf{r})+V_{\text{H}}^{\text{ps}}([n^{\text{ps}}],\mathbf{r})+V_{\text{xc}}^{\text{ps}}([n^{\text{ps}}],\mathbf{r}), \tag{3.19}$$

Once core electrons are removed, pseudo wave-functions are nodeless in the core region (no zero in the core region) and outside that region the pseudopotential and pseudo wave-functions are the same as the all-electron ones. An empirical or a semi-empirical pseudopotential is based on fitting the effective potential or its ionic components to empirical data and is not transferable to different chemical environments. *Norm conserving* pseudopotential is a set of *ab initio* pseudopotential that are not fitted to experimental data and are transferable. Such a pseudopotential is constructed to satisfy the following conditions [69]:

1. The eigenvalues resulting from the pseudopotential are identical to the all-electron eigenvalues.

2. Outside a cut-off region the pseudopotential is equal to the all-electron potential.

3. Outside the cut-off region the pseudo wave-function is the same as the all-electron one. At the cut-off the logarithmic derivatives of pseudo wave-function and the all electron one is the same.

4. Inside the cut-off region the charge from pseudopotential calculations and all-electron calculations coincide.

The cut-off region controls the accuracy of the pseudopotential. The pseudopotential is more transferable if the cut-off is smaller [69].

By removing the core electrons a considerable part of total energy is disregarded and hence only differences in total energy due to the valence charge readjustment are meaningful in pseudopotential calculations [68, 69, 88].

3.6.2 Basis sets

By choosing the appropriate exchange-correlation functional and pseudopotential, H_{KS} is defined and one can solve the Kohn-Sham equations numerically. For this purpose one needs to use a set of basis functions in order to represent the single-particle wave-functions. The basis functions are chosen depending on several factors, e.g. ease of implementation, computational cost, precision and geometry of the system [88]. In general the basis sets are either localized in $\mathbf{k}$ space, like the plane-wave basis, or localized in real space. In this work [48, 49], we employed Gaussian basis sets. Accordingly, we restrict our discussion to Gaussian basis sets.

Gaussian functions are localized in Fourier space and real space. Gaussian orbitals either can be given in polar coordinates or Cartesian coordinates as

$$\begin{aligned} \chi_{n,l,m}(r,\theta,\phi) &= \chi_\nu(r,\theta,\phi) = N Y_{lm}(\theta,\phi) r^{2n-2-l} e^{-\zeta_\nu r^2} && (3.20) \\ \chi_{l_x,l_y,l_z}(x,y,z) &= \chi_\nu(x,y,z) = N x^{l_x} y^{l_y} z^{l_z} e^{-\zeta_\nu r^2} && (3.21) \end{aligned}$$

The type of orbital is defined by the sum of $l_x + l_y + l_z$. The index $\nu \equiv l, m$ indicates different symmetries of the orbitals. By expanding the Kohn-Sham wave-function in terms of $\{\chi_\nu\}$ localized at each atomic position $\mathbf{R}_\mu$, we have

$$\phi_i^{\mathrm{KS}} = \sum_{\nu\mu} c^i_{\nu\mu} \chi_\nu(\mathbf{r} - \mathbf{R}_\mu). \tag{3.22}$$

A minimum basis set is the smallest number of functions. For example, for Hydrogen it involves one s orbital.

Employing eq. 3.22 into Kohn-Sham equation, it converts to

$$\sum_{\nu\mu} c^i_{\nu\mu} [H_{\nu\mu\nu'\mu'} - \varepsilon_i S_{\nu\mu\nu'\mu'}] = 0. \tag{3.23}$$

and the matrix elements of the Hamiltonian are

$$H_{\nu\mu\nu'\mu'} = \int d\mathbf{r}\chi_{\nu}^{*}(\mathbf{r}-\mathbf{R}_{\mu})[-\frac{\nabla^2}{2} + V_{\text{eff}}^{\text{ps}}([n^{\text{ps}}],\mathbf{r})]\chi_{\nu'}(\mathbf{r}-\mathbf{R}_{\mu'}), \tag{3.24}$$

and

$$S_{\nu\mu\nu'\mu'} = \int d\mathbf{r}\chi_{\nu}^{*}(\mathbf{r}-\mathbf{R}_{\mu})\chi_{\nu'}(\mathbf{r}-\mathbf{R}_{\mu'}), \tag{3.25}$$

is the overlap matrix. Equation 3.23 is a general eigenvalue problem with a symmetric matrix $(\mathbf{H} - \varepsilon\mathbf{S})$. This can be solved using standard numerical techniques.

The Kohn-Sham Hamiltonian in eq. 3.15 depends on its own solution through density. Hence, it is a non-linear eigenvalue problem which needs to be solved self-consistently [68, 69, 88], figure 3.1. The procedure involves updating V_{eff} (eq. 3.19) and electronic density $n(\mathbf{r})$ successively until self-consistency is achieved. Initial density is computed using the initial configuration. Employing Poisson's equation, the Hartree potential V_{H} is calculated. Having chosen the exchange-correlation potential V_{xc}, the matrix elements $H_{\nu\mu}$ and $S_{\nu\mu}$ can be evaluated using eq. 3.24 and eq. 3.25. Solving the eigenvalue problem eq. 3.23 leads the single particle eigenvalues and eigenfunctions. The new electron density is computed using eigenfunctions of eq. 3.23 and is used for the next iteration. This procedure iterates until the self-consistency criterion is satisfied.

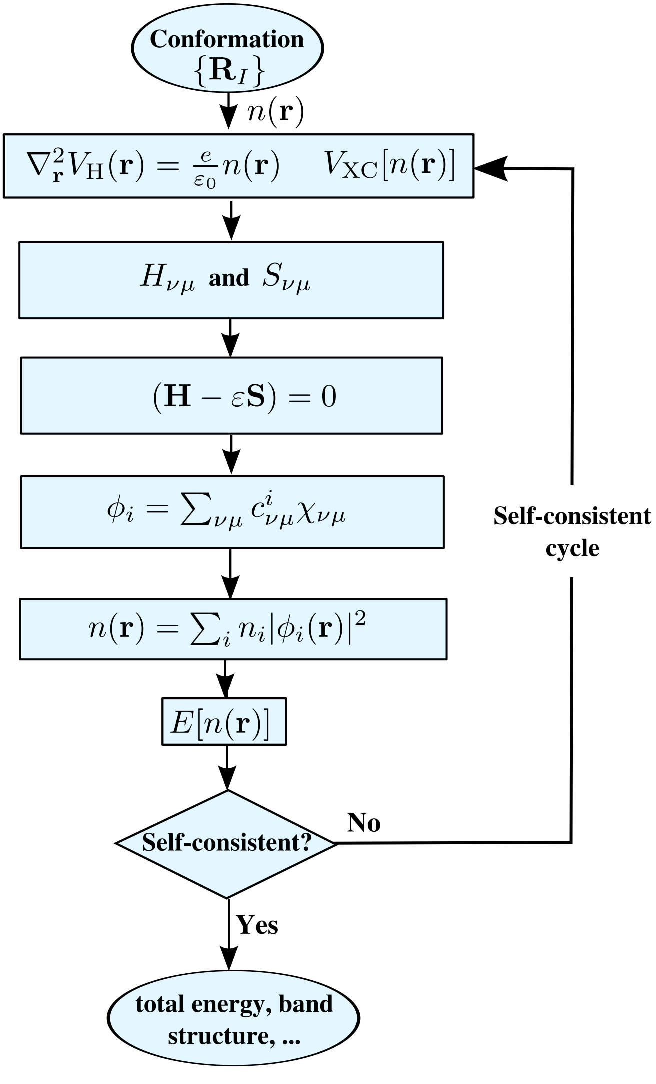

Figure 3.1: Schematic representation of self-consistent solutions of Kohn-Sham equations.

Chapter 4

Many-Body Green's Functions

4.1 Introduction

Density functional theory (DFT) that was briefly described in chapter 3 is a ground state theory. It can describe the ground state properties of a system of interacting electrons in an external potential in the form of effective single particle Kohn-Sham equations. However, predicting or interpreting results of experiments like photoemission, absorption , electron-energy loss that involves electronically excited states cannot be described by DFT since it cannot describe electron-hole excitations [27]. Accordingly, one needs to go beyond DFT in order to describe excited-state properties of molecules.

For the description of electronically excited states, there are two methods based on the ground of density functional theory that are commonly used. One is time-dependent density functional theory (TDDFT) [89]. The other one is based on many-body perturbation theory in which a set of Green's function equations [39, 90] is employed [27]. Electron's self energy Σ is introduced and proper description of electron-hole interactions is taken into account. Compared to Green's function methods, TDDFT benefits from density dependence rather than depending on the wave function or Green's functions but it suffers from the problem of choosing exchange correlation functional and does not account for bound excitons which are needed to describe absorption experiments. Despite that DFT cannot provide a good description of excited stated, the Kohn-Sham eigenvalues and eigenfunctions can be employed as a starting point for further excited state calculations [27]. In this chapter, we review some essentials of the many-body perturbation theory based on Green's functions. Hedin's equations [39] are presented in this chapter to describe the absorption and emission properties of molecules [27]. For a more detailed discussion, please see Refs. [27, 70, 71, 91].

4.2 Green's Functions

Let $|N\rangle$ be the normalized many electron ground state of the system. Then, the single-electron (single-particle) Green's function at zero temperature reads as

$$G(\mathbf{r},\sigma,t;\mathbf{r}',\sigma',t') = -i\,\langle N|\, T\hat{\psi}(\mathbf{r},\sigma,t)\hat{\psi}^{\dagger}(\mathbf{r}',\sigma',t')\,|N\rangle\,. \tag{4.1}$$

In eq. 4.1, T is the time-ordering operator, $\hat{\psi}(\mathbf{r},\sigma,t)$ and $\hat{\psi}(\mathbf{r}',\sigma',t')$ are annihilation and creation field operators, respectively. $\psi^{\dagger}(\mathbf{r},\sigma,t)\,|N\rangle$ creates an electron at time t and position $\mathbf{r}$ with spin σ, and defines (N+1)-state. By adding an electron to the system at time $t' < t$, the Green's function yields the probability amplitudes to detect an electron with spin σ at position $\mathbf{r}$ and time t. In this case the Green's function describes propagation of electrons.

If $t' > t$, the Green's function describes a system that an electron with spin σ has been removed at time t and position $\mathbf{r}$, and that describes the propagation of holes. By defining a collective index for space, time and spin variables $1 \equiv \{\mathbf{r}_1, t_1, \sigma_1\}$, the single electron Green's function (eq. 4.1) can be written as

$$G(1,2) = -i\,\langle N|\, T\hat{\psi}(1)\hat{\psi}^{\dagger}(2)\,|N\rangle\,. \tag{4.2}$$

The Single particle Green's function is a powerful tool in order to describe fundamental properties of many-electron system like charge density, spin density and total energy [27]. One can utilize the single-particle Green's function to calculate the expectation values of any single-particle operator in the ground-state of the system. The ground-state energy of the system is connected to single-particle Green's function through the Galitskii-Migdal [92] formula [27, 70].

However, for describing all the properties of the system the single-particle Green's function is not enough. For example in order to describe coupled exciton (electron-hole pair) in optical absorption and emission, single-particle Green's function cannot fully describe the system. Hence, a two-particle (two-body) Green's function is required,

$$G(1,2;1',2') = -\,\langle N|\, T[\hat{\psi}(1)\hat{\psi}(2)\hat{\psi}^{\dagger}(2')\hat{\psi}^{\dagger}(1')]\,|N\rangle\,. \tag{4.3}$$

In general one can write the N-particle (N-electron) Green's function [27, 70]as

$$G^N(1,\ldots,N;1^{'},\ldots,N^{'}) = \\ (-i)^N \langle N| T[\hat{\psi}(1)\ldots\hat{\psi}(N)\hat{\psi}^{\dagger}(N^{'})\ldots\hat{\psi}^{\dagger}(1^{'})] |N\rangle \,. \tag{4.4}$$

Lehmann representation (described below) of the Green's function allows one to make connection between the Green's function and the single-particle excitation energies of the system. By using the time-dependent field operator in the Heisenberg picture,

$$\hat{\psi}(1) = \hat{\psi}(\mathbf{r},t,\sigma) = e^{i\hat{H}t}\hat{\psi}_{\sigma}(\mathbf{r})e^{-i\hat{H}t}. \tag{4.5}$$

and a completeness relation

$$\sum_s |N+1,s\rangle \langle N+1,s| \;\; = \;\; 1. \tag{4.6}$$

$$\sum_s |N-1,s\rangle \langle N-1,s| \;\; = \;\; 1. \tag{4.7}$$

where $|N+1,s\rangle$ ($|N-1,s\rangle$) is the s-th excited state of the $N+1$-electron ($N-1$-electron) system with energy E_s^{N+1} (E_s^{N-1}). Assuming the Hamiltonian ($\hat{H}$) is time-independent, the single-electron Green's function can be written as

$$G(\mathbf{r},\sigma,t;\mathbf{r}',\sigma',t') = -i\sum_s e^{-i\varepsilon_s(t-t')}f_s(\mathbf{r},\sigma)f_s(\mathbf{r}',\sigma') \\ \times [\theta(t-t')\theta(\varepsilon_s-\mu) - \theta(t'-t)\theta(\mu-\varepsilon_s)], \tag{4.8}$$

where,

$$f_s(\mathbf{r},\sigma) = \begin{cases} \langle N| \hat{\psi}(\mathbf{r},\sigma) |N+1,s\rangle \,, & \varepsilon_s > \mu \\ \langle N-1,s| \hat{\psi}(\mathbf{r},\sigma) |N\rangle \,, & \varepsilon_s < \mu \end{cases} \tag{4.9}$$

and

$$\varepsilon_s = \begin{cases} E_s^{N+1} - E_0, & \varepsilon_s > \mu \\ E_0 - E_s^{N-1}, & \varepsilon_s < \mu \; . \end{cases} \tag{4.10}$$

This is called the Lehmann representation of the single-particle Green's function and $f_s(\mathbf{r},\sigma)$. $f_s(\mathbf{r}',\sigma')$ are referred to as the Lehmann amplitudes which describe the overlap between the ground state and excited state of the system.

They can be interpreted as the probability amplitudes for electron addition or removal. Using the integral representation of the step function,

$$\theta(t-t') \equiv \theta(\tau) = -\int_{-\infty}^{+\infty} \frac{d\omega}{2\pi i} \frac{e^{-i\omega}}{\omega + i\eta}. \tag{4.11}$$

and Fourier transform of eq. 4.8 we have

$$G(\mathbf{r},\sigma;\mathbf{r}',\sigma';\omega) = \sum_s \frac{f_s(\mathbf{r},\sigma) f_s(\mathbf{r}',\sigma')}{\omega - \varepsilon_s + i\eta \ \mathrm{sgn}(\varepsilon_s - \mu)}. \tag{4.12}$$

Electron addition and removal energies can be obtained by finding the poles of G in eq. 4.12 [27, 70, 71].

4.3 Connection to Spectroscopy

The Lehmann representation demonstrates the connection of the single-particle Green's function to photo-emission characterization. Specifically, the spectral function $A(\omega)$ is a quantity that makes the connection,

$$A(\omega) = \frac{1}{\pi} \left| \int d\mathbf{r} \lim_{\mathbf{r}' \to \mathbf{r}} \mathrm{Im}\ G(\mathbf{r},\mathbf{r}',\omega) \right| = \frac{1}{\pi} \left| \mathrm{Tr}[\mathrm{Im}\ G(\omega)] \right|. \tag{4.13}$$

By using the relation

$$\lim_{\eta \to 0^+} \frac{1}{x + i\eta} = \mathcal{P}\frac{1}{x} - i\pi\delta(x). \tag{4.14}$$

in which $\mathcal{P}$ stands for principle value, in the Lehmann representation of the Green's function in eq. 4.12 $A(\omega)$ is given by

$$A(\mathbf{r},\mathbf{r}',\omega) = \sum_s f_s(\mathbf{r}) f_s^*(\mathbf{r}') \delta(\omega - \varepsilon_s). \tag{4.15}$$

$A(\omega)$ has the same information as G. The spectral function has the following properties [27, 70, 71]:

- *Sum-rule:*

$$\int_{-\infty}^{+\infty} d\omega A(\mathbf{r},\mathbf{r}',\omega) = \delta(\mathbf{r} - \mathbf{r}'). \tag{4.16}$$

- *Ground state density:*

$$\int_{-\infty}^{\mu} d\omega \ A(\mathbf{r},\mathbf{r}',\omega) = n(\mathbf{r}). \tag{4.17}$$

- *Total energy can be calculated using $A(\omega)$ and the Galitskii-Migdal formula.*
- *Photoemission spectra can be obtained using $A(\omega)$.* The photocurrent from Fermi's Golden rule can be evaluated as a function of $A(\omega)$ [27, 70, 71]. In a simplified picture, one could have two kinds of excitations in a photo-emission spectrum: One is a sharp peak in spectrum originating from quasi-particle like excitations and the second is from the satellite structures corresponding to collective excitations which are broadened in a given energy area. Satellites in isolated atoms and molecules do not emerge due to their short lifetime [70].

4.4 Dyson equation and self-energy

Let us start from the equation of motion for the Heisenberg creation and annihilation field operators $\hat{\psi}^{\dagger}$ and $\hat{\psi}$ and derive a hierarchy of equations of motion in which the N-particle Green's function is linked to the $N+1$-particle and $N-1$-particle Green's functions [70, 71]. For instance, for single and two-particle Green's function

$$[i\frac{\partial}{\partial t_1} - h_0(1)]G(1,2) + i\int d3v(1,3)G(1,3^+;2,3^{++}) = \delta(1,2), \qquad (4.18)$$

where $h(1) \equiv h_0(\mathbf{r}_1)\delta(t_1)$ is the single-particle term of the many-body Hamiltonian (or density-independent part of the effective Hamiltonian) in which $h_0(\mathbf{r}) = \frac{-\nabla^2}{2} + V_{ext}(\mathbf{r})$. V_{ext} is assumed to be static, and

$$v(1,2) \equiv v(\mathbf{r},\mathbf{r}')\delta(t-t') = \frac{\delta(t-t')}{|\mathbf{r}-\mathbf{r}'|}. \qquad (4.19)$$

is the repulsive Coulomb interaction between electrons. Notation $1^+ \equiv \{\mathbf{r}_1, t_1+\eta, \sigma_1\}$ where η is a positive infinitesimal. Equation 4.18 is a reformulated version of the many electron problem to a set of equations of motions of Green's functions. However this set of equations of motions has the same complexity as the original many-body problem. For instance, for describing single-particle properties which are related to two-body Green's function, one needs to find an approximation for the two-particle Green's function to be expressed as a one-particle Green's function. For two-particle properties of the system which are related to the three-body Green's function, one needs to approximate the three-body Green's function in terms of the two-body Green's function [27, 70, 71].

One can define an auxiliary quantity called *self-energy* that contains all of the two-body effects,

$$\int d3\ \Sigma(1,3)G(3,2) = -i\int d3\ v(1,3)G(1,3^{+};2,3^{++}). \tag{4.20}$$

Using the definition of self-energy in eq. 4.18, one can obtain the Dyson equation

$$[i\frac{\partial}{\partial t_1} - h_0(1)]G(1,2) - \int d3\ \Sigma(1,3)G(3,2) = \delta(1,2). \tag{4.21}$$

Using Feynamn diagram techniques one can approximate the self-energy. It can be written as

$$\Sigma(1,2) = -i\delta(1,2)\int\ d3v(1,3)G(3,3^{+}) + iv(1,2)G(1,2+), \tag{4.22}$$

where the first term is the Hartree potential V_H

$$V_H(1,2) = \delta(1,2)\int d3\ v(1,3)n(3), \tag{4.23}$$

and the second term is the so-called exchange operator. The Hartree term is local and one can put it inside the one-particle Hamiltonian

$$h_0(1) = \frac{-\nabla^2}{2} + V_{ext} + V_H, \tag{4.24}$$

and self-energy designates the remaining exchange part [27, 70, 71, 91]. Using this definition, the self-energy accounts for the exchange-correlation that is, all electron-electron interactions beyond the Hartree term. With this definition of self-energy we have

$$[i\frac{\partial}{\partial t_1} + \frac{\nabla_1^2}{2} - V_{ext}(1) - V_H(1)]G(1,2) - \int d3\ \Sigma(1,3)G(3,2) = \delta(1,2). \tag{4.25}$$

This self-energy operator accounts for two-particle effects, and in general is a complex, non-local, and non-Hermitian operator. The real part of the self-energy can be attributed to the exchange and correlation contributions of quasi-particle energies and its imaginary part corresponds to the excitation life-time [27, 70, 71, 91].

4.5 Non-interacting limit

Most *ab initio* approaches are based on the effective non-interacting particle picture. It is useful for writing the Lehmann representation of the Green's function in terms of single-particle orbitals $\{\phi_i^{\mathrm{QP}}\}$ (quasi-particle orbitals) with eigenvalues $\{\varepsilon_i^{\mathrm{QP}}\}$, which they are the eigenfunctions and eigenvalues of the effective single-particle Hamiltonian $h_0\phi_i^{\mathrm{QP}} = \varepsilon_i^{\mathrm{QP}}\phi_i^{\mathrm{QP}}$.
By using the expression for the field operator, $\hat{\psi}(\mathbf{r}) = \sum_i \phi_i^{\mathrm{QP}}(\mathbf{r})\hat{c}_i^\dagger$

$$\begin{aligned} f_s(\mathbf{r}) &= \langle N|\,\hat{\psi}(\mathbf{r})\,|N+1,s\rangle \\ &= \sum_i \phi_i^{\mathrm{QP}}(\mathbf{r})\,\langle N|\,\hat{c}_i^\dagger\,|N+1,s\rangle \\ &= \sum_i \phi_i^{\mathrm{QP}}(\mathbf{r})\delta_{i,s} = \phi_i^{\mathrm{QP}}(\mathbf{r}). \end{aligned} \tag{4.26}$$

and single-particle excitation energies are related to the single-particle eigenvalues as

$$\varepsilon_s = E_s^{N+1} - E_0 = \varepsilon_s^{\mathrm{QP}}. \tag{4.27}$$

One can rewrite the Lehmann representation of the Green's function in terms of single-particle orbitals and single particle energies as

$$G_0(\mathbf{r};\mathbf{r}';\omega) = \sum_i \frac{\phi_i^{\mathrm{QP}}(\mathbf{r})\phi_i^{\mathrm{QP}}(\mathbf{r}')}{\omega - (\varepsilon_i^{\mathrm{QP}} - \mu) - i\eta\ \mathrm{sgn}(\varepsilon_i^{\mathrm{QP}} - \mu)}. \tag{4.28}$$

The same applies to its Fourier transform ($\tau = t - t'$),

$$\begin{aligned} G_0(\mathbf{r},\mathbf{r}',\tau) = -i\sum_i & e^{-i(\varepsilon_i^{\mathrm{QP}}-\mu)\tau}\phi_i^{\mathrm{QP}}(\mathbf{r})\phi_i^{\mathrm{QP}}(\mathbf{r}') \\ & \times [\theta(\tau)\theta(\varepsilon_i^{\mathrm{QP}} - \mu) - \theta(-\tau)\theta(\mu - \varepsilon_i^{\mathrm{QP}})]. \end{aligned} \tag{4.29}$$

By differentiating eq. 4.29 with respect to time, one can derive the equation of motion for the non-interacting Green's function as

$$[i\frac{\partial}{\partial t_1} - h_0(1)]G_0(1,2) = \delta(1,2). \tag{4.30}$$

By replacing the δ-function in Dyson equation eq. 4.21:

$$[i\frac{\partial}{\partial t_1} - h_0(1)][G(1,2) - G_0(1,2)] = \int d3\Sigma(1,3)G(3,2). \tag{4.31}$$

and therefore,

$$G(1,2) = G_0(1,2) + \int d3d4\ G_0(1,3)\Sigma(3,4)G(4,2). \tag{4.32}$$

Hence, we can write the Dyson equation for the Green's function in terms of non-interacting Green's function [27, 70, 71, 91] as

$$G = G_0 + G_0\Sigma G. \tag{4.33}$$

4.6 Hedin's equations

The single-particle Green's function is essential for electronic excitations of the many-body system which obeys the equation of motion as given in eq. 4.25. In order to assess the one-electron Green's function and self-energy, Lars Hedin in 1965 [90] derived a set of self-consistent equations known as Hedin's equations. By expanding the self-energy in terms of a screened Coulomb potential W rather than bare Coulomb potential v, Hedin's equations can be obtained considering that the total energy needs to be stationary with respect to variations in the Green's function. In a real many-body system interactions are screened and one needs to consider electron relaxation and correlation effects. The screened Coulomb potential first was introduced by Hubbard [93].

In this section the main results of Hedin's equations are provided. The details of how to derive these equations can be found in Refs. [90, 91]. Starting from the definition of self-energy and using Schwinger's techniques [94] of functional derivatives and introducing a local time-dependent potential coupled to electron density, Hedin's equations can be obtained [27, 70, 91] as

$$G(1,2) = G_0(1,2) + \int d34\ G_0(1,3)[V_H(3)\delta(3,4) + \Sigma(3,4)]G(4,2) \tag{4.34a}$$

$$P(1,2) = -i\int d34\ G(2,3)G(4,2)\Gamma(3,4;1) \tag{4.34b}$$

$$W(1,2) = v(1,2) + \int d34\ v(1,3)P(3,4)W(4,2) \tag{4.34c}$$

$$\Sigma(1,2) = i\int d34\ G(1,4)W(3,1^+)\Gamma(4,2;3) \tag{4.34d}$$

$$\Gamma(1,2;3) = \delta(1,2)\delta(1,3) + \int d4567\frac{\delta\Sigma(1,2)}{\delta G(4,5)}G(4,6)G(7,5)\Gamma(6,7;3), \tag{4.34e}$$

where P is the polarization operator (contains the response of the system to electron addition or removal (hole)), W is the dynamically screened Coulomb

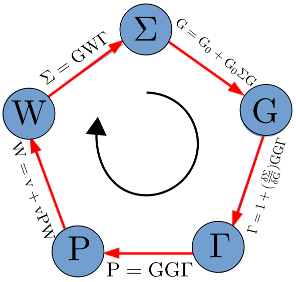

Figure 4.1: Schematic representation of the iterative solution of the set of Hedin's equations for G, Σ, W, P, and Γ [91].

interaction, Σ is the self-energy, and Γ the 3-point vertex function which includes information of electron-hole interaction. The self-dependence of eq. 4.34 is because each of them depends on the other four. Hedin's equation need to be solved iteratively:

1. Initialize the non-interacting Green's function G_0.
2. Calculate P, W, and Σ.
3. Evaluate Γ.
4. Update the Green's function using the Dyson equation (eq. 4.34a).
5. Iterating until satisfactory convergence is obtained.

There is no complete solution for this set of equations. Consequently, approximations are required [27, 70, 91].

4.7 The *GW* Approximation

The *GW* approximation signifies the perturbative expansion of self-energy in terms of W as in Hedin's approximation [90] and keeping only the first order term so that the self-energy is obtained as product of G and W. Therefore it is referred to as the *GW* approximation. The *GW* approximation can be achieved by keeping only the diagonal terms of the vertex function Γ and neglecting the vertex corrections, that is,

$$\Gamma(1,2;3) = \delta(1,2)\delta(1,3). \tag{4.35}$$

Accordingly, we have non-interacting quasielectron-quasihole pairs and Hedin's equation in the *GW* approximation can be given as

$$G(1,2) = G_0(1,2) + \int d34\ G_0(1,3)[V_H(3)\delta(3,4) + \Sigma(3,4)]G(4,2) \tag{4.36a}$$

$$P(1,2) = -iG(1,2)G(2,1) \tag{4.36b}$$

$$W(1,2) = v(1,2) + \int d34\ v(1,3)P(3,4)W(4,2) \tag{4.36c}$$

$$\Sigma(1,2) = iG(1,2)W(1,2) \tag{4.36d}$$

$$\Gamma(1,2;3) = \delta(1,2)\delta(1,3). \tag{4.36e}$$

The *GW* approximation was introduced by Hedin and Lundqvist [90, 39]. Note that the particle number and energy are conserved in the fully self-consistent *GW* approximation. From eq. 4.36a one can start from the Green's function of non-interacting electrons with an effective single-particle potential and iterate till convergence is achieved. Equation 4.36 is still very complicated to be solved in practice. One can follow different approaches to solve eq. 4.36. One way is nonself-consistent G_0W_0 in which Green's function of non-interacting electrons, G_0, is used instead of updating G in every iteration, and static approximation of screened Coulomb potential W is employed. In other approach only G is updated in every iteration and not W. The result of total energy calculations for a homogeneous electron gas from a fully self-consistent *GW* is very close to the result from quantum Monte Carlo scheme, however regarding spectroscopic properties, it fails in description of bandwidth and quasiparticle excitation lifetime [27]. In order to go beyond GW, one needs to consider vertex corrections [27, 70, 91].

4.8 Random Phase Approximation

The presence of other charged particles leads to screening of the initial long-range Coulomb interactions, and hence the integral equation of polarization P can be approximated at the lowest order. This is called the Random Phase Approximation (RPA). Within the *GW* approximation the dielectric function can be given by as

$$\epsilon(\mathbf{r},\mathbf{r}',\omega) = \delta(\mathbf{r}-\mathbf{r}') - \int dr''\ v(\mathbf{r}-\mathbf{r}'')P(\mathbf{r}'',\mathbf{r}',w), \tag{4.37}$$

where v is the bare Coulomb potential and P is the polarizability operator. In the GW approximation P is given by $P(1,2) = -iG(1,2)G(2,1)$, where in the approximation of non-interacting electrons using the quasiparticle eigenfunctions can be written as

$$P(\mathbf{r},\mathbf{r}',w) = \sum_{ij}(f_i - f_j)\frac{\phi_i(\mathbf{r})\phi_j^*(\mathbf{r})\phi_j(\mathbf{r}')\phi_i^*(\mathbf{r}')}{\omega - \omega_{ij} + i\eta}, \tag{4.38}$$

where $\omega_{ij} = (\varepsilon_j - \varepsilon_i)$, f_i are Fermi occupation numbers and ε_i are the eigenvalues of the non-interacting system. This approximation to P is in form of RPA [27]. The dynamic Coulomb interaction (W) within the RPA as a function of the dielectric function ε and the bare Coulomb interaction v is given by:

$$W = \epsilon^{-1}v. \tag{4.39}$$

Physically, RPA means that electrons respond to the total effective field as if they were non-interacting [91].

4.9 *GW* in practice

The Fourier transform of the self-energy operator in the GW approximation, eq. 4.36, can be evaluated as

$$\Sigma(\mathbf{r},\mathbf{r}',E) = \frac{i}{2\pi}\int e^{-i\omega\eta}G(\mathbf{r},\mathbf{r}',E-\omega)W(\mathbf{r},\mathbf{r}',\omega)\,d\omega. \tag{4.40}$$

where η is a positive infinitesimal number. In order to compute Σ one can employ the Kohn-Sham wave functions and energies,

$$\left\{-\frac{\nabla^2}{2} + V_{\mathrm{PP}}(\mathbf{r}) + V_H(\mathbf{r}) + V_{\mathrm{xc}}(\mathbf{r})\right\}\phi_i^{\mathrm{KS}}(\mathbf{r}) = \varepsilon_i^{\mathrm{KS}}\phi_i^{\mathrm{KS}}(\mathbf{r}). \tag{4.41}$$

and calculate G and W using ϕ^{KS} as

$$G(\mathbf{r},\mathbf{r}',\omega) = \sum_i \frac{\phi_i^{\mathrm{KS}}(\mathbf{r})\phi_i^{\mathrm{KS}^*}(\mathbf{r}')}{\omega - \varepsilon_i + i\eta\ \mathrm{sgn}(\varepsilon_i - \mu)}, \tag{4.42}$$

where eq. 4.42 is the Lehmann representation of the single-particle Green's function in non-interacting quasi-particle picture, and η is a positive infinitesimal number. One approach to solve the equation of motion for quasi-particles in the *GW* approximation,

$$\left\{-\frac{\nabla^2}{2} + V_{\mathrm{PP}}(\mathbf{r}) + V_H(\mathbf{r})\right\}\phi_i^{\mathrm{QP}}(\mathbf{r}) + \int d\mathbf{r}'\Sigma(\mathbf{r},\mathbf{r}',\varepsilon_i)\phi_i^{\mathrm{QP}}(\mathbf{r}) = \varepsilon_i\phi_i^{\mathrm{QP}}(\mathbf{r}), \tag{4.43}$$

is to expand ϕ^{QP} in terms of Kohn-Sham wave functions ϕ^{KS},

$$|\phi_i^{\mathrm{QP}}\rangle = \sum_j c_j^{(i)}\,|\phi_j^{\mathrm{KS}}\rangle\,. \tag{4.44}$$

Using this basis set in eq. 4.43, the matrix elements of the quasi-particle Hamiltonian can be written as

$$H_{ii'}^{\mathrm{QP}}(\varepsilon) = \varepsilon_i^{\mathrm{KS}}\delta_{ii'} + \langle\phi_i^{\mathrm{KS}}|\,\Sigma - V_{\mathrm{xc}}\,|\phi_{i'}^{\mathrm{KS}}\rangle\,. \tag{4.45}$$

$\Sigma - V_{\mathrm{xc}}$ in eq. 4.45 can be treated as a perturbation of Kohn-Sham energies $\varepsilon_i^{\mathrm{KS}}$. Accordingly, the equation of motion of the quasi-particle can be evaluated on a post-DFT level perturbatively[27, 40, 41, 42, 91, 95].

4.10 Electron-Hole Pair Excitations with Bethe-Salpeter Equation

Although in the *GW* approximation, the quasiparticle energies describe the energetics of the single-particle excitations quite accurately. This kind of single-particle picture is not enough to describe optical excitations which involve coupled excitations of an electron and hole. The macroscopic polarization function P^{M} is needed to describe the optical spectra. Considering static screening and the absence of external fields, P^{M} only depends on the difference of time-dependent variables. Considering Hedin's equations for the vertex function eq. 4.34e and polarization, eq. 4.34b, the *Bethe-Salpeter* equation for polarization is given by

$$P^{\mathrm{M}}(t-t') = L_0(t-t') + \int dt'' L_0(t-t'')\Xi^{\mathrm{M}}P^{\mathrm{M}}(t''-t'), \tag{4.46}$$

where L is the *two-point correlation function* or *density correlation function* which describes the correlated propagation of two particles (electron-hole), and L_0 corresponds to free electron-hole pairs. It is given by

$$P(12) = L_0(12, 1'2') = -iG(1, 2')G(2, 1'), \tag{4.47}$$

where Ξ^M denotes the static electron-hole interaction kernel. Equation 4.46 can be written as

$$\begin{aligned} P^{\mathrm{M}}_{\sigma\sigma',\sigma_2\sigma_2'}(\mathbf{r}_1\mathbf{r}_1', \mathbf{r}_2\mathbf{r}_2'; \tilde{\omega}) &= \sum_n \Big\{ G_{\sigma_1\sigma_2'}(\mathbf{r}_1\mathbf{r}_2'; \omega_n) G_{\sigma_2\sigma_1'}(\mathbf{r}_2\mathbf{r}_1'; \omega_n - \tilde{\omega}_m) \\ &+ \sum_{\sigma_3\sigma_4\sigma_3'\sigma_4'} \int d\mathbf{r}_3\, d\mathbf{r}_4\, d\mathbf{r}_3'\, d\mathbf{r}_4' G_{\sigma_1,\sigma_4}(\mathbf{r}_1\mathbf{r}_4; \omega_n) G_{\sigma_3\sigma_1'}(\mathbf{r}_3\mathbf{r}_1'; \omega_n - \tilde{\omega}_m) \\ &\times \Xi^{\mathrm{M}}_{\sigma_3\sigma_4\sigma_3'\sigma_4'}(\mathbf{r}_3\mathbf{r}_4, \mathbf{r}_3'\mathbf{r}_4') P^{\mathrm{M}}_{\sigma_3'\sigma_4'\sigma_2\sigma_2'}(\mathbf{r}_3'\mathbf{r}_4', \mathbf{r}_2\mathbf{r}_2'; \tilde{\omega}_m) \Big\}. \end{aligned} \tag{4.48}$$

Expanding electron-hole state in terms of quasi-particle wave functions $\{\phi^{\mathrm{QP}}\}$,

$$\Phi^S(\mathbf{r}_e, \mathbf{r}_h) = \sum_\alpha^{\mathrm{occ}} \sum_\beta^{\mathrm{virt}} [A^S_{\alpha\beta} \phi^{\mathrm{QP}}_\beta(\mathbf{r}_e) \phi^{\mathrm{QP}^*}_\alpha(\mathbf{r}_h) + B^S_{\alpha\beta} \phi^{\mathrm{QP}}_\alpha(\mathbf{r}_e) \phi^{\mathrm{QP}^*}_\beta(\mathbf{r}_h)], \tag{4.49}$$

where α(valence states) and β(conduction states) represents the single-particle occupied and virtual(empty) states, respectively, and $A_{\alpha\beta}$ and $B_{\alpha\beta}$ are the resonant and anitresonant electron-hole amplitudes which indicate transitions from an occupied to a virtual state and from a virtual to an occupied state, respectively. Equation 4.48 can be transformed into an eigenvalue problem [27, 40, 41, 42, 91],

$$\begin{pmatrix} H & \Xi^{\mathrm{M}} \\ -\Xi^{\mathrm{M}^*} & -H^* \end{pmatrix} \begin{pmatrix} A^S \\ B^S \end{pmatrix} = \Omega_S \begin{pmatrix} A^S \\ B^S \end{pmatrix}. \tag{4.50}$$

H is the resonant matrix of transition. Its matrix elements are given by

$$H(\alpha\beta, \alpha'\beta') = [\varepsilon^{\mathrm{QP}}_\beta - \varepsilon^{\mathrm{QP}}_\alpha] \delta_{\beta\beta'} \delta_{\alpha\alpha'} \underbrace{-W_{\alpha\alpha',\beta\beta'}}_{\mathrm{K^d}} + \underbrace{\bar{v}_{\alpha\beta,\alpha'\beta'}}_{\mathrm{K^x}}, \tag{4.51}$$

where Ξ^{M} is the coupling matrix between the resonant and antiresonant transitions:

$$\Xi^{\mathrm{M}}(\alpha\alpha', \beta\beta') = \underbrace{-W_{\alpha\beta,\alpha'\beta'}}_{\mathrm{K^d}} + \underbrace{\bar{v}_{\alpha\alpha',\beta\beta'}}_{\mathrm{K^x}}. \tag{4.52}$$

For details, please see equations (19.9) and (19.32) in Ref. [91]. $\mathrm{K^d}$ denotes the statically screened Coulomb interaction and $\mathrm{K^x}$ represents electron-hole exchange which is the short-range unscreened Coulomb repulsion.[91]. Ω is the transition energy of the optical excitation. Note that in general α and β depend on spin of quasi-particles, respectively.

The spin structure of the solutions of BSE is an important issue that we briefly discuss here. Considering the Hilbert space of electron-hole pairs with their spin structure, including four subspaces: $v\uparrow c\uparrow$, $v\uparrow c\downarrow$, $v\downarrow c\uparrow$, and $v\downarrow c\downarrow$, the BSE Hamiltonian can be written is this general form:

$$\begin{pmatrix} D+\mathrm{K^d}+\mathrm{K^x} & 0 & 0 & \mathrm{K^x} \\ 0 & D+\mathrm{K^d}+\mathrm{K^x} & 0 & 0 \\ 0 & 0 & D+\mathrm{K^d} & 0 \\ \mathrm{K^x} & 0 & 0 & D+\mathrm{K^d}+\mathrm{K^x} \end{pmatrix} \begin{pmatrix} v\uparrow c\uparrow \\ v\uparrow c\downarrow \\ v\downarrow c\uparrow \\ v\downarrow c\downarrow \end{pmatrix}, \quad (4.53)$$

where D is $D=[\varepsilon_c^{\mathrm{QP}}-\varepsilon_v^{\mathrm{QP}}]$. Considering spin-singlet $(\frac{1}{\sqrt{2}}(v\uparrow c\uparrow - v\downarrow c\downarrow))$ and spin-triplet $(v\uparrow c\downarrow, \frac{1}{\sqrt{2}}(v\uparrow c\uparrow + v\downarrow c\downarrow), v\downarrow c\uparrow)$, a class of solutions (one should note that the spin of a hole state in valence band v is the negative of the spin of the electron which initially occupied that state), the Hamiltonian becomes $[\varepsilon_c^{\mathrm{QP}}-\varepsilon_v^{\mathrm{QP}}]+\mathrm{K}^d$ for spin triplet subset and $[\varepsilon_c^{\mathrm{QP}}-\varepsilon_v^{\mathrm{QP}}]+\mathrm{K}^d+2\mathrm{K}^x$ for spin singlet. Therefore, the BSE Hamiltonian can be decoupled for the singlet and triplet states. Since K^x vanishes for spin-triplet transitions and is nonzero and repulsive for spin-singlet transitions, the spin-singlet excitations are higher in energies than the spin-triplet states. Evaluating the full BSE with its spin structure, increases the number of basis sets by a factor of four and hence the computation of BSE becomes more demanding.

Since the off-diagonal term Ξ^{M} in eq. 4.50 has been found to be very small for many systems, one can neglect resonant-antiresonant coupling terms Ξ when they are much smaller than H and hence the resonant and antiresonant parts of full BSE decouple. This is the so-called *Tamm-Dancoff Approximation* (TDA) [27, 40, 41, 42, 91, 95]. Within TDA, the electron-hole wavefunction of the excitation S is given by

$$\Phi_S(\mathbf{r}_e,\mathbf{r}_h)=\sum_{\alpha}^{\mathrm{occ}}\sum_{\beta}^{\mathrm{virt}} A_{\alpha\beta}^S \phi_\beta^{\mathrm{QP}}(\mathbf{r}_e)\phi_\alpha^{\mathrm{QP}*}(\mathbf{r}_h). \quad (4.54)$$

The electron-hole amplitudes $A_{\alpha\beta}^S$ and the associated transition energies Ω_S

can be obtained by solving

$$(\varepsilon_\beta^{\mathrm{QP}} - \varepsilon_\alpha^{\mathrm{QP}})A_{\alpha\beta}^S + \sum_{\alpha'\beta'} K_{\alpha\beta,\alpha'\beta'}^{\mathrm{eh}}(\Omega_S)A_{\alpha'\beta'}^S = \Omega_S A_{\alpha\beta}^S. \tag{4.55}$$

in which $K^{\mathrm{eh}} = \eta K^x + K^d$ ($\eta = 2$ for singlets, $\eta = 0$ for triplets) is the electron-hole interaction kernel comprised of bare exchange (K^x) and screened direct terms (K^d), respectively.

Figure 4.2 represents the flow chart for GW-BSE steps in order to calculate the excitation energies Ω_S. Having the structure of the molecule, first, the molecular orbitals and energies are determined by solving the Kohn-Sham equations. The single-particle Green's function and the screened Coulomb potential in RPA are computed using the Kohn-Sham molecular orbitals and energies. Because DFT underestimates the fundamental HOMO-LUMO gap [53], the self-energy and the resulting QP energies may deviate from the self-consistent result. In order to avoid this deviation, an iterative procedure is employed in which W is calculated from a scissor-shifted Kohn-Sham spectrum [53, 41]. From the resulting QP gap, a new value for the scissor-shift is determined and this procedure is repeated until convergence is reached. For each step, the QP energy levels are iterated and the Green's function of eq. 4.42 and thus the self-energy are updated. A one-shot G_0W_0 calculation from Kohn-Sham energies may differ from iterated results by up to several 0.1 eV. Note that this (limited) self-consistency treatment does not change the QP structure of eq. 4.42 (due to satellite structures or other consequences of a self-consistent spectral shape of $G(\omega)$). Finally, the coupled electron-hole wave function and excitation energies are computed using BSE within TDA.

4.11 Oscillator Strength

In order to describe the strengths of the optical transitions in molecules one can employ the so-called *oscillator strengths* (f-values). Considering a classical single-electron oscillator with oscillation frequency $\omega_{\beta\alpha}$ with classical radiative decay rate $\gamma = \frac{e^2\omega_{\beta\alpha}^2}{6\pi\epsilon_0 m_e c^3}$, f-values "describes what fraction of the energy of the classical oscillator should be ascribed to a given transition" [96]. For emission it is defined by

$$A_{\beta\alpha} = -3f_{\beta\alpha}\gamma, \tag{4.56}$$

and for absorption as

$$g_\alpha f_{\alpha\beta} = -g_\beta f_{\beta\alpha} \equiv gf, \tag{4.57}$$

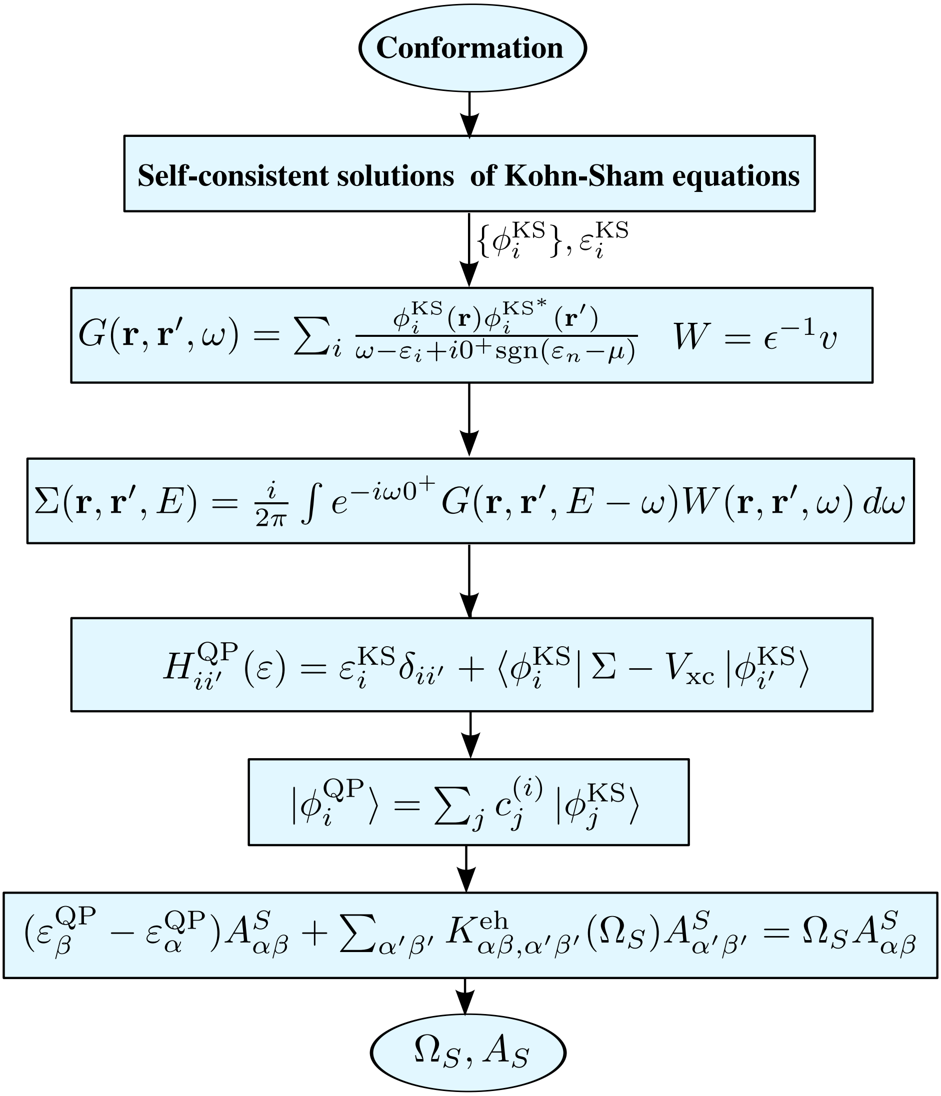

Figure 4.2: Schematic representation of GW-BSE on the ground of Kohn-Sham calculations.

where $f_{\beta\alpha}$ are the oscillator strengths and $A_{\beta\alpha}$ are the transition probabilities from a upper quantum state 2 to a lower quantum state 1. $g = 2J + 1$ where J is the angular momentum quantum number. For spin-singlet, $J_1 = 0$ and $g = 1$. For spin-triplet, $J_2 = 1$ and $g = 3$.

From a quantum electrodynamic treatment, the f-values are given by

$$f_{\beta\alpha} = -\frac{2}{3}\frac{\omega_{\beta\alpha}}{g_\beta}\sum_{m_\beta,m_\alpha} |\left\langle \beta m_\beta \right| \vec{\mathbf{r}} \left| \alpha m_\alpha \right\rangle|^2. \tag{4.58}$$

where $\omega_{\beta\alpha}$ are given by the energy differences of the quantum levels $(\varepsilon_\alpha - \varepsilon_\beta)$ and m_α and m_β are the spin quantum numbers of levels α and β, respectively. However, the electron-hole interaction is not present in the above discussion [96, 97]. The electron-hole interaction couples different electron-hole configurations to the excitation S [95]. As such, the transition matrix elements become

$$\left\langle 0 \right| \vec{r} \left| S \right\rangle = \sum_{\alpha\beta} A^S_{\alpha\beta} \left\langle \alpha \right| \vec{r} \left| \beta \right\rangle, \tag{4.59}$$

which is a sum of transition matrix elements of interband configurations. As a result, the f-values for coupled electron-hole excitations with electron-hole interaction in TDA approximation and in the absence of spin-orbit coupling is given by

$$f_S = \frac{2}{3}\Omega_S \sum_S |\left\langle 0 \right| \vec{r} \left| S \right\rangle|^2. \tag{4.60}$$

Chapter 5

Hybrid Quantum Mechanics-Classical Mechanics (QM/MM)

5.1 Introduction

Classical Molecular Dynamics (MD) is probably the most commonly used computational technique to study macromolecules. It is based on predefined potentials, *force fields.* For the reason that quantum mechanical methods are computationally expensive, inevitably one needs to employ MD simulations for systems with a lot of atoms. However, being able to describe electronic excitations in molecules necessitates a quantum mechanical treatment of at least a part of the system. One approach to describe these systems is to employ the GW-BSE technique on a selected component of the system and account for the classical environment (e.g. solvent molecules) by describing it with a polarizable force field that interacts with the GW-BSE subpart. This is the topic of the following chapter.

5.2 Classical Molecular Dynamics

In MD simulations, atoms are considered as classical objects evolving according to Newton's equation of motion [98, 99]. Hence, the energy of the system is considered to be only a function of nuclear positions. The electronic degrees of freedom are not treated explicitly. This simplification is valid for systems where electronic properties are not considered to be dominant in the total behavior of the system. This lets one to save computational time and study systems with a large number of atoms [98, 100, 101]. The *Born-Oppenheimer approximation* [72], *adiabatic approximation* [102], and considering nuclei as *classical objects* are approximations that lead to classical MD.

As a result of the aforementioned approximations, the movement of N classical particles (atoms) in an effective potential $V(\mathbf{R}_I)$, $I = 1, 2, ..., N$ is given by

$$\mathbf{F}_I[\{\mathbf{R}\}] = M_I \ddot{\mathbf{R}}_I = -\frac{\partial V(\mathbf{R}_I)}{\partial \mathbf{R}_I}, \tag{5.1}$$

where $\mathbf{R}_I$ defines the position of atom I. The potential energy $V(\mathbf{R})$ is usually divided into many-body terms which together with their parameters are collectively called a *force field* [100]:

$$\begin{aligned} V^{FF}(\{\mathbf{R}_I\}) = \sum_{I=1}^{N} v_1(\mathbf{R}_I) + \sum_{I<I'}^{N} v_2(\mathbf{R}_I, \mathbf{R}_{I'}) \\ + \sum_{I<I'<I''}^{N} v_3(\mathbf{R}_I, \mathbf{R}_{I'}, \mathbf{R}_{I''}) + \ldots \end{aligned} \tag{5.2}$$

The terms in eq. 5.2 are single-particle, two-body, and three-body interaction terms, respectively. Most often, the functional form of the potential is considered to be a sum of bond stretching, angle bending, bond torsion and non-bonded interactions, e.g., electrostatics and van der Waals interactions [103, 101]

$$\begin{aligned} V(\mathbf{R}) &= \sum_{\text{bonds},i} \frac{k_{\text{bond}}}{2}(l_i - l_{i,0})^2 + \sum_{\text{angles},i} \frac{k_\theta}{2}(\theta_i - \theta_{i,0})^2 \\ &+ \sum_{\text{tosion,i}} \sum_{n=0}^{5} \frac{k_{\text{tor},i}}{2}(-1)^n(\cos(n\phi)) \\ &+ \sum_{I=1}^{N} \sum_{J>I} \Big\{ 4\epsilon_{IJ}\Big[\Big(\frac{\sigma_{IJ}}{r_{IJ}}\Big)^{12} - \Big(\frac{\sigma_{IJ}}{r_{IJ}}\Big)^{6}\Big] + \frac{q_I q_J}{4\pi\epsilon_0 r_{IJ}} \Big\}, \end{aligned} \tag{5.3}$$

where k_{bond}, k_θ, k_{tor}, ϵ_{IJ}, and σ_{IJ} are force constants, that is, *force field parameters.* Force field parameters can be evaluated from experimental data and/or independent electronic structure calculations [101, 100].

The solution to the differential equations eq. 5.1 can be obtained using numerical techniques in discrete time steps such as the Verlet algorithm [104].

This algorithm is based on Taylor expansion of coordinate $\mathbf{R}$ around time t as

$$\mathbf{R}_I(t + \delta t) = 2\mathbf{R}_I(t) - \mathbf{R}_I(t - \Delta t) + \frac{\mathbf{F}_I[\{\mathbf{R}(t)\}]}{M_I}\Delta t^2 + \mathcal{O}(\Delta t^4). \qquad (5.4)$$

Velocity can then be evaluated as

$$\mathbf{v}_I(t) = \frac{\mathbf{R}_I(t + \Delta t) - \mathbf{R}_I(t - \Delta t)}{2\Delta t} + \mathcal{O}(\Delta t^2). \qquad (5.5)$$

In equations 5.4 and 5.5, Δt is the time step. The error for the positions is proportional to Δt^4, and for the velocities Δt^2. Δt should be chosen by using the time scale of the fastest motion in the system as the guideline, for instance, the high frequency hydrogen bond vibrations. Usually, one is not interested in these motions, and one can constrain these bond lengths. Hence, one can increase Δt. Typically, a time step of 1 fs with typically non-constrained, and 2 fs with constrained bond lengths are used [98].

5.2.1 Periodic Boundary Conditions

Typically one desires to simulate macromolecules in a large box of solvent to reduce the boundary effects on the measured properties. Moreover, due to physical conditions such as dilution, the box size needs to be large. This is, however, impractical and computationally expensive. In order to overcome this difficulty one can use *periodic boundary conditions* (PBC) which involves repeated identical copies of the simulation box.

5.2.2 Long-Range Interactions

Computing long-range interactions is challenging in MD simulations and special treatments are required to calculate them [105]. The electrostatic potential at position of atom I of a molecule consisting of N atoms with charge q_J in a cubic box of length L and volume $V = L^3$ with periodic boundary conditions applied in all directions, is given by

$$V(\mathbf{r}_I) = \sum_{\mathbf{m}} \sum_{J=1 J\neq I}^{N} \frac{q_J}{|\mathbf{r}_I - \mathbf{r}_J + \mathbf{m}L|}, \qquad (5.6)$$

where $\mathbf{m} = (m_x, m_y, m_z) \in \mathbb{Z}$ is the index vector for the simulation box. Due to PBC, atom I interacts with atom J and all of its images. This leads to the sum over $\mathbf{m}$. One needs to define the so-called minimum image condition to avoid double counting [99]. Its computational cost for N atoms is of the order of $\mathcal{O}(N^2)$ since a sum over $N(N-1)/2$ pairs is required [105]. In order to compute the electrostatic interactions, there are several approaches. They are briefly discussed next:

1. In *Cut-off Methods* a cut-off length is chosen and electrostatic interactions are only considered inside that cut-off region and disregarded outside. The computational cost of this method is of the order of $\mathcal{O}(N)$. They are however, inaccurate [105, 106].

2. In *Reaction Field Methods* [107, 108], a spherical cut-off is considered for each atom and a homogeneous dielectric is introduced beyond it. Electrostatic interactions inside the cut-off are calculated explicitly. This method has improved accuracy relative to the cut-off method with a computational cost of order $\mathcal{O}(N)$.

3. In *Ewald summation* [109] the Coulomb sum is described as two terms: a short-range term computed in real space and a long-range term calculated in Fourier space [110]. The computational cost of this method is higher than the simple truncation techniques and reaction field methods and is of the order of $\mathcal{O}(N^{3/2})$ [98].

4. The *Particle-Mesh Ewald Method* [111] is based on Ewald summation. To speed up computation, charges are projected on a grid using B-spline interpolation. Fast Fourier Transform algorithm [112] is then utilized. The computational cost of this approach is $\mathcal{O}(N \log(N))$ [101].

For a detailed description of algorithms for computing long range electrostatics, and their pros and cons, please see Ref. [105, 106].

5.2.3 Statistical Ensembles

Classical molecular mechanics and quantum mechanics give information about the state of the system. Statistical mechanics provides the necessary tools to connect microscopic information to macroscopic observables of thermodynamics and conformational properties. It introduces the concept of statistical ensembles (introduced by Gibbs in 1876 [113] for the first time) which is a set of all possible microstates of the system that have the same macroscopic properties like total energy E, number of particles N, volume V, pressure P, temperature T, and chemical potential μ. Macroscopic observables can be calculated by taking an *ensemble average.* In this section a brief overview of statistical ensembles is provided.

- The *Microcanonical Ensemble* (NVE) defines a set of isolated systems characterized by fixed number of particles N, volume V, and total energy E in which microstates of the system are on the constant energy hypersurface. The probability of finding a microstate in vicinity (E_0) of the constant energy hypersurface (E), is given by [114]

  $$\frac{1}{\Omega(N,V,E)}, \tag{5.7}$$

  where $\Omega(N,V,E)$ is the total amount of microstates available for the system. It is given by [114]

  $$\Omega(N,V,E) = \frac{1}{h^{3N}} \int_{E<H(x)<E+E_0} dx, \tag{5.8}$$

  where h is the Planck's constant. The points in phase space are denoted by x. H is the Hamiltonian of the system. This constant energy condition cannot be satisfied in real experiments and therefore ensembles that can reflect experimental conditions need to be considered [114].

- In the *Canonical Ensemble* (NVT) the system is characterized by constant particle number N, volume V, and temperature T. The system is in contact with a heat bath, allowing for energy fluctuations in order to keep the temperature of the system fixed. The probability of finding microstates of the system in a state with energy E_r, is given by [114]

  $$\rho_r^{NVT} = \frac{e^{-\beta E_r}}{\sum_r e^{-\beta E_r}} \tag{5.9}$$

  where $\beta = \frac{1}{k_B T}$, k_B the Boltzmann constant. Note that discrete notation for phase space is only for convenience and in general the phase space is continuous.

  Different strategies have been developed in order to perform MD simulations under NVT conditions. This requires a *thermostat*. Several schemes have been developed by Andersen (1980) [115], Berendsen [116] Nosé and Hoover [117, 118] (1984-1985), and Bussi et al in 2007 [119]. In this work [48, 49], we used the Langevin thermostat [120].

- *Isothermal-Isobaric Ensemble* (*NPT*): Most experiments take place at fixed temperature and fixed pressure. As such, the isothermal-isobaric ensemble can reflect the latter condition through volume fluctuations.

The probability distribution is given by [114]

$$\rho_r^{NPT} = \frac{e^{-\beta(E_r+PV_r)}}{\sum_r e^{-\beta(E_r+PV_r)}}. \tag{5.10}$$

Andersen [115] and afterwards Parrinello and Rahman [121] introduced techniques to achieve the conditions of NPT ensemble in MD simulations [101]. In this work [49], the Parrinello-Rahman [122] barostat was employed.

5.3 Combined Quantum Mechanics (GW-BSE) and Classical Mechanics

Studies of chemical reactions, (e.g. enzyme reactions), electron transfer and electronic excitations in molecules that are embedded in a larger macromolecular framework, are processes that require an explicit treatment of electrons and, hence, quantum mechanical methods are needed. However, due to the high computational cost of such techniques, they are limited to small molecules and are not applicable to systems with a lot of atoms.

One approach to study these systems is to combine quantum mechanical (QM) methods with molecular mechanic (MM) force fields (QM/MM). The QM/MM approach was first introduced by Warshel and Levitt in 1976 in their seminal paper [123]. One of the important phenomena that has gained a lot of interest is to describe optical properties of conjugated polymers surrounded by solvent molecules. Understanding how the solvent environment tunes optical properties is crucial. In QM/MM approaches, the QM part is often solved with DFT to study the ground state properties.

In this work [48, 49], electronic excitations are calculated based on Many Body Green's Functions theory within the GW approximation and the Bethe-Salpeter equation (GW-BSE) [27]. In order to describe electronic excitations of polymers, we present a QM/MM approach where the QM component is based on GW-BSE techniques. Linking GW-BSE to a classical environment, represented at atomistic resolution by a polarizable force field, allows for the determination of optical properties from the self-consistent solution of the coupled QM/MM system in realistic environments. With this new approach, it is possible to disentangle the conformational (as a result of side chain-solvent interactions) and electronic (due to local electric fields and polarization effects) contributions to the absorption spectra. Such a combined QM and MM approach can take advantage of accuracy of the GW-BSE to describe electronic excitations and of the computational efficiency of the MM calculations for the environment.

However, the method for splitting the system into QM and MM sections is not obvious. Commonly, hydrogen atoms are included to saturate the valence orbitals of the atoms at the boundary of the QM and MM regions [124]. These hydrogens will be treated quantum mechanically. The MM region acts like an external field on the QM region. Another aspect in implementation of QM/MM is the treatment of electrostatic coupling between MM and QM regions. By representing the molecules in the MM region by a set of atomic properties such as static multipole moments Q_t^a (in spherical tensor representation [125], where t indicates the multipole rank and a the associated atom) and polarizabilities, the MM region and the QM part can interact via classical electrostatic potentials. Unlike intramolecular potential, intermolecular potential is weak and can be approached perturbatively. The first-order term is called *electrostatic* and the second-order term, *polarization*, the computation of which [125] we briefly discuss in the following.

5.4 Electrostatic Contribution

Let us consider two molecules A and A' at global positions $\boldsymbol{\rho}_A$ and $\boldsymbol{\rho}_{A'}$, which consist of a set of atoms $\{a\}$ and $\{a'\}$ at positions $\mathbf{a}$ and $\mathbf{a}'$ relative to A and A', respectively. The electrostatic potential of this system is given by [125]

$$H_{AA'} = \frac{1}{4\pi\epsilon_0} \sum_{a\in A} \sum_{a'\in A'} \frac{q_a q_{a'}}{|\boldsymbol{\rho}_{A'} + \mathbf{a}' - \boldsymbol{\rho}_A - \mathbf{a}|}, \tag{5.11}$$

where q_a and $q_{a'}$ are the charges on atom a and a', respectively. Using spherical tensor formulation for $|\boldsymbol{\rho}_{A'} + \mathbf{a}' - \boldsymbol{\rho}_A - \mathbf{a}|^{-1}$ eq. 5.11 can be written as [125]

$$\begin{aligned} H_{AA'} = \frac{1}{4\pi\epsilon_0} \sum_{l_1 l_2} \sum_{m_1 m_2 m} (-1)^{l_1} \sqrt{\frac{(2(l_1+l_2)+1)!}{(2l_1)!(2l_2)!}} \underbrace{\sum_{a\in A} q_a R_{l_1 m_1}(\mathbf{a})}_{\hat{Q}^{A\text{global}}_{l_1 m_1}} \\ \times \underbrace{\sum_{a'\in A'} q_{a'} R_{l_2 m_2}(\mathbf{a}')}_{\hat{Q}^{A'\text{global}}_{l_2 m_2}} I_{l_1+l_2,m}(\boldsymbol{\rho}_{A'} - \boldsymbol{\rho}_A) \begin{pmatrix} l_1 & l_2 & l_1+l_2 \\ m_1 & m_2 & m \end{pmatrix}, \end{aligned} \tag{5.12}$$

where R_{lm} and I_{lm} are the regular and irregular spherical harmonics. Equation 5.12 is valid when $|\mathbf{a}' - \mathbf{a}| < |\boldsymbol{\rho}_{A'} - \boldsymbol{\rho}_A|$. $\hat{Q}^{\text{global}}_{lm}$ is the multipole moment operator in the global coordinate system. Using the Wigner rotation matrix $D^l_{mk}(\Omega)$ to transfer from global coordinate system to local coordinates of each molecule, $H_{AA'}$ can be written in the form below [125]

$$H_{AA'} = \frac{1}{4\pi\epsilon_0} \sum_{l_1 l_2} \sum_{k_1 k_2} \begin{pmatrix} l_1 + l_2 \\ l_1 \end{pmatrix} \hat{Q}^{A(L)}_{l_1 k_1} \hat{Q}^{A'(L)}_{l_2 k_2} \bar{S}^{k_1\ k_2}_{l_1\ l_2\ l_1+l_2} |\boldsymbol{\rho}_{A'} - \boldsymbol{\rho}_A|^{-l_1-l_2-1}, \tag{5.13}$$

where all the orientation dependence is included in $\bar{S}^{k_1\ k_2}_{l_1\ l_2\ l_1+l_2}$. By defining the interaction tensor T as [125]

$$T_{l_1 k_1, l_2 k_2} = \frac{1}{4\pi\epsilon_0} \begin{pmatrix} l_1 + l_2 \\ l_1 \end{pmatrix} \bar{S}^{k_1\ k_2}_{l_1\ l_2\ l_1+l_2} |\boldsymbol{\rho}_{A'} - \boldsymbol{\rho}_A|^{-l_1-l_2-1}, \tag{5.14}$$

$H_{AA'}$ is given by

$$H_{AA'} = \sum_{l_1 l_2} \sum_{k_1 k_2} \hat{Q}^{A}_{l_1 k_1} \hat{Q}^{A'}_{l_2 k_2} T_{l_1 k_1, l_2 k_2}. \tag{5.15}$$

Using label t and u for sequential multipoles the interaction can be written as [125]

$$H_{AA'} = \hat{Q}^A_t T^{A\ A'}_{t\ u} \hat{Q}^{A'}_u \tag{5.16}$$

For a detailed derivation of the above formulas, please see Ref. [125]. The above derivation related to molecular multipole moments can be generalized to atomic multipoles. At last, we note that CHELPG (*CHarges from ELectrostatic Potentials using a Grid based method*) point charges [126] are used in this work. With this method the atomic charges are obtained in such a way that they reproduce the molecular electrostatic potential at a number of grid points outside the molecule.

5.5 Polarization Contribution

Due to the external fields generated by other molecules, the charge distribution of a molecule can change the charge distribution of other molecules and induce polarization to the molecules. Using the Applequist model [127, 128], molecular polarizabilities can be described using atomic polarizabilities. Describing molecular polarizabilities using charge density susceptibility to account for movement of electrons from one atom to another in an external field and partition the molecule into regions a, leads to the induced moment given by [125]

$$\Delta Q_{t'}^{a'} = -\sum_{at} \alpha_{t't}^{a'a} V_t^a, \tag{5.17}$$

in which $\alpha_{t't}^{a'a}$ is called distributed polarizability and is given by [125]

$$\alpha_{t't}^{a'a} = \iint d^3\mathbf{r}\; d^3\mathbf{r}'\; \mathrm{w}^{a'}(\mathbf{r}-\mathbf{a}')R_{t'}(\mathbf{r}'-\mathbf{a}')\alpha(\mathbf{r}',\mathbf{r})\mathrm{w}^{a}(\mathbf{r}-\mathbf{a})R_t(\mathbf{r}-\mathbf{a}), \tag{5.18}$$

in which w is weight function which is defined for every region a and is 1 inside a and 0 outside a. Operator R_t describes moment t of region a. $\alpha(\mathbf{r},\mathbf{r}')$ is the charge density at $\mathbf{r}'$ in response of variation in electrostatic potential at $\mathbf{r}$. $\alpha(\mathbf{r},\mathbf{r}')$ contains how multipole element $Q_{t'}^{a'}$ at atom a' responds to the element V_t^a of the external field at atom a. V_t^a describes t derivative of potential at the center of region a. The electrostatic potential is given by

$$V_t^a = \sum_{A' \neq A} T_{tu}^{aa'} Q_u^{a'}, \tag{5.19}$$

and the polarization energy reads

$$\Delta E_A = \frac{1}{2} \Delta Q_t^a (\alpha^{-1})_{tt'}^{aa'} \Delta Q_{t'}^{a'}. \tag{5.20}$$

5.6 Total energy of the classical system

Within this framework, the total energy of the classical system of state (s) composed of A molecules comprises external (electrostatic) and internal (polarization) contributions [125]

$$E_{\mathrm{MM}}^{(s)} = E_{\mathrm{ext}}^{(s)} + E_{\mathrm{int}}^{(s)}, \tag{5.21}$$

with

$$E_{\mathrm{ext}}^{(s)} = \frac{1}{2} \sum_{A} \sum_{A'} (Q_t^{a(s)} + \Delta Q_t^{a(s)}) T_{tu}^{aa'} (Q_u^{a'(s)} + \Delta Q_u^{a'(s)}), \tag{5.22}$$

and

$$E_{\mathrm{int}}^{(s)} = \frac{1}{2} \sum_{A} \sum_{A'} \delta_{AA'} \Delta Q_t^{a(s)} (\alpha^{-1})_{tt'(s)}^{aa'} \Delta Q_{t'}^{a'(s)}. \tag{5.23}$$

Herein, $\alpha_{tt'}^{aa'}$ is the polarizability matrix describing the change in multipole moment t of atom a due to the field generated by moment t' of atom a'. Induced moments are referred to as ΔQ_t^a. The tensor $T_{tu}^{aa'}$ represents the interaction between the multipole moment Q_t^a and $Q_u^{a'}$. To avoid overpolarization, induced interactions are modified using Thole's damping functions [129, 130]. The energy follows a variational principle with respect to the induced moments and is minimized in a self-consistent procedure via iterative updates of ΔQ_t^a [125]:

$$\frac{\partial(E_{\text{ext}} + E_{\text{int}})}{\partial(\Delta Q_t^a)} = \sum_A \sum_{A'} T_{tu}^{ab}(Q_u^a + \Delta Q_u^b) + (\alpha^{-1})_{tt'}^{aa'} \Delta Q_{t'}^{a'} = 0 \tag{5.24}$$

$$\Delta Q_t^a = -\sum_A \sum_{A'} \alpha_{tt'}^{aa'} T_{t'u}^{a'b}(Q_u^b + \Delta Q_u^b), \tag{5.25}$$

and the field V_t^a is given by

$$V_t^a = \frac{1}{2} \sum_A \sum_{A'} T_{t'u}^{a'b}(Q_u^b + \Delta Q_u^b). \tag{5.26}$$

Therefore the field depends on the polarized moments of the other molecules, and hence it requires a self-consistent solutions [125].

5.7 Thole Damping

The Applequist model [127] of molecular polarizabilities using isotropic atom polarizabilities appears to be successful [128, 129, 125], however once atoms are closer to each other than a certain value the polarizability becomes infinite in this model. Nevertheless, this problem has not been encountered in reality. Thole suggested that some processes that damp the interactions must be responsible in influencing the interaction tensor T for small distances of atoms. Based on this idea, he used an empirical approach to change the interaction tensor such that it fits experimental data [129]. In his approach, he employed a smeared spherical charge distribution with a total charge of unity and introduced [125]

$$\begin{aligned} u &= \frac{|\boldsymbol{\rho}_{A'} - \boldsymbol{\rho}_A|}{S_{aa'}} \\ S_{ab} &= \left(\frac{\alpha_a \alpha_{a'}}{(4\pi\epsilon_0)^2}\right)^{\frac{1}{6}}, \end{aligned}$$

which are dimensionless universal functions where α_a and $\alpha_{a'}$ are the mean polarizabilities for atom a and a', respectively. The damped interaction tensor reads

$$\tilde{T}_{ij}^{aa'} = \frac{f_e|\boldsymbol{\rho}_{A'} - \boldsymbol{\rho}_A|^2\delta_{ij} - 3f_t(\boldsymbol{\rho}_{A'} - \boldsymbol{\rho}_A)_i(\boldsymbol{\rho}_{A'} - \boldsymbol{\rho}_A)_j}{4\pi\epsilon_0|\boldsymbol{\rho}_{A'} - \boldsymbol{\rho}_A|^5}, \tag{5.27}$$

with f_t and f_e as damping coefficients.

5.8 *GW*-BSE/MM in practice

In the QM/MM scheme used in this thesis, we restrict the static multipoles to point charges and the induced moments to dipoles. Due to the inclusion of polarization interactions, a two-level self-consistent approach is employed. Within a single iteration step m of the outer level, a QM level calculation (DFT for neutral $s = n$, DFT+GW-BSE for excited $s = x$ states) is performed in the electric field generated by the total moments in the MM region, yielding the QM energy $E_{\text{QM}}^{m,(s)} = E_{\text{DFT}}^{m,(s)} + \delta_{sx}\Omega_S^m$. The associated electron density is represented by CHELPG point charges [126], which are then used to self-consistently (inner level) determine new induced dipoles in the MM region. Since the electron density already contains the polarization response to the outside field, no atomic polarizabilities are assigned to the atoms of the QM region in this step. After subtraction of terms related to interactions already included in E_{QM} (such as the energy of the QM charge distribution in the field generated by the total MM multipoles) to avoid double-counting, the minimized classical energy $\bar{E}_{\text{MM}}^m$ is used to update the total energy of the coupled QM/MM system $E_{\text{QMMM}}^{m,(s)} = E_{\text{DFT}}^{m,(s)} + \delta_{sx}\Omega_S^m + \bar{E}_{\text{MM}}^m$. The whole procedure is repeated until the change of total energy $\Delta E_{\text{QMMM}}^{m,(s)} = |E_{\text{QMMM}}^{m,(s)} - E_{\text{QMMM}}^{m-1,(s)}|$, as well as those of the individual contributions is smaller than 10^{-4} eV. Figure 5.1 represents a schematic of the aformentioned setup.

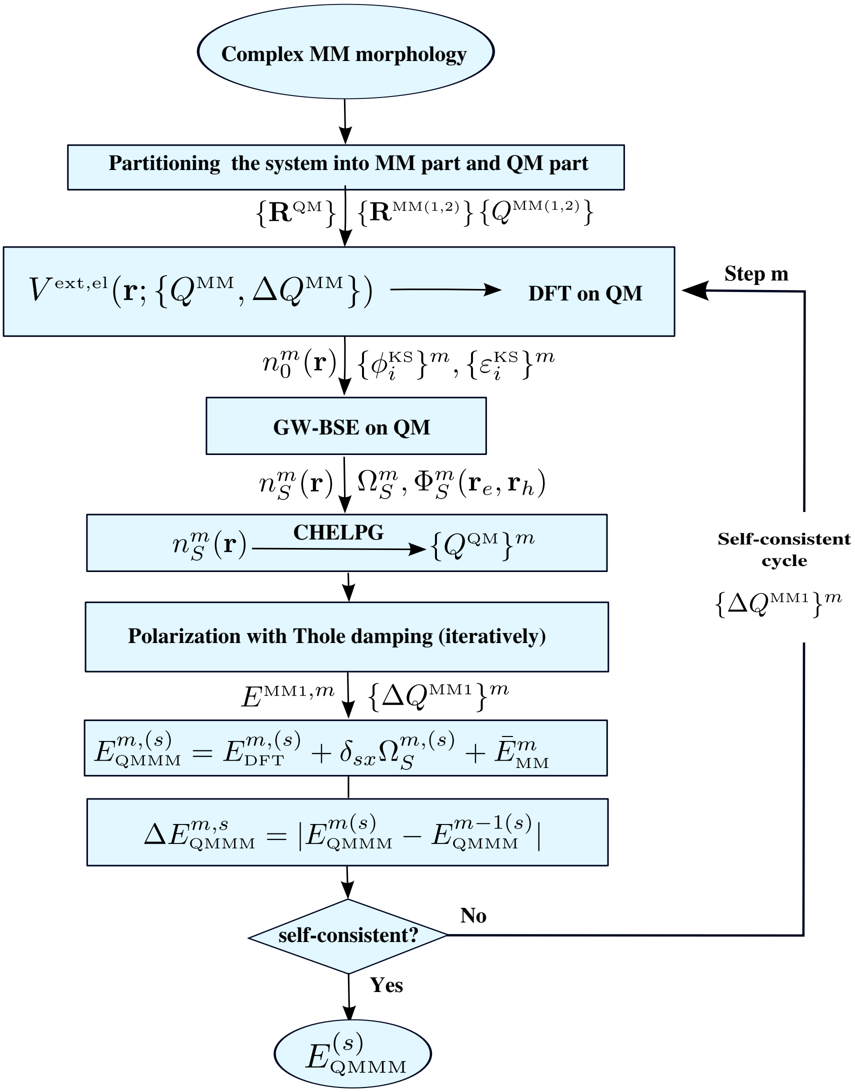

Figure 5.1: Schematic representation of Self-consistent *GW*-BSE/MM cycle.

Chapter 6

Challenges in quantum-classical studies of excitons in polymeric system

6.1 Introduction

We recall that our goal is to investigate optical properties of a class of fluorescent polymers called *poly para phenylene ethynylene* (poly-PPE) in complex morphologies. Poly-PPE (see the chemical structure in Figure 6.1) are a class of strongly conjugated polymers with a rigid backbone consisting of aromatic phenyl rings bridged by alternating single and triple carbon bonds and absorption and emission of light tunable from the ultraviolet (absorption) to the visible (emission) range [19]. Poly-PPEs can be prepared in a variety of morphologies, ranging from extended single chains to polydots, depending on the choice of functionalizing side chains and solvent combinations for processing.

Electronic excitations pose a significant challenge [28, 29, 30, 31, 32, 33, 34, 35, 36] since typical DFT methods describe the ground state. An assessment

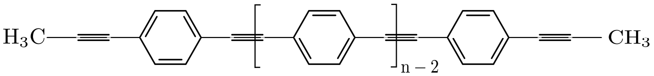

Figure 6.1: Chemical structure of poly *para* phenylene ethynylene (poly-PPE). n is the number of repeat units along the polymer (degree of polymerization).

This chapter is based on the work that was published: Behnaz Bagheri, Björn Baumeier and Mikko Karttunen, Phys. Chem. Chem. Phys., **18**, 30297-30304 (2016).

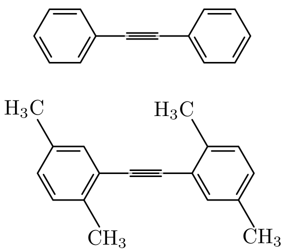

Figure 6.2: Chemical structures of diphenylethyne (DPE, top) and methylated diphenylethyne (Me-DPE, bottom). It consists of two aromatic rings bridged by a sequence of single bonds and very stiff triple bonds.

of the interplay between molecular electronic structure, morphological order, and thermodynamic properties requires the knowledge of the material morphology at atomic resolution, as well as strategies to couple quantum mechanical techniques to classical environments for accurate evaluation of electronic excitations [52, 53, 54].

Using empirical atomistic potentials in multiscale simulations of excitations based on quantum calculations requires that the structural description at different levels of resolution are compatible with each other. For example, bond length deviations or fluctuations in angles and torsions can lead to substantial artifacts if the backmapped/fine-grained geometries do not match the potential energy surfaces (PES) of the underlying quantum mechanical system. Such a situation regularly arises for conjugated polymers since conjugation can depend sensitively on conformation. In (semi) flexible polymers, conjugation along a single chain can be broken due to large out-of-plane torsions between two repeat units. Broken conjugation and wave function localization [23, 24, 25] are often intuitively interpreted based on a simple empirical criterion, the dihedral angle between two adjacent repeat units [33]. In general, details are specific to the backbone chemistry, functionalization by side chains, and solute-solvent interactions. Characteristics of conjugation also directly influence the localization behaviour of electronic excitations and hence the electronic and optical properties of the polymer.

In this chapter, some of the underlying challenges pertaining to the transfer of structural atomistic detail between quantum and all-atom resolutions are demonstrated. In particular, we consider the calculation of optical properties of poly-PPE which make them particularly attractive for use in fluorescence imaging and sensing [20, 19, 21]. Due to the importance of backbone torsions on conjugation and hence excitations, we compare PESs for phenyl rotations in diphenylethyne (DPE, see figure 1.4) obtained using density functional theory (DFT) to the ones from all-atom simulations using the standard force field and experimental data. Significant discrepancies were found and as a result, the atomistic force field was re-parameterized. With this modified force field, ground state geometries are optimized for n-PPE oligomers with $n = 1, \ldots, 10$ and then used in GW-BSE calculations. The associated excitation energies are benchmarked with results from quantum-mechanical treatment, revealing qualitatively similar characteristics as a function of n but deviations at the quantitative level.

6.2 Methodology

MM/MD calculations were performed using a force field of OPLS (optimized potential for liquid simulations) [131, 132, 133] form with GROMACS simulation software version 4 [134]. The force field parameters are taken from the polymer consistent force field [135, 136] (PCFF) as converted to OPLS form in Refs. [137, 138]. We refer to it as PCFF* from now on. The OPLS potential energy function consists of harmonic bond stretching (V_{bond}), angle bending potential (V_{angle}), non-bonded terms ($V_{\text{non-bonded}}$) including Lennard-Jones (LJ) and electrostatics, proper and improper dihedral potential terms (V_{torsion}) [131, 132, 133]:

$$V_{\text{bond}} = \sum_i k_{\text{b},i}(r_i - r_{0,i})^2 \tag{6.1}$$

$$V_{\text{angle}} = \sum_i k_{\theta,i}(\theta_i - \theta_{0,i})^2 \tag{6.2}$$

$$V_{\text{non-bonded}} = \sum_i \sum_{j>i} \Big\{ \frac{q_i q_j e^2}{r_{ij}} + 4\epsilon_{ij} \Big[\Big(\frac{\sigma_{ij}}{r_{ij}}\Big)^{12} - \Big(\frac{\sigma_{ij}}{r_{ij}}\Big)^{6} \Big] \Big\} \tag{6.3}$$

$$\begin{aligned} V_{\text{torsion}} &= \sum_i \Big[\frac{1}{2} k_{1,i}(1+\cos(\phi_i)) + \frac{1}{2} k_{2,i}(1-\cos(2\phi_i)) \\ &+ \frac{1}{2} k_{3,i}(1+\cos(3\phi_i)) + \frac{1}{2} k_{4,i}(1-\cos(4\phi_i)) \Big] \end{aligned} \tag{6.4}$$

The parameters $k_{\text{b},i}$ and $k_{\theta,i}$ are the bond force constant for bond i and angle force constant for angle i, respectively. r_0 and θ_0 are initial (reference,equilibrium) bond distance and angle bending, respectively. $k_{1,i}, k_{2,i}, \ldots$ are the torsional force constants for each dihedral i. $q_i e$ is the partial atomic charge of atom i in which e is the charge of one electron, σ_{ij} are the LJ radii and ϵ_{ij} are the LJ energies (well-depth) and r_{ij} are the distances between atom i and j. The geometric combination rules were used following the convention adopted in OPLS force field [$\sigma_{ij} = (\sigma_{ii}\sigma_{jj})^{\frac{1}{2}}$ and $\epsilon_{ij} = (\epsilon_{ii}\epsilon_{jj})^{\frac{1}{2}}$]. The intramolecular non-bonded interactions were evaluated for atom pairs separated by three or more bonds. The 1,4-intramolecular interactions were reduced [131, 132, 133] by a factor of 1/2.

To obtain relaxed scans of potential energy surfaces (PES) from MM/MD, energy minimization of the DPE molecule in vacuum was performed using the conjugate gradient method followed by a short MD run (100 ps) with constant particle number (N) and temperature (T). The Langevin thermostat [120] with 1 fs time step and open boundary conditions were applied. Temperature was kept at 10 K with 10 fs damping constant. All LJ interactions were cut-off at 1.2 nm. A plain cut-off scheme was used for electrostatic interactions with 2.0 nm real space cut-off: with open boundary conditions plain cut-off can be used. For systems with periodic boundary conditions, the particle-mesh Ewald (PME) [111, 139] should be used instead. For more discussion about the importance of electrostatic interactions, please see Ref. [105]. The cut-off distance for the short-range neighbor list was 1.2 nm and the neighbor lists were updated at every step. The intention was to evaluate the ground state energies of DPE molecules with different torsional angle between aromatic rings. To do that, after the first energy minimization step, a short MD run at very low temperature was used to bring the system out of possible local minima. Then a second conjugate gradient energy minimization was performed to obtain the ground state MM/MD PES. A detailed description on MM/MD simulations is provided in chapter 5.

DFT optimizations and relaxed PES scans were performed using the B3LYP exchange correlation functional [140, 141, 142, 143] and def2-TZVP basis set [144] as implemented in the Orca package [145]. Due to the lack of van der Waals (dispersion) interactions in standard DFT, Grimme's DFT-D3 method [146], was employed. A detailed description on DFT can be found in chapter 3.

In order to calculate electronically excited states, many-body Green's function theory in the GW approximation with the Bethe-Salpeter equation (GW-BSE) [39] was employed, since static DFT [37] cannot describe coupled electron-hole excitations. For details of the application to molecular systems, the reader is referred to Refs. [27, 40, 41, 42, 43, 44]. The GW-BSE method is based on a set of Green's function equations of motion which contain electron-hole interaction (BSE) leading to the formation of excitons. It utilizes the DFT molecular orbitals and energies to calculate the one-particle Green's function (G) and screened Coulomb interaction (W) to obtain single-particle excitations within the GW approximation as introduced by Hedin and Lundqvist [39]. An electron-hole excitation cannot be described in an effective single-particle picture but instead requires explicit treatment of a coupled two-particle system. To treat coupled excitation of an electron and hole, it uses an electron-hole state, combining single electron and hole wave functions with certain amplitudes. The electron-hole amplitudes and associated transition energies can be obtained by solving the Bethe-Salpeter equation [27, 41, 42]. For calculation of excitation energies according to GW-BSE method, first DFT calculations were performed using the Orca package [145], B3LYP functional [140, 141, 142, 143], effective core potentials of the Stuttgart/Dresden type [147], and the associated basis sets that are augmented by additional polarization functions [148] of d symmetry. The specialized GW-BSE implementation for isolated systems [40, 41, 42, 149] available in the VOTCA software package [150] is used in all further steps related to the excitations. See chapter 4 for more details. For molecular visualizations, Visual Molecular Dynamics (VMD) [151] and Jmol [152] were used.

6.3 Results

6.3.1 Force field parametrization

Due to the influence of conformational details on the optical properties [50, 51] in PPEs, one needs to determine if the force field yields reliable minimum energy configurations. Hence, relaxed scans of potential energy surface (PES) were obtained using both MM/MD and DFT.

The resulting PES are shown in figure 6.3. The PCFF* result (red triangles) shows a minimum at 90°, corresponding to twisted phenylene rings. In contrast, the result of the DFT-based scan (black squares) indicates a minimum energy configuration in which the two phenyl rings are co-planar, which is also extracted from experiments [153, 19]. The force field predicts a practically free rotation of phenylenes for $T \geq 0$, while a barrier of around $\sim 4\,\mathrm{kJ/mol}$ ($\sim 1.5\,\mathrm{k_B T}$) is obtained with DFT. The latter is comparable to the one reported in Ref. [154]. The experimental potential barrier is around $\sim 2\,\mathrm{kJ/mol}$ [153, 19, 155]. Overall, the scans imply that the PCFF* force field does not correctly model the ground state conformations of DPE, which can have severe implications for the derived optical properties.

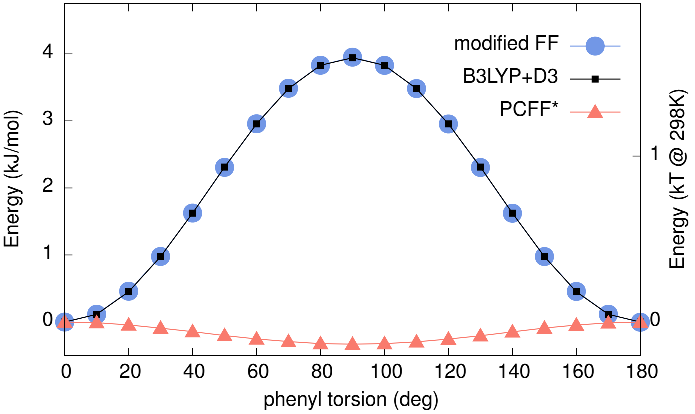

Figure 6.3: Potential energy surface (PES) obtained by MM/MD and quantum mechanical (QM) calculations. Red triangles show PES calculated using PCCF* [138, 137] force field. Black squares are the QM results using B3LYP+D3. Blue circles show PES obtained using our new modified force field. The modified force field and B3LYP+D3 are in excellent agreement.

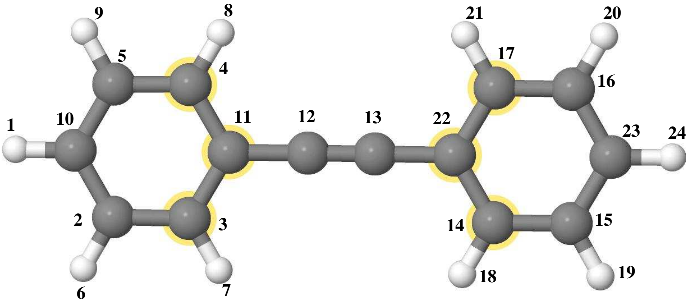

Figure 6.4: Atomic structure of DPE. Gray spheres show carbon atoms and white spheres indicate hydrogen atoms. The indices show atom number. There is a triple bond between 12 and 13.

Table 6.1: Ryckaert-Bellemans [156] torsion parameters (eq. 6.4) in kJ/mol for atom numbers 4-11-22-17, 3-11-22-14, 4-11-22-14 and 3-11-22-17, see figure 6.4 for the definition of atom numbers.

Torsion Type	k_0	k_1	k_2	k_3	k_4	k_5
C-C-C-C	1.0685	0.0007	-1.0660	0.00004	-0.00375	-0.0004

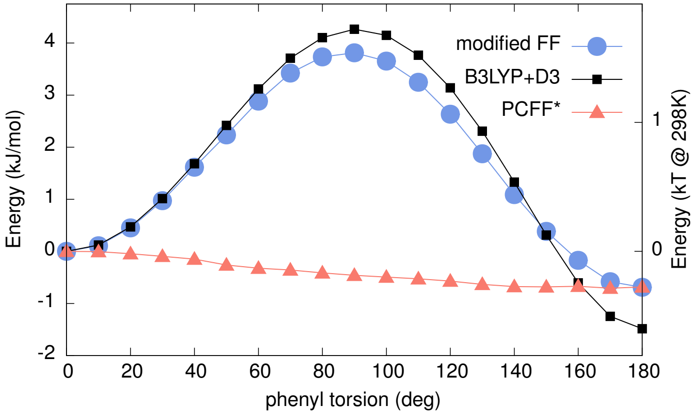

Figure 6.5: Potential energy surface (PES) obtained using the modified force field (black squares), DFT calculations (blue circles), PCFF* force field (red triangles). The modified force field gives reasonable agreement with the B3LYP+D3. Dispersion interaction between the methyl side chains leads to *cis* conformation (180°) preference over *trans* conformation (0°).

To remedy this situation, the existing force field is refined by the addition of a torsional potential between the two adjacent phenylenes (see figure 6.4 for definition of involved atoms). By fitting eq. 6.4 to the differences of DFT and PCFF* potential energy surfaces, corresponding Ryckaert-Bellemans [156] force parameters, provided in Table 6.1, were obtained. The PES is re-calculated with MM/MD using the modified force field, yielding the scan as shown in figure 6.3 (blue circles). It is in good agreement with the DFT result.

To assess the transferability of the modified force field, we repeat the above scans of the torsional potential for *para* methylated-DPE (see chemical structure shown in figure 1.4). The PES resulting from both MD and DFT calculations are shown in figure 6.5. With the modified force field (blue circles) one can observe a good agreement with the DFT data (black squares). Both approaches predict a minimum energy configuration at 180° twist. The energetic preference of this *cis* conformation of Me-DPE over the *trans* conformation (0°) is driven by attractive dispersion interaction among the two CH_3. While this preference is also obtained with the original PCFF* force field (red triangles), no barrier between *cis* and *trans* configurations is found. In terms of obtaining minimum energy configurations and energy barriers in the PES, the modified PCFF is clearly more reliable.

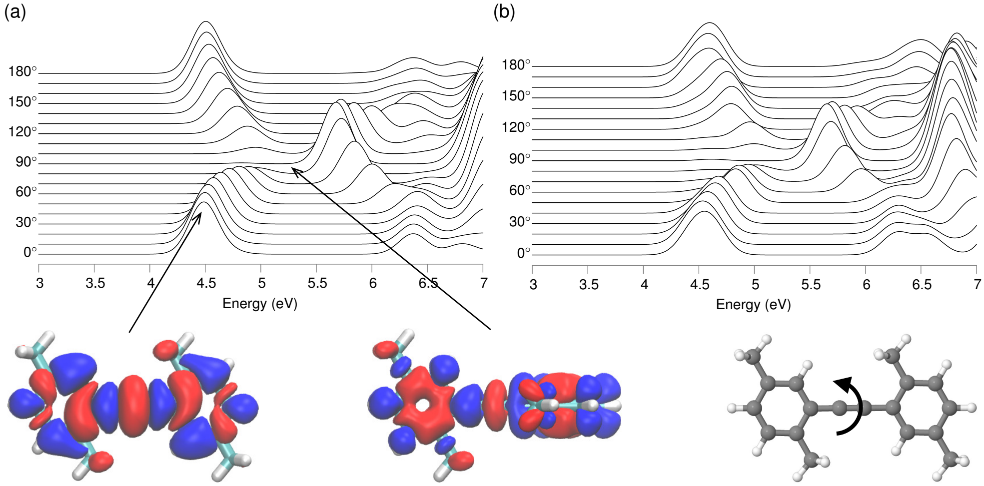

Figure 6.6: Top: Optical absorption spectra for Me-DPE as a function of torsional angle between phenylene rings based on (a) DFT optimized structures and (b) MM/MD energy minimized structures. The lower energy excitations in both (a) and (b) show the same dependency on the angle. Bottom: isosurfaces ($\pm 5 \times 10^{-3}\,\mathrm{e}/\mathrm{\AA}^3$) of excitation electron density at 0° and 90° based on DFT optimized structures. Red color corresponds to negative values (hole density) and blue color corresponds to positive values (electron density). Electron and hole densities are extended along the molecule at 0° and 90° and no localization of the excitation occurs. MAE(MAPE) of the energies underlying the spectra: S1 0.13 eV(2.7 %), S2 0.05 eV(1.1 %), S3 0.05 eV(0.7 %).

6.3.2 Optical excitations in single molecules

For systems such as solvated polymer chains, the system size makes the use of classical simulations inevitable to obtain structural information. Even with the modified force field at hand, it is not automatically guaranteed that the use of the MM/MD geometries in QM/MM schemes does not lead to spurious errors in the computed excitations. To further assess the level of reliability of such calculations, the evolution of optical absorption properties of Me-DPE is examined as a function of phenyl torsions based on the respectively optimized geometries.

The optical absorption spectra resulting from *GW*-BSE are shown in figure 6.6. DFT optimized geometries were used in (a) and MD energy minimized geometries using the modified force field were used in (b). The height of the curves indicates the strength of the excitation. Comparing both results, it is evident that the same dependency on the torsional angle is obtained by both

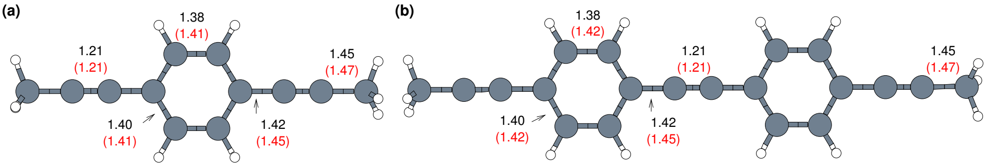

Figure 6.7: Structure of (a) 1-PPE and (b) 2-PPE. The bond length indicated by black is the result of DFT calculations and the bond length indicated by red is the result of MM/MD simulations. The bonds in the phenyl rings and the C−C bond connecting the ring to the ethyne are elongated by about 2% in MD simulations compared to DFT. The length of the C≡C triple bond results 1.2 Å in both cases.

approaches. With increasing twist from 0 ° to 90 ° the main absorption peak gradually shifts to higher energies while its strength decreases at the same time until it vanishes at 90 °. Inspection of the electron and hole densities of the excitations for co-planar and perpendicular (see bottom of figure 6.6) also reveals no localization of the excitation during the rotation confirming that the conjugation via the C≡C bond is indeed strong. The identical behavior of the lowest energy excitations (which are typically those of interest) for both MM/MD and DFT conformations indicates that the modified force field is suitable for use in QM/MM calculations.

So far the analysis has been limited to small model systems. As a next step towards more realistic system sizes, *para* phenylene ethynylene (PPE) oligomers were investigated. The geometries of single n-PPE oligomers with $n = 1, \ldots, 10$ were optimized in vacuum using both DFT (def2-TZVP [144] basis set and B3LYP functional with Grimme's D3 dispersion corrections [146]) and MD on the basis of the modified PCFF force field in vacuum at 0K. Both approaches yield planar configurations of the PPE backbone for all values of n. While qualitatively identical, quantitative differences can be observed. Most notably, the bonds in the phenyl rings and the $C - C$ bond connecting the ring to the ethyne are elongated by about 2% in MD compared to DFT. In contrast, the length of the $C \equiv C$ triple bond results 1.21 Å in both cases (see figure 6.7).

In the next step, GW-BSE calculations were performed to gauge the effect of these differences on the electronic and optical properties of the oligomers. The resulting electronic structure data, summarized in Tab. 6.2, illustrates the effects of GW-BSE with respect to the calculation of excitation energies: Taking the quasi-particle corrections to the Kohn-Sham energies into account

Table 6.2: Electronic structure data for n-PPE oligomers with $n = 1, \ldots, 10$ based on QM and MM optimized geometries: HOMO-LUMO gap from Kohn-Sham (E_g^{KS}), quasi-particle (E_g^{QP}) energies, optical excitation energy (Ω), and the contributions to it from free inter-level transitions ($\langle D \rangle$) and electron-hole interaction ($\langle K^{\mathrm{eh}} \rangle = \langle K^d + 2K^x \rangle$). All energies in eV.

	QM optimized					**MM optimized**				
n	E_g^{KS}	E_g^{QP}	Ω	$\langle D \rangle$	$\langle K^{\mathrm{eh}} \rangle$	E_g^{KS}	E_g^{QP}	Ω	$\langle D \rangle$	$\langle K^{\mathrm{eh}} \rangle$
1	4.67	8.46	5.15	9.11	-3.96	4.71	8.52	5.15	9.14	-3.99
2	3.80	7.07	4.17	7.49	-3.32	3.96	7.30	4.28	7.72	-3.44
3	3.42	6.45	3.73	6.84	-3.11	3.61	6.73	3.89	7.13	-3.24
4	3.22	6.12	3.50	6.51	-3.01	3.45	6.46	3.71	6.88	-3.17
5	3.10	5.92	3.36	6.32	-2.96	3.33	6.26	3.57	6.70	-3.13
6	3.02	5.79	3.27	6.21	-2.94	3.25	6.13	3.48	6.59	-3.11
7	2.97	5.69	3.21	6.13	-2.92	3.19	6.04	3.43	6.51	-3.08
8	2.94	5.63	3.17	6.09	-2.92	3.18	6.01	3.41	6.50	-3.07
9	2.90	5.58	3.13	6.04	-2.91	3.17	5.98	3.39	6.47	-3.08
10	2.88	5.53	3.11	6.01	-2.90	3.15	5.95	3.37	6.46	-3.09
∞			3.08					3.33		
Exp.			3.00 - 3.20							

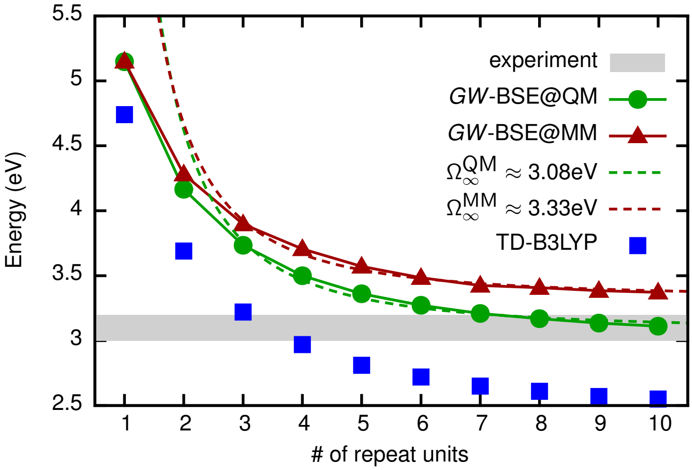

Figure 6.8: Lowest optically active excitation energies in n-PPE as the number of repeat units is increased in from n=1 to n=10. Results obtained on DFT (MM/MD) geometries are shown as green points (red triangles). For comparison, results of TDDFT calculations using the B3LYP functional are indicated as blue squares. The respective dashed lines indicate the fit to the quantum-size model. The gray shaded area indicates the width of the experimental data [19]. MEA(MAPE) of MM vs QM structures is 0.19 eV(5.6 %). MEA(MAPE) of TD-B3LYP vs *GW*-BSE is 0.53 eV(15.3 %).

increases the HOMO-LUMO gap for, e.g., the QM optimized 10-PPE from 2.88 eV to 5.53 eV, which reflects the well-known underestimation of the fundamental gap by DFT. The energy for the lowest optically active coupled electron-hole excitation gives 3.11 eV. Due to the fact that the excitation is not a pure HOMO-LUMO transition but has additional contributions from lower occupied and higher virtual single-particle orbitals, the contribution of the independent transitions, $\langle D \rangle$, is with 6.01 eV slightly larger than E_g^{QP}. The associated effectively attractive electron-hole interaction, $\langle K^{\mathrm{eh}} \rangle = \langle K^d + 2K^x \rangle$, in this structure amounts to 2.90 eV. The obtained excitation energy is in good agreement with the experimental values of 3.0-3.2 eV obtained from absorption peaks of dilute solutions of PPE in good solvents.

The results shown in figure 6.8 exhibit a monotonous decrease with n for both approaches. Such a strong size-dependence can be traced back to an increase in the size of the conjugated system. From the particle-in-a-box model, one can estimate, e.g., the optical excitation energy of an infinitely long chain via $\Omega(n) = \Omega_\infty - a/n$. By fitting the data for $n > 3$ to this model, a value of $\Omega_\infty^{\mathrm{QM}} = 3.08$ eV is obtained for QM geometries. For $n > 7$ the respective excitation energies vary only slightly and approach the region in which experimental absorption is measured in experiment [19]. This indicates that studying more complex morphologies, i.e., solvated polymers, based on oligomers with $n = 10$ is an adequate choice. For MM geometries, the absorption energies result slightly higher, evidenced by the estimate of $\Omega_\infty^{\mathrm{MM}} = 3.33$ eV. Upon further inspection, this offset of 0.25 eV with respect to $\Omega_\infty^{\mathrm{QM}}$ is a cumulative result of slight discrepancies in bond length within the phenylenes and the $C - C$ bridge bonds (see figure 6.7). In conclusion, the use of geometries determined using MM/MD in *GW*-BSE calculations can be expected to lead to slight quantitative overestimates of excitation energies. Qualitatively, however, a satisfying agreement is found. The results of TDDFT calculations using the B3LYP functional is shown with blue squares in figure 6.8 for comparison. The TDDFT result is very far from experimental results (gray shaded area).

6.4 Conclusions

A combination of atomistic (MM/MD) and DFT calculations were performed to describe conformational properties of diphenylethyne (DPE), methylated-DPE and poly para phenylene ethynylene (PPE). MM/MD simulations based on PCFF* force field were not able to provide a good description of the ground state conformation of the DPE molecule. Due to this, DFT calculations were employed to develop force field parameters to improve the MM/MD simulations. The modified force field was able to describe the conformation of methylated-DPE in agreement with DFT results. The *GW*-BSE method was utilized to describe excited states of the methylated-DPE and n-PPE polymer with $n = 1, 2, \ldots, 10$. Optical excitations were obtained for the methylated-DPE and nPPE based on MM/MD energy minimized structures using the modified force field and DFT optimized geometries. The results for methylated-DPE show that the lowest energy excitations based on the MM/MD conformations and DFT optimized geometries follow the same pattern. This nearly identical behavior for the lowest energy excitations indicates that one can describe optical excitations using the *GW*-BSE method based on MM/MD conformations. Results for the excitation energies for nPPE indicate that there is an overall agreement between the results of *GW*-BSE based on MM/MD energy minimized structures and DFT optimized geometries. There is a discrepancy of around 0.25 eV between the two. This discrepancy is a cumulative result of geometric differences between MM/MD and DFT structures. Overall agreement between MM/MD and QM based excitations is enough to validate the use MM/MD conformations as the basis for calculation of optical excitations with *GW*-BSE method.

Chapter 7

Solvent effects on optical excitations of poly *para* phenylene ethynylene

7.1 Introduction

In this chapter electronic excitations in dilute solutions of poly *para* phenylene ethynylene (poly-PPE) are studied using a QM/MM approach combining many-body Green's functions theory within the *GW* approximation and the Bethe-Salpeter equation with polarizable force field models. Oligomers up to a length of 7.5 nm (10 repeat units) functionalized with nonyl side chains are solvated in toluene and water, respectively. After equilibration using atomistic molecular dynamics (MD), the system is partitioned into a quantum region (backbone) embedded into a classical (side chains and solvent) environment. Optical absorption properties are calculated solving the coupled QM/MM system self-consistently and special attention is paid to the effects of solvents. The model allows to differentiate the influence of oligomer conformation induced by the solvation from electronic effects related to local electric fields and polarization. It is found that the electronic environment contributions are negligible compared to the conformational dynamics of the conjugated PPE. An analysis of the electron-hole wave function reveals a sensitivity of energy and localization characteristics of the excited states to bends in the global conformation of the oligomer rather than to the relative of phenyl rings along the backbone.

This chapter is based on the work that was published: Bagheri, B., Karttunen, M. & Baumeier, B. Eur. Phys. J. Spec. Top. **225** 1743-1756 (2016).

7.2 Methodology

Classical molecular dynamics (MM/MD) simulations were performed using an OPLS type (optimized potentials for liquid simulations) [131, 132, 133] force field. The parameters were taken from Refs. [137, 138] in which PCFF (polymer consistent force field) force field parameters were converted to OPLS form. Modification for torsional potential parameters of the phenylene rings as evaluated in Ref. [48] were employed. The new modified force field is available at www.softsimu.org/downloads.html. To study the behavior of PPE polymers in explicit solvents, water molecules were described using the SPC/E [157] model for water and the OPLS force field for toluene. Geometric mixing rules [$\sigma_{ij} = (\sigma_{ii}\sigma_{jj})^{\frac{1}{2}}$ and $\epsilon_{ij} = (\epsilon_{ii}\epsilon_{jj})^{\frac{1}{2}}$] for Lennard-Jones (LJ) diameters (σ) and LJ energies (ϵ) were used for atoms of different species according to the OPLS conventions [131, 132, 133]. The reader is referred to Ref. [158] for more in-depth discussion on mixing rules. Non-bonded interactions between atom pairs within a molecule separated by one or two bonds were excluded. Interaction was reduced by a factor of 1/2 for atoms separated by three bonds and more. Simulations were run using GROMACS version 5 [134]. A 1.2 nm cutoff was employed for the real space part of electrostatics and Lennard-Jones interactions. The long-range electrostatics was calculated using particle-mesh Ewald (PME) [111, 139] with the reciprocal-space interactions evaluated on a 0.16 grid with cubic interpolation of order 4. The importance of proper treatment of electrostatics in MM/MD simulations is discussed in detail in Ref. [105]. The velocity-Verlet algorithm [104] was employed to integrate the equations of motions with 1 fs time step. A Langevin thermostat [120] with a 100 fs damping was used to keep the temperature of the system at 300 K. The systems were energy minimized using the steepest descents algorithm. 100 ps simulations in constant particle number, volume and temperature (NVT) ensemble at 300 K were performed on the energy minimized systems. The simulation box size was $(15 \times 13 \times 13)\,\mathrm{nm}^3$ for dinonyl-10-PPE. Simulations were continued in constant particle number, pressure and temperature (NPT) ensemble at 300 K and 1 bar controlled by Parrinello-Rahman [122] barostat with a coupling time constant of 2.0 ps. Molecular visualizations were done using Visual Molecular Dynamics (VMD) software [151].

For practical calculations according to the *GW*-BSE method, first single-point Kohn-Sham calculations are performed using ORCA [145], the B3LYP functional [140, 141, 142, 143], effective core potentials of the Stuttgart/Dresden type [147], and the associated basis sets that are augmented by additional

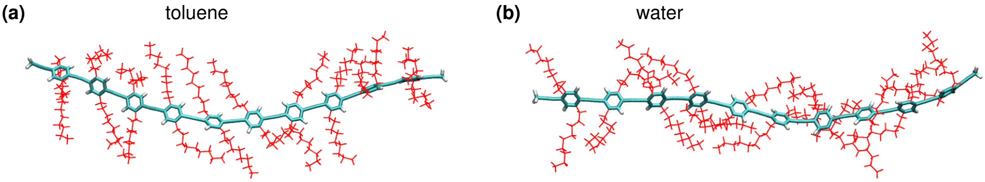

Figure 7.1: Structures of 2,5-dinonyl-10-PPE (a) in toluene and (b) in water after 7.7 ns MD simulations. (a): In toluene, the side chains are dispersed and separated from each other as well as the backbone. (b): In water, the side chains start to aggregate toward the backbone.

polarization functions [148] of d symmetry. The use of ECPs offers a computational advantage as the wave functions entering the GW procedure are smooth close to the nuclei and do not require strongly localized basis functions, keeping the numerical effort tractable. We confirmed that the Kohn-Sham energies obtained from ECP-based calculations do not deviate significantly from all-electron results. All steps involving the actual GW-BSE calculations are performed using the implementation for isolated systems [40, 41, 42, 149], available in the VOTCA software package [150]. In VOTCA, the quantities in the GW self-energy operator (dielectric matrix, exchange and correlation terms) and the electron-hole interaction in the BSE are expressed in terms of auxiliary atom-centered Gaussian basis functions. We include orbitals of s, p, d symmetry with the decay constants α (in a.u.) 0.25, 0.90, 3.0 for C and 0.4 and 1.5 for H atoms, yielding converged excitation energies. It was also confirmed that the addition of diffuse functions with decay constants smaller than 0.06 a.u. to the wave function basis set does not affect the low-lying excitations. For all systems considered in this chapter, polarizability is calculated using the full manifold of occupied and virtual states in the random-phase approximation. Quasiparticle corrections are calculated for the $2n_{\text{occ}}$ lowest-energy states, and n_{occ} occupied and n_{occ} virtual states are considered in the Bethe-Salpeter equation. Further technical details can be found in Refs [40, 41, 149].

7.3 Results

7.3.1 Structural properties of solvated 2,5-dinonyl-10-PPE

Conformations of 2,5-dinonyl-10-PPE were studied in explicit water and toluene. Water is a poor solvent for both the backbone and the side chains while toluene is a good solvent for the backbone and a poor solvent for the side

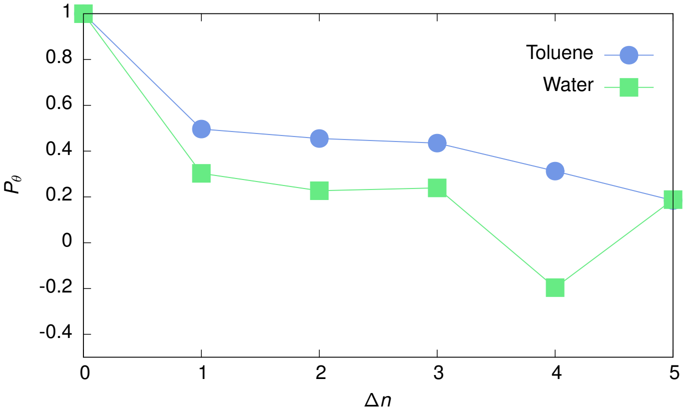

Figure 7.2: Orientations order parameter (eq. 7.1) for 10-PPE with nonyl side chains in toluene solvent (blue circles) and water (green squares). The length of MM/MD simulations for both was 7.7 ns. Time average for toluene case is taken over frames of the last 1 ns trajectory with 100 ps between the frames. In the case of water, the time average was taken over frames of the last 600 ps of the trajectory with a 100 ps step.

chains [138, 137]. figure 7.1 shows the structure of 10-PPE (a) in toluene and (b) in water at 7.7 ns. For clarity, water and toluene molecules are not shown. In toluene, the backbone remains extended and the side chains are dispersed and separated from each other as well as the backbone. This is in agreement with the results of Ref. [138]. Structural studies using small angle neutron scattering (SANS) have shown that dialkyl PPE forms a molecular solution with an extended backbone at high temperature and low concentrations [138, 159]. In water (figure 7.1(b)), the side chains start to aggregate toward each other and the backbone. This is in agreement with Ref. [137, 138]. Another important parameter is the correlation of aromatic rings along the backbone of PPE. The interplay between the arrangements of aromatic rings in PPE polymers and their electro-optical properties has been studied by several groups (see e.g. [50, 51, 160]).

The orientational order parameter[161], given by

$$P_\theta = \frac{1}{2}\langle 3\cos^2\theta - 1\rangle \tag{7.1}$$

is a measure to quantify how aromatic rings within PPE polymer backbone are correlated. θ is the angle between the normal vectors to the planes of two aromatic rings which are apart from each other by a distance Δn. P_θ

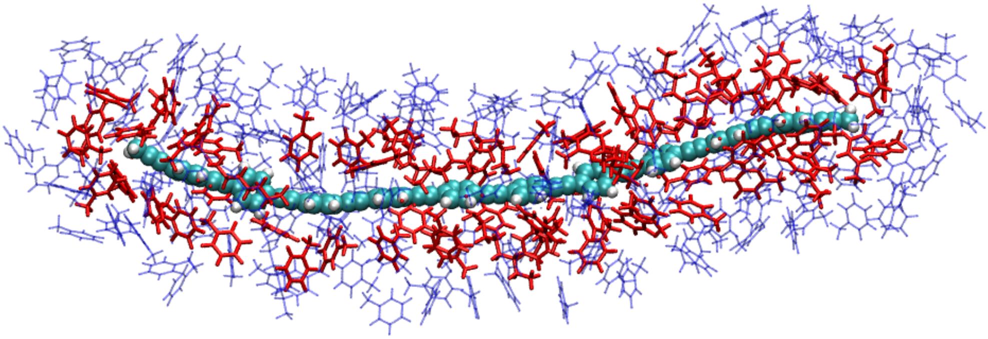

Figure 7.3: Example of *GW*-BSE/MM partitioning of the system. The oligomer is embedded into a two-layer environment of solvent molecules. Molecules within a region R_1 (red) are represented by both static atomic point charges and polarizabilities, while then ones within the extended layer R_2 (blue) are only represented by point charges.

describes the average alignment of aromatic rings. Since each vector normal to the planes of the aromatic rings can be considered as a reference direction to calculate θ and then P_θ, one needs to consider the vector normal to each plane as a reference direction and take an average: there are two averages in the calculation of P_θ, one of which is the time average over time frames and the other one is over the selection of a vector normal to the plane of the rings. P_θ can have values $[-\frac{1}{2},1]$ [161]. $P_\theta > 0$ describes a co-planar alignment of aromatic rings, while $P_\theta < 0$ indicates perpendicular alignments. $P_\theta = 0$ and $P_\theta = 1$ refer to completely random and fully co-planar alignment of the rings, respectively [138, 137]. Figure 7.2 shows the order parameter versus Δn for 10-PPE with nonyl side chains in toluene and water after 7.7 ns. The time average is taken over the frames of the last 1 ns (0.6 ns) of the MM/MD trajectory with 100 ps time step between the frames for 10-PPE in toluene (water). Having a value of around 0.4 (0.2) in toluene (water) indicates a correlation between the aromatic rings. This refers to an angle of around 39° and 47° for 10-PPE in toluene and water, respectively. In Ref. [50], the authors discussed optical properties of dialkyl and dialkoxy-PPEs in chloroform and dichloromethane, and the average angle of aromatic rings using a configuration-coordinate model in which they concluded the angle to be around 40 degrees.

7.3.2 Optical absorption of solvated 2,5-dinonyl-10-PPE

For the QM/MM calculations using the procedure described in Sec. 5.3, a two-layer scheme is employed in the MM region. Within a cutoff R_1 around the

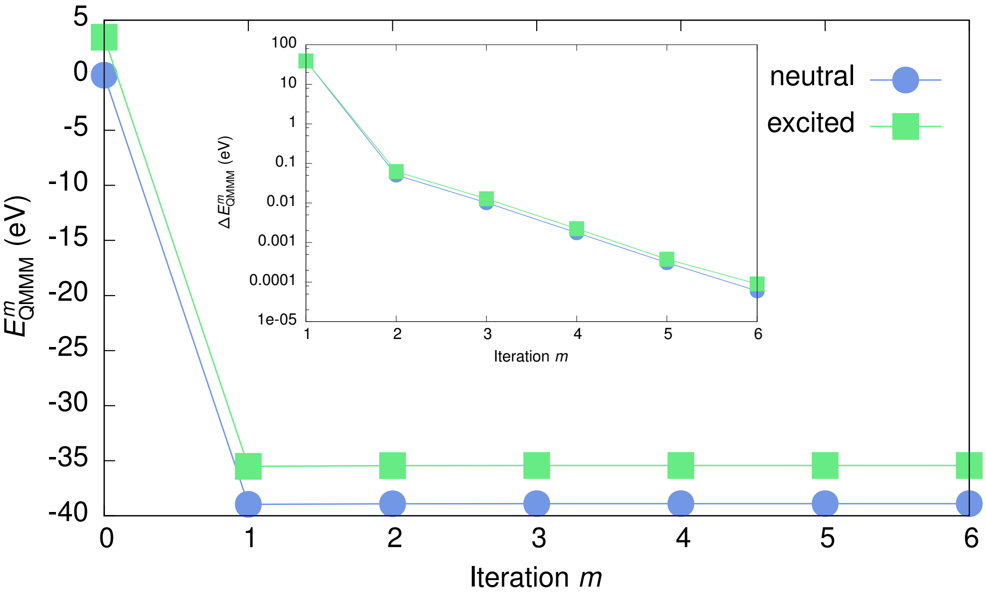

Figure 7.4: Total energies of the coupled QM/MM system (E^m_{QMMM}) for a representative snapshot at each iteration step m of the self-consistent procedure in neutral and excited states. The inset shows the respective energy differences between two subsequent iteration steps.

QM part, atomic partial and polarizable interactions are taken into account. In the more extended buffer region with $R_2 \geq R_1$, only electrostatics are active. An example for such a partitioning is depicted in figure 7.3. For a snapshot taken from the MD simulated morphology of 10-PPE with nonyl side chains in toluene, this approach is adopted using cutoffs of $R_1 = 2.5\,\mathrm{nm}$ and $R_2 = 4.0\,\mathrm{nm}$. The 10-PPE backbone is treated quantum-mechanically while the side chains and solvent molecules belong to the MM region. To split the functionalized oligomer into backbone and side chains, a link-atom approach [162] with hydrogen saturation of the backbone-side chain bridge are employed. Partial charges for the solvent molecules and side chain fragments are determined from CHELPG [126] fits to the electrostatic potentials, while the atomic Thole polarizabilities are parametrized to match the molecular polarizability tensors obtained from DFT.

Figure 7.4 shows a typical evolution of total energies of the coupled QM/MM system E_{QMMM} during the self-consistency procedure. In the evaluation of the total QM/MM energy, the contribution resulting from the interactions of the static MM partial charges is neglected, since we are ultimately only interested in total energy differences. Note that we do, however, account for the effect of the electric field of these charges on the polarizable quantum and classical parts. The zero of the energy scale is defined to correspond to the total energy of the neutral 10-PPE in vacuum (iteration $m = 0$). It is apparent that the most significant change to the total energy in both neutral and excited states occurs during the very first step of the calculation. This is further corroborated by considering the change of total energy at iteration m compared to the previous iteration as shown in the inset of figure 7.4. Within three iterations the respective changes are of the order of 0.01 eV and, more importantly, no significant differences are observed for the two states. Overall, the effect of polarization is small for the solvated 10-PPE and consequently, the excitation energy is nearly unaffected by the environment. More precisely, the excitation energy is 3.47 eV from the polarized QM/MM system, while a calculation using pure static MM yields 3.44 eV. Omitting the environment altogether, i.e., performing a GW-BSE calculation on the isolated oligomer conformation, yields 3.45 eV. The fact that environment effects only have a negligible impact on the calculated excitation energies can be attributed to a combination of the diluteness of the solution and the associated randomness of local electric fields and the small change of dipole moment between neutral and excited states. Similar observations have been made, e.g., for the optically excited states of push-pull oligomers embedded in a polarizable lattice [53].

Based on the above results, it is justified to limit the QM/MM setup to only electrostatic interactions in the following. Having realized that the direct electronic effects of solvent molecules on the excitations in 10-PPE are small, the focus is now on indirect effects that originate from the influence on the backbone conformations. To this end, 10-PPE in both toluene and water is considered and sample the conformations at different time intervals ($\Delta t = 10\,\text{fs}, 100\,\text{fs}, 1\,\text{ps}$, and $10\,\text{ps}$), all starting from an identical starting point $t_0 = 7.7\,\text{ns}$ of our MD simulations are taken (see figure 7.5). For each of these snapshots the absorption spectrum is calculated in a static MM environment defined by $R_2 = 4\,\text{nm}$ (implies $R_1 = 0\,\text{nm}$). The obtained discrete spectra of excitation energies and associated oscillator strengths are broadened by Gaussian functions with a FWHM (full width at half maximum) of 0.3 eV. It is found that the absorption properties are insensitive to structural dynamics of the backbone at time scales of 100 fs. Only for times exceeding about 500 fs fluctuations in the peak positions and heights of the spectra can be observed both in toluene and water. Figure 7.6 shows the evolution of the absorption spectrum for the time steps $\Delta t = 1\,\text{ps}$, as well as the average over the eleven

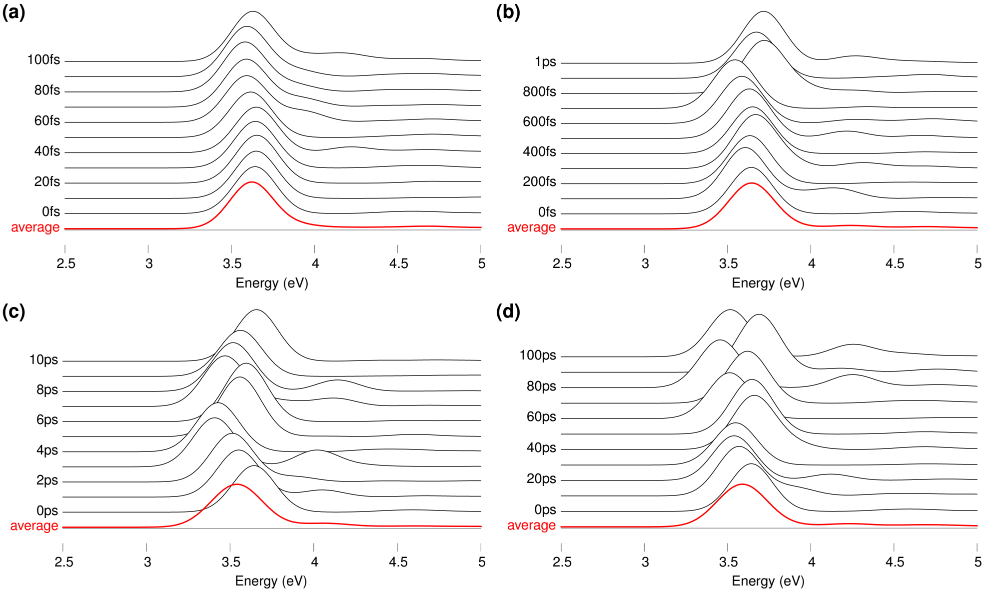

Figure 7.5: Simulated absorption spectra (broadened by Gaussian functions with a FWHM of 0.3 eV) of 10-PPE in toluene in a static MM environment ($R_2 = 4\,\text{nm}$) with a sampling time step (a) $\Delta t = 10\,\text{fs}$ (b)$\Delta t = 100\,\text{fs}$ (c)$\Delta t = 1\,\text{ps}$ (d)$\Delta t = 10\,\text{ps}$ starting from $t_0 = 7.7\,\text{ns}$. The average over the eleven respective snapshots is given in red.

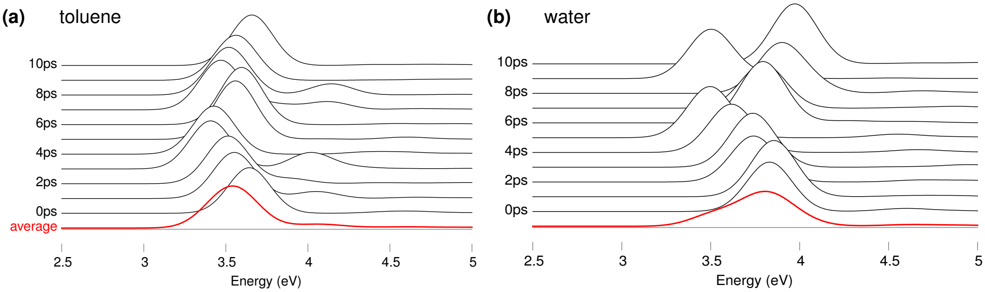

Figure 7.6: Simulated absorption spectra (broadened by Gaussian functions with a FWHM of 0.3 eV) of 10-PPE in (a) toluene and (b) water calculated in a static MM environment ($R_2 = 4\,\text{nm}$) with a sampling time step $\Delta t = 1\,\text{ps}$ starting from $t_0 = 7.7\,\text{ns}$. The average over the eleven respective snapshots is given in red.

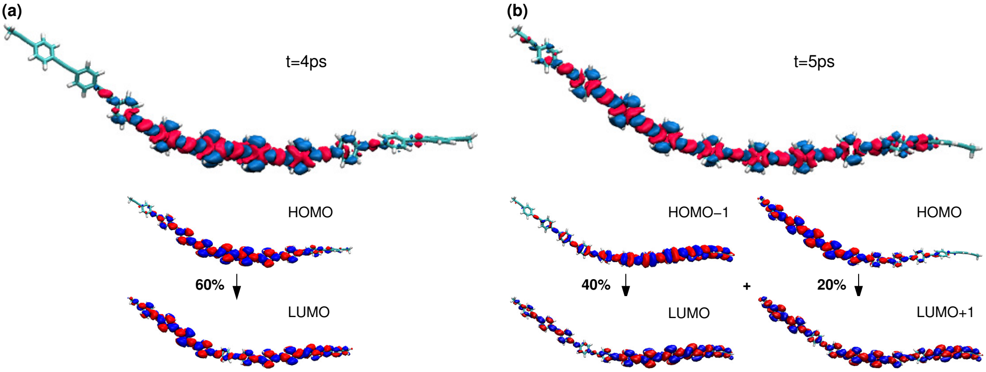

Figure 7.7: Analysis of the excited state wave functions for representative snapshots of 10-PPE in toluene. Top row: Isosurfaces of excitation electron density ($\pm 10^{-4}$e/Å^3). Red color corresponds to negative values (hole density), blue to positive values (electron density). Bottom rows: Isosurfaces of the main single-particle excitations contributing to the electron-hole wave functions (isovalue $\pm 5 \times 10^{-3}$).

respective snapshots. While the dynamics of the backbone is comparatively slow since it is to a significant extent constrained by the nonyl side chain dynamics in both poor solvents, one can observe stronger fluctuations of the absorption spectra in water as compared to toluene.

To understand the origin of these fluctuations with respect to backbone conformations in more detail, the electron-hole wave functions of the excitations is analyzed at times $t = 4\,\text{ps}$ and $t = 5\,\text{ps}$, c.f. figure 7.6(a). In the top row of figure 7.7 isosurfaces for the hole (red) and electron (blue) density distributions are shown. The overall conformation of the 10-PPE exhibits a characteristic bend as a result of the stress caused by side chain interactions. At both times, the excitation appears to be localized at the apex of the bend, more pronounced for the structure at 4 ps which is lower in energy by 0.13 eV. The different characteristics can be attributed to a slightly stronger out-of-plane bent angle between the phenylene and etynlene. Over all, co-planarity of the phenyl rings along the backbone (or the lack thereof) does not appear to affect the excitations significantly.

Analysis of the composition of the electron-hole wavefunction reveals striking differences between the two snapshots. The excitation shown in figure 7.7(a) is formed to 60% by a transition between the two frontier orbitals. The isosurfaces of these orbitals show that both HOMO and LUMO are practically extended along the full length of the backbone. Slight intensity variations can

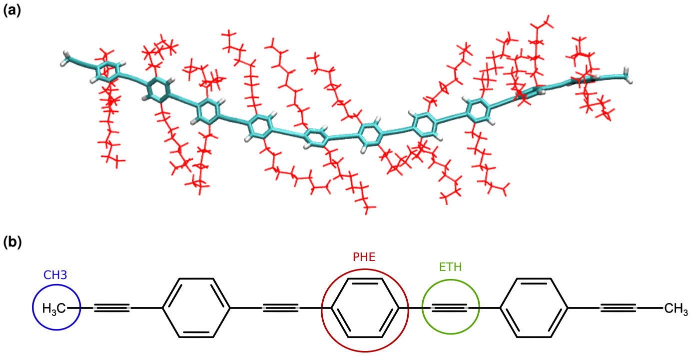

Figure 7.8: (a) Sample configuration of 2,5-dinonyl-10-PPE solvated in toluene. Nonyl side chains are indicated in red and solvent molecules are not shown for clarity. (b) Definition of three types of rigid fragments used in back mapping of the backbone conformations used in the QM/MM setup.

be noted with the HOMO being more attracted to the apex while the LUMO is thinning out at the same spot. These variations give rise to the coupled excitation being localized. At $t = 5\,\text{ps}$, in contrast, there is not a single dominant contribution to the electron-hole wavefunction. Rather, a superposition of several transitions is found, with HOMO-1 to LUMO and HOMO to LUMO+1 transitions being most significant. As can be seen in figure 7.7(b) conformational changes result in a different localization characteristics of the underlying single-particle orbitals not at the apex but left and right from it, respectively. As a pure transition between two localized states, such as the one from HOMO-1 to LUMO, is energetically penalized by stronger exchange interactions. By mixing in transitions between lower lying occupied and higher unoccupied levels, an effectively more delocalized excitation is formed. An analogous analysis of the respective excitations of 10-PPE in water, i.e, at $t = 9\,\text{ps}$ and $t = 10\,\text{ps}$, reveals qualitatively similar behaviour.

7.3.3 Absorption and emission of solvated 2,5-dinonyl-10-PPE

The 11 snapshots with a time step of 1 ps is taken from the classical MD trajectory and each of the snapshots is partitioned into a quantum (the backbone) and a classical region comprising the side chains and the solvent molecules. QM and MM regions interact via static partial charge distributions. The aim of this setup is to evaluate the excitations of the polymer backbone taking its curved conformation into account while reducing discrepancies between the force-field and QM geometries, as much as possible. At the same time, the bridging carbon-carbon bond between the phenyl 2 and 5 positions and the

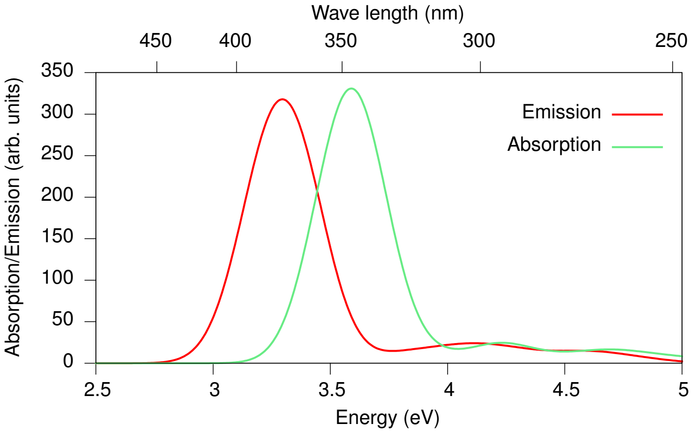

Figure 7.9: Optical absorption (blue) and emission (blue) spectra for 2,5-dinonyl-10-PPE in toluene as obtained from *GW*-BSE/MM calculations using fragment based re-mapping. Both spectra are averages over 11 snapshots taken every 1 ps, respectively. A Stokes shift (red shift) of 0.29 eV is found, which compares well to experimental observations of 0.3-0.4 eV [19].

nonyl side chain, defining the boundary between QM and MM regions, needs to be broken and the dangling bond saturated by hydrogen atom. This can be achieved with the help of a re-mapping scheme based on the definition of molecular fragments. Using centers of mass and gyration tensors, fragments of optimized QM configurations were mapped onto the orientation and alignment of the corresponding fragments in the MD configurations.

Figure 7.8(b) illustrates the re-mapping scheme for PPE. Each phenyl ring (PHE), ethyne pair (ETH), and terminal methyl group (CH3) is defined as a unique fragment. A 10-PPE backbone is hence subdivided into a total of 23 fragments (10 PHE, 11 ETH, 2 CH3) for mapping purposes.

With the re-mapped conformations at hand, the coupled *GW*-BSE/MM system is solved and the absorption spectrum determined as an average over the eleven snapshots. Individual spectra are broadened by Gaussian functions with a FWHM of 0.3 eV and the resulting spectrum is shown as a blue line in figure 7.9. It is characterized by a single peak at an energy of 3.64 eV, which is larger than the value of 3.11 eV obtained for an isolated single oligomer. This spectral blue shift is a direct result of the polymer's curvature constrained by the side chain interactions. With the re-mapping scheme it is also possible to approximate emission spectra by using excited state QM geometries as a reference. The lack of analytical forces for *GW*-BSE makes the optimization of the excited state geometries of molecules of the size of 10-PPE practically im-possible. Therefore, the geometry of the first excited state is optimized using time-dependent DFT (TDDFT), with the same functional and basis set as in the ground state. Numerical gradients of DFT/GW-BSE total energies basd on the TDDFT optimized sturcture yields very small forces. Upon excitation, electrons are promoted to higher, often anti-bonding, molecular orbitals causing an extension of bonds. Constrained by side chains, a more general modification of the overall conformation can (at least on short time scales) not be expected. Solving the GW-BSE/MM system based with excited state re-mapping yields the emission spectrum shown as a red line in figure 7.9. While the no changes in the spectral shape can be noted, the peak position of the emission is red-shifted by 0.29 eV compared to the absorption peak. This Stokes shift is in good agreement with experimental data in the range of 0.3-0.4 eV [19].

7.4 Conclusion

Electronic excitations of PPE were computed using a QM/MM approach combining many-body Green's functions theory within GW approximation and the Bethe-Salpeter equation. Conformations of solvated PPE as obtained from atomistic MD simulations were used in the mixed QM/MM setup in order to determine optical excitations of solvated PPE.

Conformations of 2,5-dinonyl-10-PPE were studied in toluene and water. The side chains were found to be dispersed from each other and from the backbone in toluene. In water, the side chains tend to aggregate. Optical excitations were calculated for 10-PPE in the QM/MM setup. The results show that the electronic environment contributions are negligible compared to the conformation dynamics of the conjugated PPE. From the analysis of the electron-hole wave function, sensitivity of energy and localization characteristics of the excited states to bends in global conformation of PPE polymer was observed.

Chapter 8

Conformational studies of solvated 2,5-dinonyl-10-PPE and 2,5-diethylhexyl-10-PPE

8.1 Introduction

In chapter 7 we discussed how the conformation and the environment affect the optical properties of PPEs with the emphasis on the influence of the classical environment. We showed that the electronic effects of the environment resulting from local electrostatics: fields and polarization are negligible compared to those from the conformational dynamics of the polymer. We also determined that the localization characteristics of the excited states and their energies are sensitive to small changes in the global conformation of a PPE molecule rather than the relative arrangements of aromatic rings. Short simulations of PPE in toluene, in which the side chains were dispersed from the extended backbone, were sufficient to reach these conclusions.

From experiment, the conformation of PPEs can be purposefully modified, e.g. by functionalizing side chains and solvent combinations. The collapse of a polymer is a result of intricate interactions between the side chains and solvent, and the associated dynamics of the polymer backbone involves much longer time scales than those addressed in chapter 7 [19, 20, 21]. To gain more detailed insight into these interactions and how they lead to complex conformations in PPEs, we study the behaviour of a short oligomer with 10 monomers (10-PPE) functionalized by nonyl and ethylhexyl side chains in toluene and water, respectively. We focus on the effects of side-chain solvent

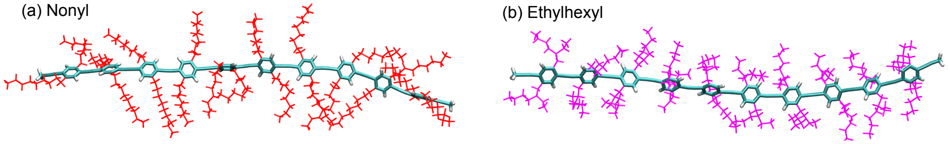

Figure 8.1: Structures of (a) 2,5-dinonyl-10-PPE and (b) 2,5-diethylhexyl-10-PPE in toluene after 66 ns and 20 ns MD simulations, respectively. In toluene, the side chains (nonyl and ethylhexyl) are dispersed and separated from each other as well as the backbone. The backbone forms an extended structure. Toluene molecules are not shown for clarity.

interactions on morphological behaviour of PPEs. As will be discussed in this chapter, the results show a variety of conformations depending on the solvent and the side chains. We measure a set of quantities to characterize these different conformations. At the end we investigate the effects of these conformational changes on the absorption spectra.

8.2 Methodology

Classical MD simulations were performed on 2,5-diethylhexyl-10-PPE and 2,5-dinonyl-10-PPE in SPC/E [157] water and toluene following the same protocol described in chapter 7. The simulations for 10-PPE with nonyl side chains in water were continued from the initial 7.7 ns [49] to longer times in a simulation box of size $(15 \times 15 \times 15)\,\mathrm{nm}^3$ in the NpT ensemble. The simulation box size for 2,5-diethylhexyl-10-PPE side chain was $(15 \times 13 \times 13)\,\mathrm{nm}^3$. For the calculation of optical spectra, the GW-BSE calculations were performed in the same way as was described in chapter 7.

8.3 10-PPE with nonyl and ethylhexyl side chains

Toluene

Toluene is a poor solvent for both ethylhexyl and nonyl side chains and a good solvent for the backbone [138, 137]. We recall that in chapter 7, the structure of 2,5-dinonyl-10-PPE in explicit toluene exhibited an extended backbone with dispersed nonyl side chains after 7.7 ns [49]. From there, MD simulations were continued until 66 ns. Furthermore, conformations of 2,5-diethylhexyl-10-PPE were studied in explicit toluene. Figure 8.1 shows representative snapshots of the structures of both 2,5-dinonyl-10-PPE and 2,5-diethylhexyl-10-PPE in toluene after 66 ns and 20 ns, respectively. For 2,5-dinonyl-10-PPE, the structure does not change significantly. Independent of the side chain, 10-PPE

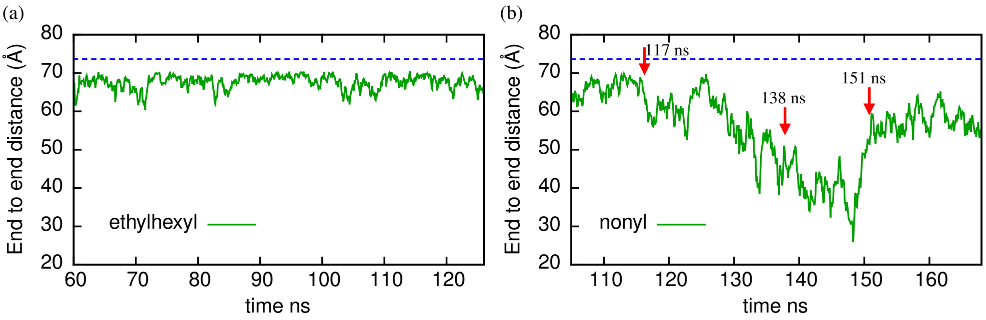

Figure 8.2: End-to-end distance of the PPE backbone with (a) ethylhexyl side chains and (b) nonyl side chains in water. In the case of ethylhexyl side chains the end-to-end distance is more uniform around 70 Å. For nonyl side chains it alters significantly due to fluctuating conformations of the polymer. The blue dashed line shows the end-to-end distance of a fully extended backbone.

forms an extended backbone with side chains separated from each other and dispersed from the backbone. These results agree with the results of Ref. [138] and small angle neutron scattering (SANS) data at high temperature and low concentrations for dialkyl PPE [138, 159].

From now on, we focus on the structural properties of 10-PPE in water.

Water

Water is a poor solvent for both the backbone and the two side chains [138, 137]. In order to describe conformational changes, the end-to-end distance is measured to obtain information about the size and the shape of the polymers.

Ethylhexyl: Figure 8.2(a) shows the end-to-end distance of the 10-PPE backbone with ethylhexyl side chains. Having a relatively constant value of about 70 Å as a function of time indicates that the backbone remains mainly extended. This can also be seen from the snapshots in figure 8.3. While the backbone remains primarily extended, the ethylhexyl side chains partially aggregate toward the backbone.

Nonyl: The end-to-end distance is shown in figure 8.2(b). Significant fluctuations occur, which imply conformational changes. Figure 8.4 shows representative snapshots of the polymer structure at different times. Until around 117 ns, the backbone is fully extended with the nonyl side chains aggregating toward the backbone, which the end-to-end distance being around 65 Å. At around 120 ns the backbone starts to bend and fluctuates between different

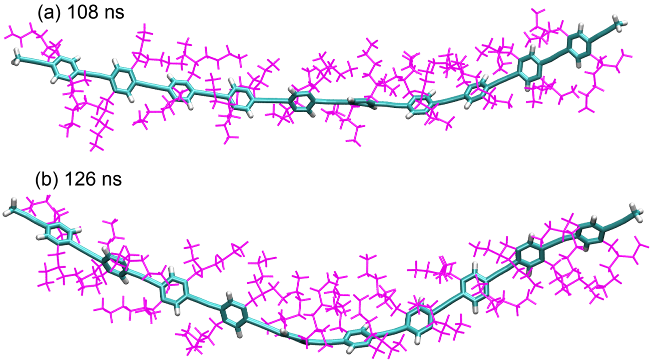

Figure 8.3: Structure of 2,5-diethylhexyl-10-PPE in water after (a) 108 ns and (b) 126 ns MD simulation. In water, the ethylhexyl side chains aggregate toward the backbone while the backbone remains extended. After 126 ns it bends, however the bend is transient.

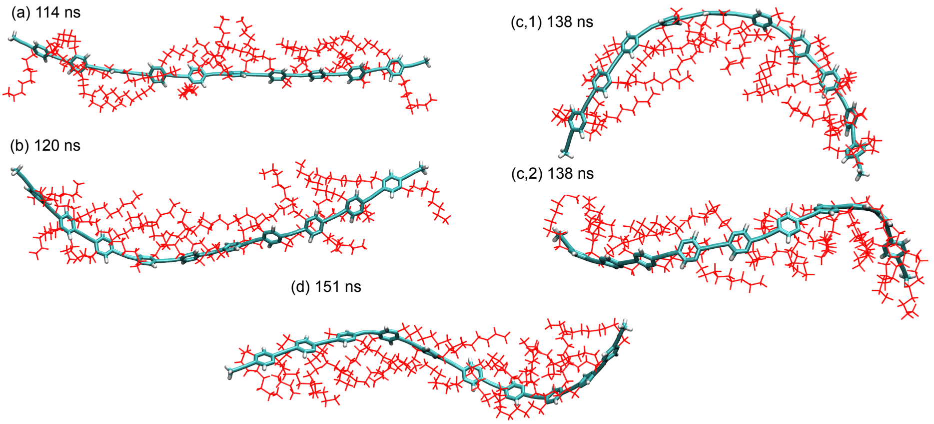

Figure 8.4: Structures of 2,5-dinonyl-10-PPE in water at (a) 114 ns, (b)120 ns, (c,1) 138 ns (side view), (c,2) 138 ns (top view) and (d)151 ns MD simulations. The nonyl side chains tend to aggregate toward the backbone. The backbone is extended at 114 ns. It starts to bend at around 120 ns forming an arc-like structure. At 138 ns, it forms a helical-like structure with the nonyl side chains all toward one side of the backbone. At 151 ns the helix has started to open.

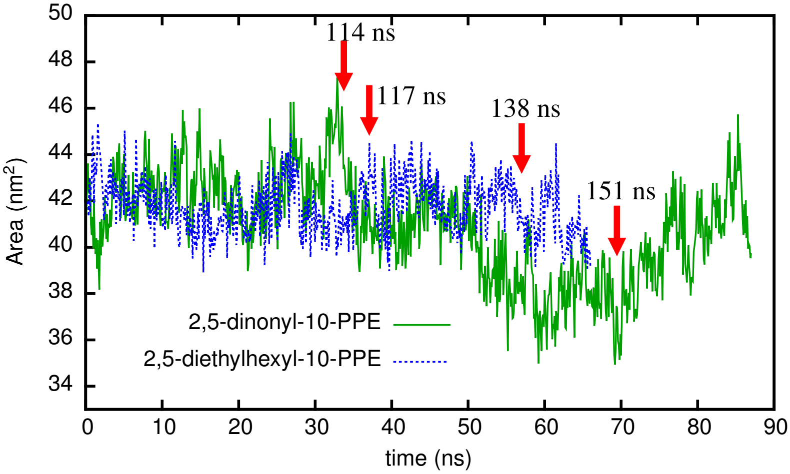

Figure 8.5: Water accessible surface area for 2,5-dinonyl-10-PPE (green line) and 2,5-diethylhexyl-10-PPE (blue dashed line). The zero refers to 81 ns and 60 ns, respectively. For 10-PPE with nonyl side chains at 117 ns the accessible surface area decreases slightly and at around 134 ns undergoes a noticeable decrease. In the case of 10-PPE with ethylhexyl it does not change significantly.

structures (arc-like structure and helical), of which none is permanent. These structural fluctuations in the backbone may be affected by the local orientations of the nonyl side chains around the backbone. At 138 ns the backbone forms a helical-structure and the side chains are all oriented toward the inside. The end-to-end distance decreases to ≈ 40 Å. At 151 ns, the backbone still has a helix-like configuration. The nonyl side chains align along the backbone. The value of end-to-end distance increases to around 55 Å. In the following we discuss possible causes of the different behaviours.

Hydrophobic interactions play a crucial role in conformational properties. Due to the exposure of the hydrophobic backbone and side chains to polar water molecules, the solvation free energy contributes to the total free energy of the system. Fully extended nonyl side chains (around 11 Å) are longer than the ethylhexyl ones (around 6 Å), and hence, the number of hydrophobic contacts of nonyl side chains is expected to be larger than ethylhexyl side chains.

Calculation of solvent accessible surface area provides an estimate of the number of water contacts. Figure 8.5 represents the calculated water accessible surface area for 10-PPE with nonyl (green line) and ethylhexyl (blue dashed

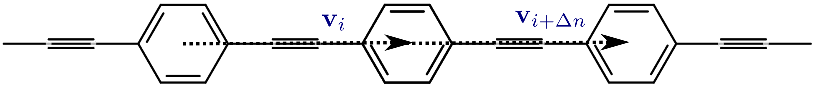

Figure 8.6: Chemical structure of PPE with the definition of tangent vectors. The persistence length of polymer can be estimated by the correlation of tangent-tangent vectors eq. 8.1. The persistence length is a measure of stiffness of the backbone of a polymer.

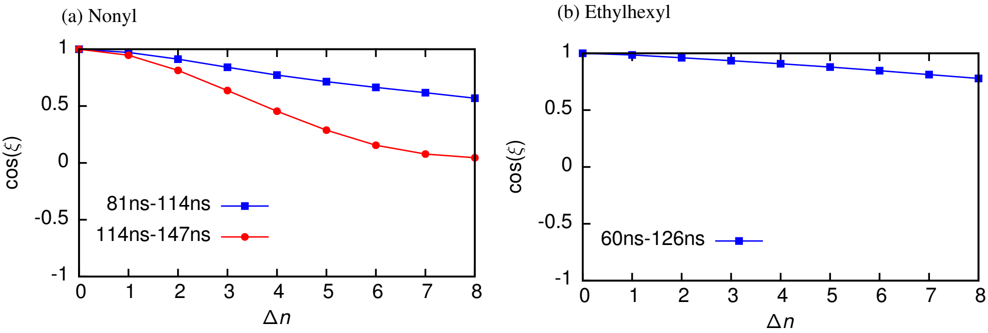

Figure 8.7: Correlation of tangent vectors along the polymer backbone in 10-PPE with (a) nonyl side chains and (b) with ethylhexyl side chains in water. In (a), the blue squares show the correlation during 81 ns-114 ns, which 2,5-dinonyl-10-PPE exhibits an extended backbone. In 114 ns-147 ns the polymer forms bent structures.

line) side chains, determined using the GROMACS implementation [163]. The time zero refers to 81 ns for nonyl and to 60 ns for ethylhexyl PPE. The water accessible surface area for nonyl side chains decreases slightly at around 117 ns. Around 134 ns it decreases more significantly, however at 160 ns, it increases again. In the case of 10-PPE with ethylhexyl side chains it exhibits small fluctuations during the 63 ns long trajectory.

In the next sections we describe the global behaviour of 10-PPE with nonyl and ethylhexyl side chains in water by calculating the persistence length and structure factor.

8.3.1 Tangent-tangent correlation and persistence length

The persistence length l_p as discussed in chapter 2, is a measure of how stiff the backbone of a polymer is [164, 165, 55, 56]. In an ideal chain model (see chapter 2), the polymer backbone can be described as a sequence of vectors $\mathbf{v}_i$ (tangent vector) with length l (see figure 8.6). The angle between neighbouring vectors is ξ. l_p characterizes the exponential decay of the backbone tangent-tangent correlation function. The polymer behaves as a flexible coil if l_p is comparable to monomer size while it is semi-flexible if l_p is much larger than a monomer size [164, 165, 55, 56].

The tangent-tangent correlations of the backbone can be calculated as

$$\cos(\xi) = \langle \mathbf{v}_i . \mathbf{v}_{i+\Delta n} \rangle, \tag{8.1}$$

where l is the monomer size. There are two averages in eq. 8.1. 1) A time average and 2) an average over all the pairs of i and $i + \Delta n$. The persistence length can be estimated when $\cos(\xi)$ decays exponentially [164, 165, 56]

$$\log(\cos(\xi)) \propto -\frac{n}{l_p} l. \tag{8.2}$$

Figure 8.7(a) shows the tangent-tangent correlation for 2,5-dinonyl-10-PPE in water for 81 ns-114 ns (blue squares) when the PPE backbone is extended and for 114 ns-147 ns (red circles) in which the backbone forms a bent structure (arc-like or helical). The different result for the two domains reveal that longer sampling time is needed to explore its conformations. Estimated l_p from 81 ns-114 ns curve is around 9.8 nm and from 114 ns-147 curve is around 11 Å.

Figure 8.7(b) shows the tangent-tangent correlation for 2,5-diethylhexyl-10-PPE in water. The persistence length from this curve can be estimated to be around 24.5 nm. The larger persistence length of 10-PPE with ethylhexyl side chains compared to nonyl side chains reveals that 2,5-diethylhexyl-10-PPE is stiffer. Our result for the persistence length are in the same range as the result of electron paramagnetic resonance (EPR) measurements and light scattering experiments that obtains a persistence length of the order of 11 nm to 15 nm for different side chains [166, 167, 168].

8.3.2 Structure Factor

Experimentally, polymer conformations are usually studied using different scattering experiments such as light scattering, small angle X-ray scattering and small angle neutron scattering. These methods are based on contrast

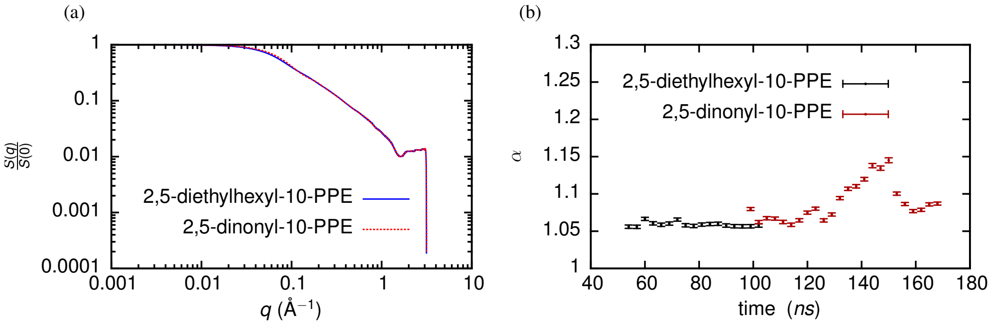

Figure 8.8: (a): The structure factor for PPE backbone for 2,5-diethylhexyl-10-PPE (blue) and 2,5-dinonyl-10-PPE in water (red). The values $q > 0.04\text{Å}^{-1}$ might be caused by the terminal ends. (b): In the intermediate q region ($q \in (0.04, 1.6)\text{Å}^{-1}$), $S(q)$ exhibits a power law dependence ($q^{-\alpha}$). The power α in different 3 ns time domains for PPE backbone with ethylhexyl side chain (black) and nonyl side chain (red) in water. For both 2,5-diethylhexyl-10-PPE and 2,5-dinonyl-10-PPE, α has a value around 1 and PPE backbone behaves like a rigid rod.

between the polymer and its environment [55, 56] and provide information about the shape of the polymer.

The structure factor can be computed using [169]

$$S(\mathbf{q}) = \int g(\mathbf{r}) e^{i\mathbf{q}.\mathbf{r}} d\mathbf{r}, \tag{8.3}$$

where $g(\mathbf{r})$ is the pair correlation function which gives the probability of finding a monomer in a unit volume at a distance $\mathbf{r}$ of a given monomer [55]. $\mathbf{q}$ is the scattering wavevector. By assuming that all the orientations of the polymer is equally probable, the structure factor for low angle scattering can be obtain as

$$S(q) = \int g(r) \frac{\sin(qr)}{qr} dr, \tag{8.4}$$

and the scattering intensity can be computed as

$$I(q) = \frac{S(q)}{S(0)} = \frac{\int g(r) \frac{\sin(qr)}{qr} dr}{\int_0^\infty g(r) dr}. \tag{8.5}$$

We modified the GROMACS implementation [169] for calculating the scattering intensity to make it work for our force field. $S(q)$ as a function of q calculated based on the positions of the bare backbone is shown in figure 8.8(a).

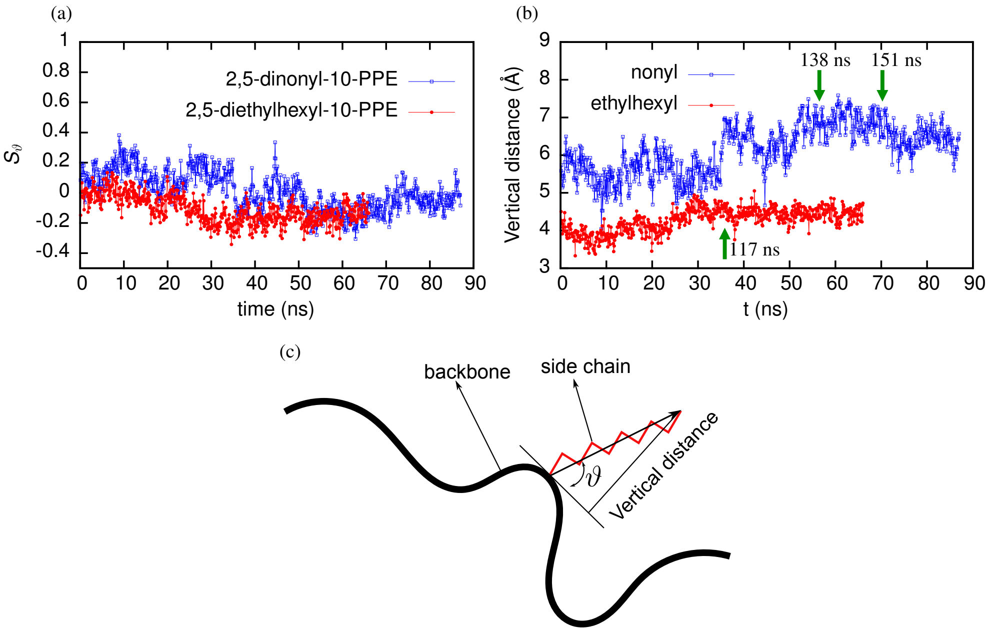

Figure 8.9: (a): Orientation of the side chains relative to the local tangent of the backbone (S_ϑ) for 2,5-dinonyl-10-PPE (blue squares) and 2,5-diethylhexyl-10-PPE (red circles). (b): Average vertical distance of the side chains with respect to the respective local tangents for 2,5-dinonyl-10-PPE (blue squares) and 2,5-diethylhexyl-10-PPE (red circles). The time zero refers to 81 ns for nonyl case and 60 ns for ethylhexyl. (c): Schematic representation of the angle ϑ and the vertical distance.

In the intermediate q region, $S(q)$ exhibits a power law dependence $q^{-\alpha}$. The values of α at different time regions of length 3 ns are shown in figure 8.8 (b). α remains at a constant value of ≈ 1 for the PPE backbone with ethylhexyl side chain. For the nonyl case there are larger fluctuations. The results support that on average the backbone behaves like a rigid rod in both cases.

8.3.3 Correlation of the side chains along the backbone

We discussed that the water-side chains interactions might be the cause of different observed conformations. We seek to measure a quantity describing the correlation of the alignments of the side chains with respect to the backbone. Inspired by the nematic order parameter in liquid crystals, we define

$$S_\vartheta(t) = \frac{1}{2}\langle(3\cos^2(\vartheta(t)) - 1)\rangle_n. \tag{8.6}$$

S_ϑ is the second Legendre polynomial [170] and $\vartheta(t)$ is the angle between the orientation of the side chains to the local tangent of the backbone (see figure 8.9(c)). The local tangent of the backbone is defined by a pair of carbon atoms of the aromatic rings (the two carbon atoms that are connected to the linkers) which build a vector along the backbone. The orientation of the side chains is defined by a vector connecting the first carbon atom of the side chain to the last one (see figure 8.9(c)). S_ϑ tells us whether the arrangements of the side chains toward the backbone are collective (non-zero) or random (zero).

The computed S_ϑ for 10-PPE with nonyl (blue squares) and ethylhexyl (red circles) side chains in water are shown in figure 8.9(a). The results indicate a random orientation in both cases. Furthermore, the vertical distance of the side chains to the local tangent of the backbone (see figure 8.9(c)) is calculated. Figure 8.9(b) shows the results. The average vertical distance of the side chains to the local tangent vector of the backbone changes. The backbone is extended until 117 ns, with the average vertical distance around 5 Å. However, once the backbone starts to bend (after 120 ns), the vertical distance increases. The vertical distance is more uniform for ethylhexyl side chains.

8.3.4 Dihedral-distribution

In chapter 6, we modified the existing force field in such a way that it yields reliable relaxed structures compared to experiments and quantum mechanical calculations [48]. The force field was refined by adding a Ryckaert-Bellemans [156] torsional potential between neighbouring phenylene rings of diphenylethyne (DPE).

In this section we study the effects of different side chains and explicit water solvent on the torsional potential profile. To this end, the dihedral distribution and the corresponding potential of mean force were calculated. It was also done for the bare backbone in explicit water to understand what are the effect of side chains to the torsional potential profile. The corresponding dihedral distributions are shown in figure 8.10(a).

The potential of mean force ($U(\phi)$) can be evaluated by converting the dihedral distribution using the Boltzmann factor [165]

$$P(\phi) = \frac{e^{-\beta U(\phi)}}{\int e^{-\beta U(\phi')} d\phi'}, \tag{8.7}$$

where $P(\phi)$ is the probability distribution and $\beta = \frac{1}{k_\mathrm{B} T}$. By inverting eq. 8.7 we estimate of the effective potential of mean force.

The results are shown in figure 8.10(b). The resulting DFT calculations

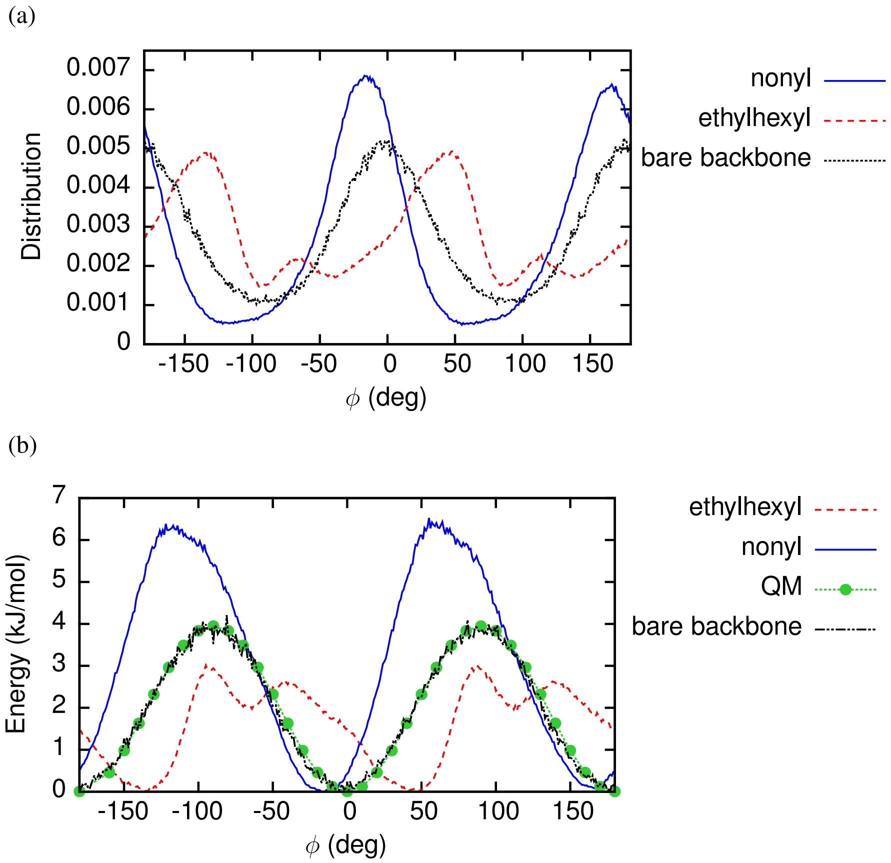

Figure 8.10: (a): Distribution of dihedral angles between the neighbouring phenylene rings in 10-PPE with nonyl side chains (blue line) and ethylhexyl side chains (red dashed line) in explicit water solvent during 63 ns and 66 ns, respectively. The dihedral distribution for the bare backbone in water calculated during 15 ns trajectory is shown with black line. (b): The effective potential mean force calculated using Boltzmann factor eq. 8.7 for 10-PPE with nonyl side chains (blue line), ethylhexyl side chains (red dashed line), and bare backbone (black line) in explicit water using the dihedral distribution shown in (a). The green circles show the DFT potential energy surface for DPE molecule that we added to the existing forcefield.

using B3LYP-D3 for DPE at $T = 0$ K are shown for comparison. The DFT calculation and therefore our modified force field for DPE gave a barrier of around ≈ 4 kJmol^{-1} ($\approx 1.5\ k_{\mathrm{B}}T$) at 90° twist. The dihedral potential of mean force for the bare backbone with 10 monomers in water matches the DFT one (see figure 8.10). Therefore, we can conclude that the interaction between water and the backbone does not affect the phenyl torsions.

The potential of mean force for 10-PPE with nonyl side chains follows almost the same pattern as the DFT one. However, the barrier is increased to ≈ 6 kJmol^{-1} ($\approx 2.5\ k_{\mathrm{B}}T$) and the minimum shifts toward $\approx -20°$. The ethylhexyl side chains shift the minimum to $\approx 50°$ and decrease the barrier to ≈ 3 kJmol^{-1} ($\approx 1.2\ k_{\mathrm{B}}T$). The potential of mean force for ethylhexyl side chains is asymmetric with a local minimum at $\approx 110°$.

The torsional potential profile is strongly dependent of the type of side chain. This asymmetric behaviour for ethylhexyl may be caused by its branched structure. In the next section the order parameters for the phenylene rings are calculated in order to understand the consequences of the changes in the torsional potential profile in arrangements of the aromatic rings.

8.4 Orientational correlations

Order parameter

As we mentioned in chapter 7, the orientational order parameter [161] is given by

$$P_\theta = \frac{1}{2}\langle 3\cos^2\theta - 1\rangle. \tag{8.8}$$

It is a measure of quantifying the correlations of aromatic rings within the polymer backbone. θ is the angle between the normal vectors to the planes of two aromatic rings which are separated by a distance Δn. The calculation of P_θ was described in chapter 7.

Figures 8.11 (a) and (b) show the order parameter versus Δn for 2,5-dinonyl-10-PPE in water for different portions of the MD trajectory. The blue squares in figure 8.11(a) show the order parameter for a trajectory from 81 ns to 114 ns. In this domain the backbone is extended. Having a small positive value characterizes a co-planar orientation of the aromatic rings. The red circles and green triangles show the order parameter for a trajectory from 114 ns to 147 ns and 147 ns to 174 ns, respectively. The results demonstrate that the orientation of the aromatic rings along the backbone and the global structure of the backbone are not independent from each other.

In order to understand the different arrangements of the aromatic rings

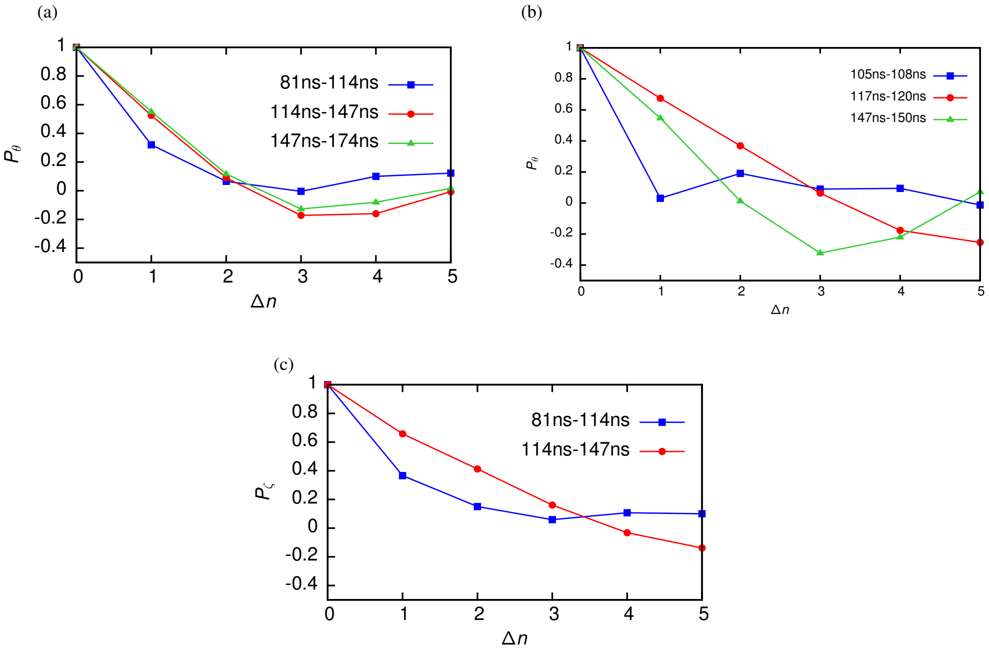

Figure 8.11: (a) and (b): Orientation order parameter P_θ for the normal vectors to the aromatic rings (eq. 8.8) for 2,5-dinonyl-10-PPE in water for different portions of the MD trajectory. (c): Order parameter P_ζ for $\mathbf{w}$ vectors (eq. 8.9) for 2,5-dinonyl-10-PPE in water.

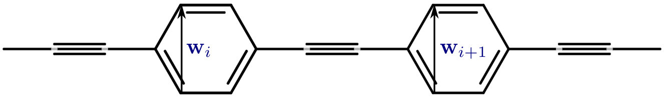

Figure 8.12: Chemical structure of PPE and the definition of **w** vectors for the monomers. The order parameter (see eq. 8.9) of these vectors obtains the arrangements of the rings with respect to the global conformation of the polymer.

when the transition from extended structure to bent occurs, P_θ is calculated for shorter time domains of 3 ns (figure 8.11(b)). In 105 ns-108 ns the backbone is extended, in 117 ns-120 ns the backbone starts to form an arc-like structure and 147 ns-150 ns the helical backbone has started to open. The results show that in the regions where the backbone is extended the rings are more randomly oriented. In the regions in which the polymer bends, the arrangements of aromatic rings are correlated.

The order parameter to the normal of the rings gives the relative arrangements of the aromatic rings. However, it does not yield the arrangements of the rings with respect to the global conformation of the polymer. Because of that, the arrangement of aromatic rings along the backbone can be studied by defining the order parameter for vectors $\mathbf{w}_i$ and $\mathbf{w}_{i+\Delta n}$ (see figure 8.12):

$$P_\zeta = \frac{1}{2}\langle 3\cos^2\zeta - 1\rangle, \tag{8.9}$$

ζ is the angle between $\mathbf{w}_i$ and $\mathbf{w}_{i+1}$. Figure 8.11(c) shows the calculated P_ζ for 2,5-dinonyl-10-PPE in water for 81 ns-114 ns (blue squares) in which the PPE backbone is extended and for 114 ns-147 ns (red circles) in which the backbone forms a bent structure. P_θ and P_ζ have the same pattern for extended backbone. For the domains that the backbone forms bent structure P_θ and P_ζ exhibit different behaviour.

In figure 8.13 the calculated order parameter for 2,5-diethylhexyl in water are shown. P_ζ and P_θ exhibit the same behaviour indicating an extended backbone. Moreover, the value of P_θ and P_ζ is around 0.2, which points to correlations between aromatic rings. This value corresponds to an average angle of around 47° between neighbouring aromatic rings. This agrees with the result of section 8.3.4 for dihedral potential of mean force for ethylhexyl

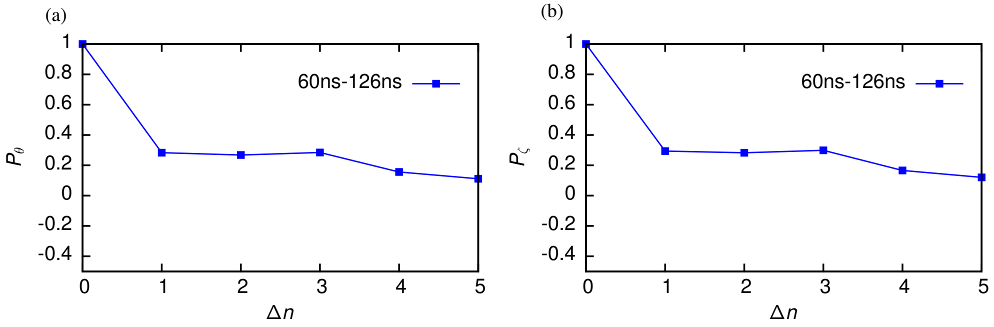

Figure 8.13: (a): order parameter P_θ for the normal of the aromatic rings for 2,5-diethylhexyl-10-PPE in water. (b): order parmeter P_ζ for **w** vectors for 2,5-diethylhexyl-10-PPE in water.

side chains, which exhibits a minimum at 50°.

Autocorrelation of the normal vectors to the rings

The autocorrelation function provides an estimate of the time scales that are needed for the PPE to be equilibrated. We computed the autocorrelation function $\langle n(t)n(0)\rangle$, where $n(t)$ is the normal to the plane of the rings [171]. Figure 8.14 (a) shows the autocorrelation of 10-PPE with nonyl side chains in water (blue circles). The red dashed line shows the fit to a triexponential decay formula $y = A_1 e^{\frac{-t}{\tau_1}} + A_2 e^{\frac{-t}{\tau_2}} + A_3 e^{\frac{-t}{\tau_3}}$ where τ_1, τ_2, and τ_3 are the characteristic relaxation times. The fit yields the three time scales as the follows: $\tau_1 = 600.59\,\text{ps} \pm 22.72\,\text{ps}$, $\tau_2 = 6.41\,\text{ns} \pm 0.16\,\text{ns}$, and $\tau_3 = 25.74\,\mu\text{s}$. τ_3 corresponds to the dynamics of the global structure of the polymer in water, and describes the relaxation time of the global structure of the backbone. τ_2 represents the time required for the rotation of the rings along the backbone to be uncorrelated. The fast motion of the terminal ends of the backbone is related to τ_1.

In figure 8.14 (b), the autocorrelation function for 10-PPE with ethylhexyl side chains is shown (blue circles). The dashed line shows the fit to a biexponential decay formula $y = A_1 e^{\frac{-t}{\tau_1}} + A_2 e^{\frac{-t}{\tau_2}}$. The following time scales were obtained in 2,5-diethylhexyl-10-PPE: $\tau_1 = 192.44\,\text{ps} \pm 6.78\,\text{ps}$, and $\tau_2 = 7.59\,\text{ns} \pm 0.01\,\text{ns}$. In the ethylhexyl case there are only two time scales: as for the nonyl case, τ_2 is related to the time required for the motion of phenylene rings to become uncorrelated. The fast time scale τ_1 is related to the motion of terminal ends of the backbone. A third time scale of the order of $\mathcal{O}(\mu s)$ does not appear for PPE with ethylhexyl side chains, since the polymer

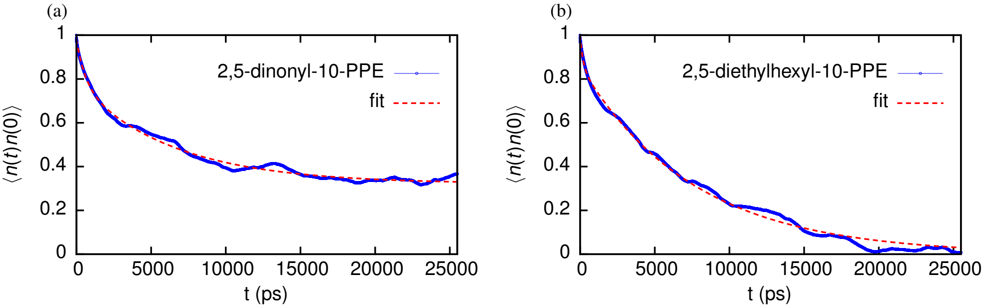

Figure 8.14: (a): The autocorrelation for 10-PPE with nonyl side chains in water (blue circles). The red dashed line shows the fit to triexponential decay formula ($y = A_1 e^{\frac{-t}{\tau_1}} + A_2 e^{\frac{-t}{\tau_2}} + A_3 e^{\frac{-t}{\tau_3}}$) which yields $\tau_1 = 600.59\,\mathrm{ps} \pm 22.72\,\mathrm{ps}$, $\tau_2 = 6.41\,\mathrm{ns} \pm 0.16\,\mathrm{ns}$, $\tau_3 = 25.74\,\mu\mathrm{s}$, $A_1 = 0.32$, $A_2 = 0.46$, and $A_3 = 0.2$. (b): Autocorrelation for 10-PPE with ethylhexyl side chains. The red dashed line shows the fit to biexponential decay function ($y = A_1 e^{\frac{-t}{\tau_1}} + A_2 e^{\frac{-t}{\tau_2}}$) with the following time scales: $\tau_1 = 192.44\,\mathrm{ps} \pm 6.78\,\mathrm{ps}$, $\tau_2 = 7.59\,\mathrm{ns} \pm 0.01\,\mathrm{ns}$, $A_1 = 0.138$, $A_2 = 0.86$.

does not bend due to a longer persistence length ($l_p \approx 24.5\,\mathrm{nm}$) than PPE with nonyl side chains ($l_p \approx 9.8\,\mathrm{nm}$) (see section 8.3.1).

Autocorrelation of the tangent vectors

In order to obtain the time scales that are required for the dynamics of the polymer along the backbone to be uncorrelated, the autocorrelation for the tangent vectors $\langle \mathbf{v}(t)\mathbf{v}(0) \rangle$ (see figure 8.6 for the definition of tangent vectors) was calculated and is shown in figure 8.15. In (a), the autocorrelation for the nonyl side chains is shown with blue line. The red dashed line shows the fit to a biexponential decay formula with the following time scales: $\tau_1 = 5.91\,\mathrm{ns} \pm 0.08\,\mathrm{ns}$, and $\tau_2 = 160.54\,\mathrm{ns} \pm 0.96\,\mathrm{ns}$. In (b), the autocorrelation of 2,5-diethylhexyl-10-PPE in water is shown. The fit yields the following time scales: $\tau_1 = 2.41\,\mathrm{ns} \pm 0.03\,\mathrm{ns}$, $\tau_2 = 127.19\,\mathrm{ns} \pm 0.14\,\mathrm{ns}$. τ_2 is the time scale that is required for the dynamics of tangent vectors to be uncorrelated along the backbone. This can be attributed to l_p, which yields the length scale that the tangent vectors lose their initial memory. τ_1 is the time scale for the rotation of tangent vectors to become uncorrelated.

8.5 Optical absorption

The result of QM/MM calculations on solvated 2,5-dinonyl-10-PPE in chapter 7, using a two layer scheme for the MM region, revealed that the excitation en-

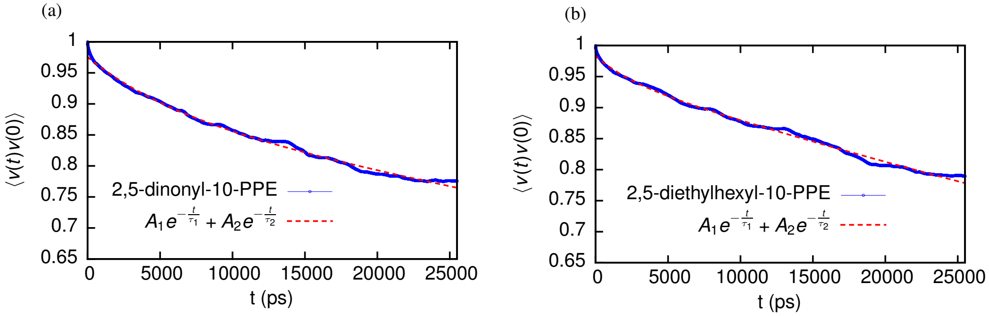

Figure 8.15: Autocorrelation for the tangent vectors. (a): 2,5-dinonyl-10-PPE (blue circles). (b): 2,5-diethylhexyl-10-PPE (blue circles). Red dashed line shows the fit to biexponential decay function ($y = A_1 e^{\frac{-t}{\tau_1}} + A_2 e^{\frac{-t}{\tau_2}}$) which yields $\tau_1 = 5.91\,\text{ns} \pm 0.08\,\text{ns}$, $\tau_2 = 160.54\,\text{ns} \pm 0.96\,\text{ns}$, $A_1 = 0.08$, and $A_2 = 0.89$ for 2,5-dinonyl-10-PPE. For 2,5-diethylhexyl-10-PPE the fit yields the following: $\tau_1 = 2.41\,\text{ns} \pm 0.03\,\text{ns}$, $\tau_2 = 127.19\,\text{ns} \pm 0.14\,\text{ns}$, $A_1 = 0.03$, and $A_2 = 0.95$.

ergies are hardly affected by the electrostatic environment but are strongly influenced by the structural changes of the polymer. In this section we aim to calculate the absorption spectra for different configurations of 2,5-dinonyl-10-PPE.

We consider a purely static environment with cutoffs $R_2 = 4.0\,\text{nm}$ and $R_1 = 0\,\text{nm}$. The backbone is treated quantum mechanically while the solvent and side chains belong to the MM region. The same procedure as described in chapter 7 is employed. In chapter 7, we found that the absorption spectrum is sensitive to structural dynamics of the backbone at time scales of 500 fs and above. As such, 1 ps time scale may be adequate to see the changes in absorption spectra as a result of the changes of the polymer structure. Therefore, we sample the conformations with $\Delta t = 1\,\text{ps}$ time intervals, starting from $t_0 = 114\,\text{ns}$ (extended), $t_0 = 138\,\text{ns}$ (helix), and $t_0 = 151\,\text{ns}$ (opened helix).

The calculated discrete spectra of excitation energies and the associated oscillator strengths are broadened by Gaussian functions with a FWHM of 0.3 eV. The evolution of the absorption spectrum for time steps of $\Delta t = 1\,\text{ps}$ for different starting points of MD simulations is shown in figure 8.16. At each starting point t_0, the dynamics of the backbone is very slow on time scales of the order of 1 ps. For all three starting points, significant fluctuations in the positions and the heights of the peaks emerge. At some time steps double peaks appear while they later merge to a single one. This trend holds for

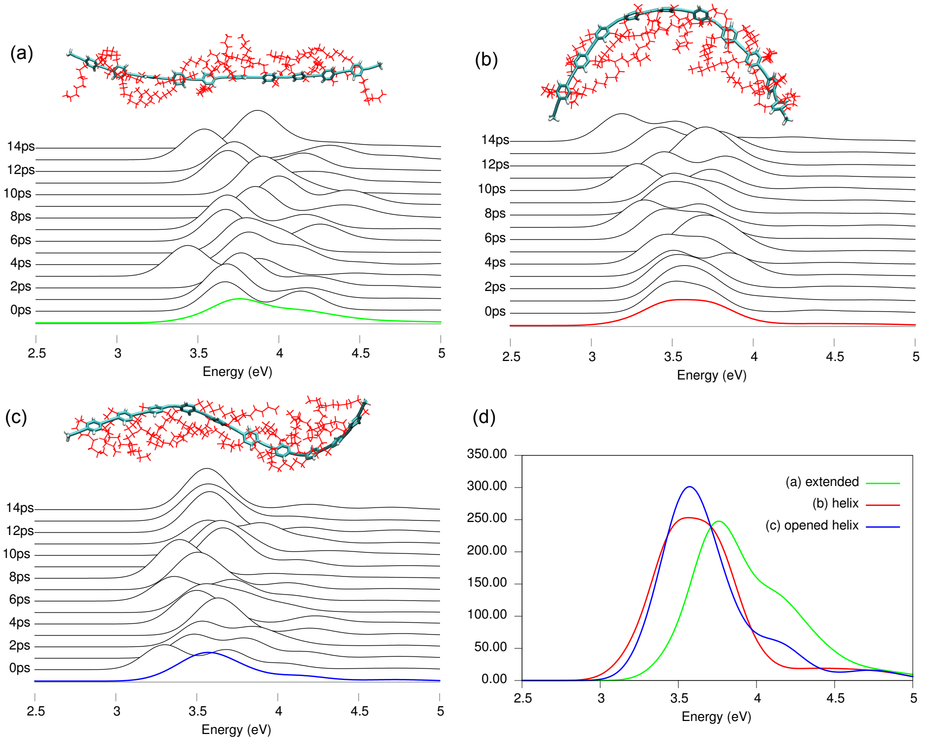

Figure 8.16: Simulated absorption spectra (broadened by Gaussian functions with a FWHM of 0.3 eV) of 10-PPE in water in a static MM environment ($R_2 = 4\,\text{nm}$) with a sampling time step $\Delta t = 1\,\text{ps}$ starting from (a) $t_0 = 114\,\text{ns}$ (b) $t_0 = 138\,\text{ns}$ (c) $t_0 = 151\,\text{ns}$. The average over the fourteen respective snapshots is given in green, red, and blue. The respective starting structure is shown. (d) The average of the respective snapshots of (a) $t_0 = 114\,\text{ns}$ (b) $t_0 = 138\,\text{ns}$ (c) $t_0 = 151\,\text{ns}$.

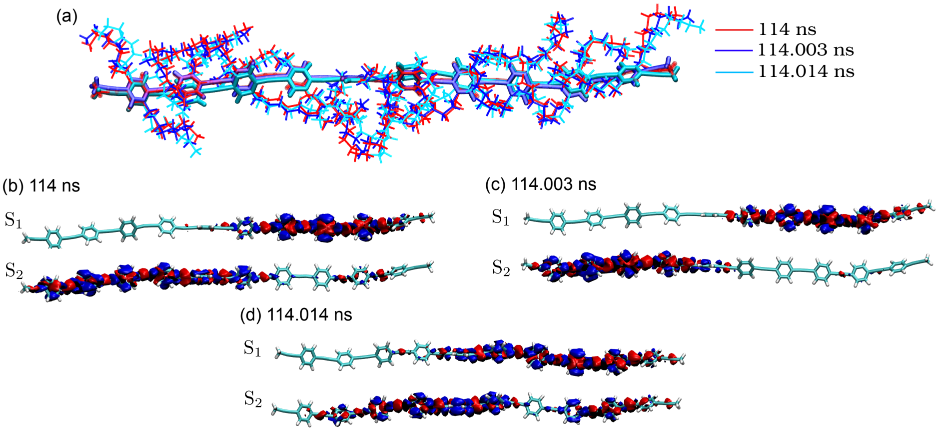

Figure 8.17: (a): The structure of 2,5-dinonyl-10-PPE in water at 114 ns (red), 114.003 ns (blue), and 114.014 ns (cyan). (b), (c), and (d): Analysis of the excited state wave functions for the respective snapshots. Isosurfaces ($\pm 10^{-4} e\text{Å}^{-3}$) of electron (blue) and hole (red) density distribution are shown. The snapshots are chosen with respect to absorption spectra in figure 8.16 (a).

all three starting points. For each of the three starting points, the averages of the respective fourteen snapshots are shown in figure 8.16 with green, red, and blue lines, respectively. The electron-hole wavefunctions of the excitations are sketched in figures 8.17, 8.18, and 8.19 for the three starting points, respectively.

Figure 8.17 shows the isosurfaces for the hole (red) and the electron (blue) density distributions for $t_0 = 114$ ns and (b) $t = 0$ ps, (c) $t = 3$ ps, and (d) $t = 14$ ps. S_1 is the first lowest energy excitation and S_2 is the second lowest energy excitation. Figure 8.17 (a) shows the structure of the polymer at the three respective times. We speculate that the localization characteristic of excitations may be sensitive to the inhomogeneous stress caused by side chains.

Figure 8.18 presents the isosurfaces of electron (blue) and hole (red) density distribution for $t_0 = 138$ ns and (b) $t = 10$ ps, (c) $t = 12$ ps, and (d)$t = 14$ ps. The isosurfaces of electron (blue) and hole (red) density distribution for $t_0 = 151$ ns and (b) $t = 0$ ps, (c)$t = 8$ ps, and (d)$t = 14$ ps are presented in figure 8.19. S_1 and S_2 are the first and the second low energy excitations, respectively. In these cases, the excitations appear to be localized at the apex of the bends. In the bent patterns the co-planarity of the aromatic rings

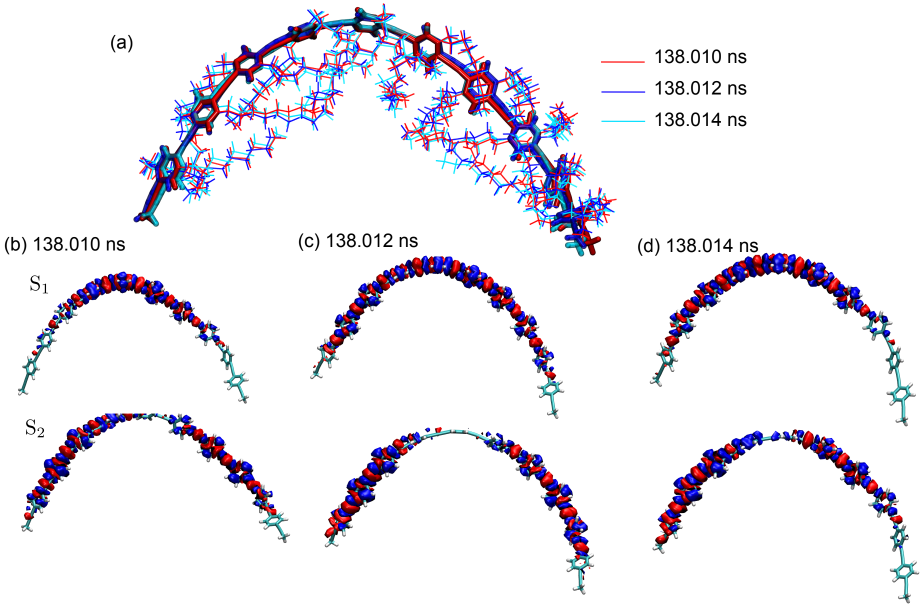

Figure 8.18: (a): The structure of 2,5-dinonyl-10-PPE in water at 138.010 ns (red), 138.012 ns (blue), and 138.014 ns (cyan). (b), (c), and (d): Analysis of the excited state wave functions for the respective snapshots. Isosurfaces ($\pm 10^{-4} e\text{Å}^{-3}$) of electron (blue) and hole (red) density distribution are shown. The snapshots are chosen with respect to absorption spectra in figure 8.16 (b).

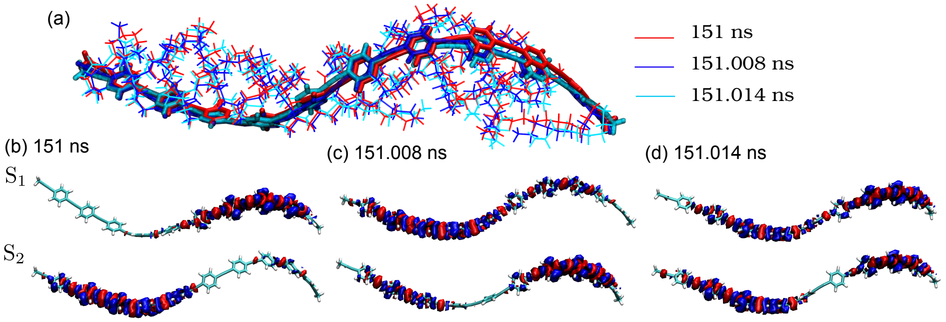

Figure 8.19: (a): The structure of 2,5-dinonyl-10-PPE in water at 151 ns (red), 151.008 ns (blue), and 151.014 ns (cyan). (b), (c), and (d): Analysis of the excited state wave functions for the respective snapshots. Isosurfaces ($\pm 10^{-4} e\text{Å}^{-3}$) of electron (blue) and hole (red) density distribution are shown. The snapshots are chosen with respect to absorption spectra in figure 8.16 (c).

does not change the excitations significantly. The excitation characteristics are delicate to the dynamics of the backbone at the respective times.

8.6 Conclusion

The backbone of 10-PPE with nonyl side chains and with ethylhexyl side chains in toluene remains extended and the side chains are dispersed from each other and from the backbone. In water, 2,5-diethylhexyl-10-PPE forms an overall extended backbone with side chains aggregated toward the backbone. 2,5-dinonyl-10-PPE in water exhibits a distinctive behaviour, from an extended backbone to a bent backbone. A set of structural analysis were performed on the conformations. We conclude that the bent structures of 2,5-dinonyl-10-PPE in water is a result of side chain-water interactions. Due to the stress caused by the side chains, the backbone bends. This effect does not occur in 2,5-diethylhexyl-10-PPE because of shorter length of ethylhexyl side chains (~ 6 Å in a straight form) compared to nonyl ones (~ 11 Å).

From the studies of structure factor for 10-PPE with both side chains in water, we conclude that the backbone in both cases behaves like a rigid rod. Further studies of dihedral distribution and effective potential of mean force for the torsion of phenylene rings along the backbone revealed that the number of rings along the backbone and the interaction between the backbone and water does not change the torsional potential profile. However, due the interaction between side chains and solvent the potential profile changes. As a result, the interaction between side chains and water lead to particular conformational behaviour of 2,5-dinonyl-10-PPE and 2,5-diethylhexyl-10-PPE.

The result of our QM/MM calculation with static environment shows that the position of the peaks and the hight of them are very sensitive to the dynamics of the backbone in all cases. In the bent structures the electron-hole wave function appears to be localized around the apex of the bends in the backbone conformation.

Chapter 9

Conclusions

In this thesis, we focused on modelling the optical properties of a series of conjugated polymers called poly para phenylene ethynylenes (poly-PPE) in complex morphologies. To this end, we used a multiscale approach that allows the analysis of the interplay between morphologies and optical excitations. The underlying challenges were addressed. In the following we present concluding remarks and open problems for future work.

Looking back

The use of classical MD simulations to obtain conformations of polymer chains in solvent is inevitable.

In chapter 6, we addressed the possible incompatibilities in molecular structures obtained from MD in QM/MM calculations.

Atomistic MD (with PCFF*) and DFT calculations were performed to describe the structural properties of diphenylethyne (DPE). With the PCFF* force field is not possible to obtain a correct description of the ground state structure of DPE. To remedy this problem, force field parameters were developed and added to the existing PCFF* force field [48]. The modified force field [48] is able to describe the structure of DPE and methylated-DPE in agreement with DFT results and experimental data.

Since our aim was to obtain optical properties based on MD conformations, the reliabilities of calculated spectra were studied by comparing the results with the corresponding results obtained based on DFT structures. To this end, the GW-BSE method was used to calculate the optical spectrum of methylated-DPE based on the corresponding MD and DFT structures. The results show that the behaviour of the lowest energy excitations follow the same pattern.

Further reliability checks were performed by calculating low energy excitations for n-PPE ($n = 1, 2, ..., 10$) based on the MD structures and DFT structures. We obtained an overall agreement between the two results.

Based on the results of chapter 6, we solvated a 10-PPE in water and toluene. This was the topic of chapter 7. Conformations of solvated 10-PPE with nonyl side chains were obtained from atomistic MD simulations with our modified force field. The conformations of 2,5-dinonyl-10-PPE in toluene exhibited dispersed side chains from the backbone. The backbone forms an extended structure.

The results for the order parameter for the normal of the phenylene rings demonstrate correlations between the torsions of the rings. The obtained conformations were utilized in the mixed QM/MM setup where the QM part is based on GW-BSE method.

The 10-PPE backbone was treated quantum mechanically while the side chains and the solvent molecules belong to MM part. A two layer MM approach was used with cutoffs $R_1 = 2.5\,\mathrm{nm}$ and $R_2 = 4.0\,\mathrm{nm}$ to calculate excitation energies of 2,5-dinonyl-10-PPE in toluene.

Within the R_1 cutoff around the QM part, interactions from atomic partial charges and polarization were taken into account, while within R_2 polarization effects are ignored. The results show that electrostatics and induced polarization is small and therefore, the excitations are unaffected by the environment. Based on this result, we conclude that the environment can have indirect effects on excitations by influencing the backbone and side chain conformations. The calculated absorption spectra in a static environment ($R_1 = 0\,\mathrm{nm}, R_2 = 4\,\mathrm{nm}$) show that the spectral properties are insensitive to the dynamics of the backbone on time scales of 100 fs. Only after 500 fs, fluctuations in the peak positions and heights of the spectra can be observed both in toluene and water. An inspection of the electron-hole wave functions shows that the excitations appear to be localized at the apex of the bend. The bend in the global structure of the backbone appears to be a result of the stress caused by the nonyl side chains. We conclude that the co-planarity of the phenyl rings along the backbone, or the lack of it, does not appear to affect the excitations significantly.

PPE polymers can be purposefully modified, e.g. by the choice of functionalizing side chains and solvent combinations. For a PPE polymer to form a collapsed structure, solvent-side chains interactions are in an important role [20, 19, 21]. As such, two kinds of side chains were considered, nonyl and ethylhexyl. MD simulation for the 10-PPE solvated in water and toluene, respectively, were performed. Structural analyses were performed on the conformations. We conclude that the bent structure of 2,5-dinonyl-10-PPE in water is a result of side chain-water interactions and due to stress caused by the side chains. This effect is less visible in 2,5-diethylhexyl-10-PPE because of shorter ethylhexyl side chains (~ 6 Å in a straight form) compared to nonyl ones (~ 11 Å). Further studies of dihedral distribution and potential of mean force for the torsion of phenylene rings along the bare backbone (10-PPE without side chains), 2,5-dinonyl-10-PPE, and 2,5-diethylhexyl-10-PPE result are the following: the number of rings along the backbone and the interaction between the backbone and water does not change the torsional potential profile. However, due to the interactions between the side chains and solvent the potential profile changes. As a result, the interactions between the side chains and water lead to particular conformational behaviour of 2,5-dinonyl-10-PPE and 2,5-diethylhexyl-10-PPE. The conformations of 2,5-dinonyl-10-PPE in water were used in our QM/MM setup with static environment ($R_1 = 0\,\mathrm{nm}$, $R_2 = 4.0\,\mathrm{nm}$). The results for optical spectrum show that the positions and heights of the peaks are very sensitive to the dynamics of the backbone in all cases. In the bent structures the electron hole wave function appears to be localized around the apex of the bends in the backbone conformation.

Looking ahead

So far, the simulations of 2,5-dinonyl-10-PPE and 2,5-diethylhexyl-10-PPE in water were run in the NpT ensemble for 183 ns and 126 ns, respectively. The two solvents that were used in this thesis are both poor solvents for the side chains. Solvating the PPE polymer in a good solvent and its effects in optical properties can be possible next steps. Furthermore, the effects of different side chains can be considered. In addition, in this thesis we used a PPE with 10 repeating units. The contour length of 10-PPE is very small compared to the estimated persistence length. Therefore, the study of conformational properties of longer chains should be considered. Furthermore, the dynamics of the solvent around the polymer should be studied in more detail. In this thesis, the SPC/E model of water was employed. One could study what are the effects of different water models on conformations and optical properties.

Our result from calculations of optical properties revealed that the electron hole wave functions of lowest energy excitations exhibited a characteristic localization around the apex of the bends in the backbone of PPE. The heights and positions of the peaks are sensitive to the dynamics of the backbone. *Ab intio*/MM simulations suggest a future study of the dynamics of the backbone and the solvent around it more accurately. The obtained conformations can be utilized in the GW-BSE/MM setup for further spectral calculations.

Simulation of polymers in solutions involve physical and chemical phenomena that occur at different length and time scales. For this purpose one could define a region around the polymer to be considered at atomistic resolution. Around this atomistic shell, a coarse grained region is considered. One possibility is to use Adaptive Resolution Simulations [172, 173] (AdResS), which can decrease the computational cost. Within this approach, the resolution of particles change once they pass from atomistic region to a coarse grained region [174].

Considering the aforementioned description about AdResS simulations, strategies can be developed in order to calculate the excitation energies of PPE polymers considering solvents at different levels of resolution. In our setup we only considered solvent molecules within a cutoff R_2 region around the solute. In order to consider the effects of the rest of the solvent, one could develop a hybrid coarse grained, atomistic, quantum mechanical calculations based on the GW-BSE method.

The final goal is to calculate optical properties of polydots made from PPE in complex morphologies considering the effects of solvents. In order to employ our hybrid GW-BSE/MM approach to a ploydot we need to divide the polydot into smaller parts. The whole polydot cannot be described within our GW-BSE calculations. As such, new strategies are required.

Summary

Multiscale Modeling of Excitations in Polymeric Systems

In this thesis we employed a multiscale computational approach in order to model the optical properties of a class of conjugated polymers called poly para phenylene ethynylenes (poly-PPE) in complex morphologies. This approach allows the analysis of the interplay between the morphologies and optical excitations.

The use of classical MD simulations to obtain conformations of polymer chains in solvent is inevitable. In chapter 6, we addressed the possible incompatibilities in molecular structures obtained from MD in QM/MM calculations.

Atomistic MD (with PCFF*) and DFT calculations were performed to describe the structural properties of diphenylethyne (DPE). With the PCFF* force field is not possible to obtain a correct description of the ground state structure of DPE. To remedy this problem, force field parameters were developed and added to the existing PCFF* force field [48]. The modified force field [48] is able to describe the structure of DPE and methylated-DPE in agreement with DFT results and experimental data.

Since our aim was to obtain optical properties based on MD conformations, the reliabilities of calculated spectra were studied by comparing the results with the corresponding results obtained based on DFT structures. To this end, the GW-BSE method was used to calculate the optical spectrum of methylated-DPE based on the corresponding MD and DFT structures. The results show that the behaviour of the lowest energy excitations follow the same pattern. Further reliability checks were performed by calculating low energy excitations for n-PPE ($n = 1, 2, ..., 10$) based on the MD structures and DFT structures. We obtained an overall agreement between the two results.

Based on the results of chapter 6, we solvated a 10-PPE in water and toluene. This was the topic of chapter 7. Conformations of solvated 10-PPE with nonyl side chains were obtained from atomistic MD simulations with our modified force field. The conformations of 2,5-dinonyl-10-PPE in toluene exhibited dispersed side chains from the backbone. The backbone forms an extended structure. The obtained conformations were utilized in the mixed QM/MM setup where the QM part is based on *GW*-BSE method. The 10-PPE backbone was treated quantum mechanically while the side chains and the solvent molecules belong to MM part. A two layer MM approach was used with cutoffs $R_1 = 2.5\,\mathrm{nm}$ and $R_2 = 4.0\,\mathrm{nm}$ to calculate excitation energies of 2,5-dinonyl-10-PPE in toluene.

Within the R_1 cutoff around the QM part, interactions from atomic partial charges and polarization were taken into account, while within R_2 polarization effects are ignored. The results show that electrostatics and induced polarization is small and therefore, the excitations are unaffected by the environment. Based on this result, we conclude that the environment can have indirect effects on excitations by influencing the backbone and side chain conformations. The calculated absorption spectra in a static environment ($R_1 = 0\,\mathrm{nm}, R_2 = 4\,\mathrm{nm}$) show that the spectral properties are insensitive to the dynamics of the backbone on time scales of 100 fs. Only after 500 fs, fluctuations in the peak positions and heights of the spectra can be observed both in toluene and water. An inspection of the electron-hole wave functions shows that the excitations appear to be localized at the apex of the bend. The bend in the global structure of the backbone appears to be a result of the stress caused by the nonyl side chains. We conclude that the co-planarity of the phenyl rings along the backbone, or the lack of it, does not appear to affect the excitations significantly.

PPE polymers can be purposefully modified, e.g. by the choice of functionalizing side chains and solvent combinations. For a PPE polymer to form a collapsed structure, solvent-side chains interactions are in an important role [20, 19, 21]. As such, two kinds of side chains were considered, nonyl and ethylhexyl. MD simulation for the 10-PPE solvated in water and toluene, respectively, were performed. Structural analyses were performed on the conformations. We conclude that the bent structure of 2,5-dinonyl-10-PPE in water is a result of side chain-water interactions and due to stress caused by the side chains. This effect is less visible in 2,5-diethylhexyl-10-PPE because of shorter ethylhexyl side chains ($\sim 6\,\text{Å}$ in a straight form) compared to nonyl ones ($\sim 11\,\text{Å}$). Further studies of dihedral distribution and potential of mean force for the torsion of phenylene rings along the bare backbone (10-PPE without side chains), 2,5-dinonyl-10-PPE, and 2,5-diethylhexyl-10-PPE result are the following: the number of rings along the backbone and the interaction between the backbone and water does not change the torsional potential profile. However, due to the interactions between the side chains and solvent the potential profile changes. As a result, the interactions between the side chains and water lead to particular conformational behaviour of 2,5-dinonyl-10-PPE and 2,5-diethylhexyl-10-PPE. The conformations of 2,5-dinonyl-10-PPE in water were used in our QM/MM setup with static environment ($R_1 = 0\,\text{nm}$, $R_2 = 4.0\,\text{nm}$). The results for optical spectrum show that the positions and heights of the peaks are very sensitive to the dynamics of the backbone in all cases. In the bent structures the electron hole wave function appears to be localized around the apex of the bends in the backbone conformation.

Curriculum Vitae

Behnaz Bagheri Varnousfaderani was born on September 20, 1987 in Iran. She completed her bachelor's degree in physics from Isfahan University of Technology (IUT), Isfahan, Iran in 2009. She obtained her master's degree in Condensed Matter Physics from the same university in 2011. Then she attended the post-graduate diploma programme of ICTP (International Center for Theoretical Physics) in the group of Condensed Matter and Statistical Physics in Trieste, Italy. She received her post-graduate diploma in 2012. She started her PhD in 2013 in the group of prof. dr. Mikko Karttunen at University of Waterloo in Canada. In 2015 she moved to Eindhoven University of Technology (TU/e) in the Centre for Analysis, Scientific computing and Applications (CASA) of the Department of Mathematics and Computer Science. The results of her research are presented in this thesis.

Acknowledgments

> *"If you treat an individual as he is, he will remain how he is.*
> *But if you treat him as if he were what he ought to be and*
> *could be, he will become what he ought to be and could be."*
> *– Johann Wolfgang von Goethe*

In my journey to pursue a PhD degree, I was privileged to work with, and enjoy the support of knowledgeable and indulgent colleagues and warm-hearted and caring friends and family.

First and foremost my deep gratitude goes to Prof. Mikko Karttunen, my promoter, and Dr. Björn Baumeier, my co-promoter, for their continuous patience, motivation, and thoughtful guidance. Mikko, thank you for giving me the opportunity to do my PhD research in your group. Björn, I happened to be your student for a short period of time, but in this time, your guidance had a great impact on me.

I would like to thank all the members of my PhD committee for reading my thesis and their fruitful comments. I feel honoured that you have agreed to referee my thesis.

I wish to express my gratitude to my current and former Softsimu colleagues, especially Trang, Yuriy, Pranav, Jens, it was a pleasure working with you.

I sincerely thank CASA (Centre for Analysis, Scientific Computing, and Applications) and ICMS (Institute for Complex Molecular Systems). I would like to express my gratitude toward Prof. Mark Peletier and Prof. Barry Koren for their support and welcoming me in CASA. Many thanks goes to Enna van Dijk for her help and kindness.

Thanks to my dear friends, Mozhdeh, Sona, Niloufar and Farideh whose friendships are my assets.

Melania, Saeed, Upanshu, and Deepeshe: this thesis would not have been possible without the incredible support and help of you. I cannot put into words how grateful I am. You are all good listeners and fair judges.

I would like to thank all my CASA colleagues for creating such a pleasant working environment. I would like to thank my current and former officemates, Melania, Deepeshe, Thomas, Yuriy, Pranav, Nitin for tolerating me in the office.

It has been less than two years that I am in Eindhoven. During this time I also had the chance to enjoy the “Kabelstraat” events. I cherish all the fun memories and am thankful to the organizers and the members.

On a personal note, I would like to thank my family back in Iran. I am deeply indebted to my loving parents for encouraging me to continue my education. Thanks to my mother for her unconditional love and support. Special thanks to my brothers, Mansour, Saeed, and Davood, for their support and understanding.

Bibliography

[1] G.R. Strobl, *The physics of polymers: concepts for understanding their structures and behavior* (Springer, Berlin; New York, 2007), ISBN 978-3-540-68411-4 978-3-540-25278-8

[2] O.G. Piringer, A.L. Baner, eds., *Plastic packaging: interactions with food and pharmaceuticals*, 2nd edn. (WILEY-VCH, Weinheim, 2008), ISBN 978-3-527-31455-3

[3] H.G. Elias, *An introduction to polymer science*, 1st edn. (VCH, Weinheim, 1997), ISBN 978-3-527-28790-1

[4] W. Salaneck, R. Friend, J. Brédas, Phys. Rep. **319**, 231 (1999)

[5] H.F. Meng, ed., *Polymer Electronics* (Pan Stanford Publishing, Singapore, 2013), ISBN 978-981-4267-84-7 978-981-4364-04-1

[6] J.M. Nunzi, C R Phys. **3**, 523 (2002)

[7] B.S. Gaylord, A.J. Heeger, G.C. Bazan, P. Natl. Acad. Sci. **99**, 10954 (2002)

[8] S.A. Kushon, K.D. Ley, K. Bradford, R.M. Jones, D. McBranch, D. Whitten, Langmuir **18**, 7245 (2002)

[9] B.S. Harrison, M.B. Ramey, J.R. Reynolds, K.S. Schanze, J. Am. Chem. Soc. **122**, 8561 (2000)

[10] D.T. McQuade, A.E. Pullen, T.M. Swager, Chem. Rev. **100**, 2537 (2000)

[11] I.B. Kim, A. Dunkhorst, J. Gilbert, U.H.F. Bunz, Macromolecules **38**, 4560 (2005)

[12] M. Liu, P. Kaur, D.H. Waldeck, C. Xue, H. Liu, Langmuir **21**, 1687 (2005)

[13] F. Hide, M.A. Diaz-Garcia, B.J. Schwartz, M.R. Andersson, Q. Pei, A.J. Heeger, Science **273**, 1833 (1996)

[14] P.K.H. Ho, J.S. Kim, J.H. Burroughes, H. Becker, S.F.Y. Li, T.M. Brown, F. Cacialli, R.H. Friend, Nature **404**, 481 (2000)

[15] C. Zhang, D. Braun, A.J. Heeger, J. Appl. Phys. **73**, 5177 (1993)

[16] P. Kaur, H. Yue, M. Wu, M. Liu, J. Treece, D.H. Waldeck, C. Xue, H. Liu, J. Phys. Chem. B **111**, 8589 (2007)

[17] S. Shaheen, D. Ginley, G. Jabbour, MRS bulletin **30**, 10 (2005)

[18] C.J. Brabec, S. Gowrisanker, J.J.M. Halls, D. Laird, S. Jia, S.P. Williams, Adv. Mater. **22**, 3839 (2010)

[19] C.E. Halkyard, M.E. Rampey, L. Kloppenburg, S.L. Studer-Martinez, U.H.F. Bunz, Macromolecules **31**, 8655 (1998)

[20] C. Wu, B. Bull, C. Szymanski, K. Christensen, J. McNeill, ACS Nano **2**, 2415 (2008)

[21] D. Tuncel, H.V. Demir, Nanoscale **2**, 484 (2010)

[22] H. Yue, M. Wu, C. Xue, S. Velayudham, H. Liu, D.H. Waldeck, J. Phys. Chem. B **112**, 8218 (2008)

[23] N. Vukmirović, L.W. Wang, J. Chem. Phys. **128**, 121102 (2008)

[24] N. Vukmirović, L.W. Wang, Nano Lett. **9**, 3996 (2009)

[25] D.P. McMahon, A. Troisi, Chem. Phys. Lett. **480**, 210 (2009)

[26] Y.H. Chan, C. Wu, F. Ye, Y. Jin, P.B. Smith, D.T. Chiu, Anal. Chem. **83**, 1448 (2011)

[27] G. Onida, L. Reining, A. Rubio, Rev. Mod. Phys. **74**, 601 (2002)

[28] Y. Olivier, L. Muccioli, V. Lemaur, Y.H. Geerts, C. Zannoni, J. Cornil, J. Phys. Chem. B **113**, 14102 (2009)

[29] E. Di Donato, R.P. Fornari, S. Di Motta, Y. Li, Z. Wang, F. Negri, J. Phys. Chem. B **114**, 5327 (2010)

[30] J. Nelson, J.J. Kwiatkowski, J. Kirkpatrick, J.M. Frost, Accounts Chem. Res. **42**, 1768 (2009)

[31] T. Vehoff, B. Baumeier, D. Andrienko, J. Chem. Phys. **133**, 134901 (2010)

[32] T. Vehoff, B. Baumeier, A. Troisi, D. Andrienko, J. Am. Chem. Soc. **132**(33), 11702 (2010)

[33] V. Rühle, J. Kirkpatrick, D. Andrienko, J. Chem. Phys. **132**, 134103 (2010)

[34] L. Wang, G. Nan, X. Yang, Q. Peng, Q. Li, Z. Shuai, Chem. Soc. Rev. **39**, 423 (2010)

[35] M. Schrader, R. Fitzner, M. Hein, C. Elschner, B. Baumeier, K. Leo, M. Riede, P. Baeuerle, D. Andrienko, J. Am. Chem. Soc. **134**, 6052 (2012)

[36] F. May, M. Al-Helwi, B. Baumeier, W. Kowalsky, E. Fuchs, C. Lennartz, D. Andrienko, J. Am. Chem. Soc. **134**, 13818 (2012)

[37] W. Kohn, L.J. Sham, Phys. Rev. **140**, A1133 (1965)

[38] P. Hohenberg, W. Kohn, Phys. Rev. **136**, B864 (1964)

[39] L. Hedin, S. Lundqvist, in *Solid State Physics: Advances in Research and Application* (Academic Press, New York, 1969), Vol. 23, pp. 1–181

[40] Y. Ma, M. Rohlfing, C. Molteni, J. Chem. Theory Comput. **6**, 257 (2010)

[41] B. Baumeier, D. Andrienko, Y. Ma, M. Rohlfing, J. Chem. Theory Comput. **8**, 997 (2012)

[42] B. Baumeier, D. Andrienko, M. Rohlfing, J. Chem. Theory Comput. **8**, 2790 (2012)

[43] X. Blase, C. Attaccalite, Appl. Phys. Lett. **99**, 171909 (2011)

[44] C. Faber, I. Duchemin, T. Deutsch, C. Attaccalite, V. Olevano, X. Blase, J. Mater. Sci. pp. 1–10 (2012)

[45] X. Blase, C. Attaccalite, V. Olevano, Phys. Rev. B **83**, 115103 (2011)

[46] N. Marom, F. Caruso, X. Ren, O.T. Hofmann, T. Körzdörfer, J.R. Chelikowsky, A. Rubio, M. Scheffler, P. Rinke, Phys. Rev. B **86**, 245127 (2012)

[47] M.J. van Setten, F. Weigend, F. Evers, J. Chem. Theory Comput. **9**, 232 (2013)

[48] B. Bagheri, B. Baumeier, M. Karttunen, Phys. Chem. Chem. Phys. **18**, 30297 (2016)

[49] B. Bagheri, M. Karttunen, B. Baumeier, EPJ ST **225**(8), 1743 (2016)

[50] U.H.F. Bunz, Macromol. Rapid Comm. **30**, 772 (2009)

[51] T. Miteva, L. Palmer, L. Kloppenburg, D. Neher, U.H.F. Bunz, Macromolecules **33**, 652 (2000)

[52] F. May, B. Baumeier, C. Lennartz, D. Andrienko, Phys. Rev. Lett. **109**, 136401 (2012)

[53] B. Baumeier, M. Rohlfing, D. Andrienko, J. Chem. Theory Comput. **10**, 3104 (2014)

[54] C. Poelking, M. Tietze, C. Elschner, S. Olthof, D. Hertel, B. Baumeier, F. Würthner, K. Meerholz, K. Leo, D. Andrienko, Nat. Mater. **14**, 434 (2015)

[55] M. Rubinstein, R.H. Colby, *Polymer physics* (Oxford University Press, Oxford ; New York, 2003), ISBN 978-0-19-852059-7

[56] I. Teraoka, *Polymer solutions: an introduction to physical properties* (Wiley, New York, 2002), ISBN 978-0-471-38929-3

[57] A.I. Grosberg, A.R. Khokhlov, P.G.d. Gennes, *Giant molecules: here, there, and everywhere*, 2nd edn. (World Scientific, Hackensack, N.J, 2011), ISBN 978-981-283-922-0

[58] P.J. Flory, M. Volkenstein, Biopolymers **8**, 699 (1969)

[59] W. Kuhn, Kolloid-Zeitschrift **68**, 2 (1934)

[60] P.J. Flory, J. Chem. Phys. **17**, 303 (1949)

[61] P. de Gennes, Phys. Lett. A **38**, 339 (1972)

[62] D. Gupta, J.J. Miller, A. Muralidhar, S. Mahshid, W. Reisner, K.D. Dorfman, ACS Macro Letters **4**, 759 (2015)

[63] M. Doi, S.F. Edwards, *The theory of polymer dynamics*, International series of monographs on physics (Clarendon Press, Oxford, 2007), ISBN 978-0-19-852033-7

[64] P.J. Flory, J. Chem. Phys. **10**, 51 (1942)

[65] M.L. Huggins, J. Chem. Phys. **9**, 440 (1941)

[66] P.E. Rouse, J. Chem. Phys. **21**, 1272 (1953)

[67] B.H. Zimm, J. Chem. Phys. **24**, 269 (1956)

[68] B. Baumeier, PhD Thesis, Universität Münster (2009)

[69] R.M. Martin, *Electronic structure: basic theory and practical methods*, 1st edn. (Cambridge University Press, Cambridge, UK ; New York, 2008), ISBN 978-0-521-53440-6

[70] F. Caruso, PhD Thesis, Universität Berlin (2013)

[71] F. Bruneval, PhD Thesis, École Polytechnique (2005)

[72] M. Born, R. Oppenheimer, Annalen der Physik **389**, 457 ((1927) English version: "On the Quantum Theory of Molecules" translated by S. M. Blinder with emendations by B. Sutcliffe and W. Geppert (2002).)

[73] D.R. Hartree, Math. Proc. Cambridge **24**, 89 (1928)

[74] V. Fock, Zeitschrift für Physik **61**, 126 (1930)

[75] A. Szabo, N.S. Ostlund, *Modern quantum chemistry: introduction to advanced electronic structure theory* (Dover Publications, Mineola, N.Y, 1996), ISBN 978-0-486-69186-2

[76] G. Senatore, N.H. March, Rev. Mod. Phys. **66**, 445 (1994)

[77] W.M.C. Foulkes, L. Mitas, R.J. Needs, G. Rajagopal, Rev. Mod. Phys. **73**, 33 (2001)

[78] J.P. Perdew, Y. Wang, Phys. Rev. B **45**, 13244 (1992)

[79] R.O. Jones, O. Gunnarsson, Rev. Mod. Phys. **61**, 689 (1989)

[80] D.C. Langreth, M.J. Mehl, Phys. Rev. B **28**, 1809 (1983)

[81] J.P. Perdew, K. Burke, M. Ernzerhof, Phys. Rev. Lett. **77**, 3865 (1996)

[82] M. Ernzerhof, G.E. Scuseria, J. Chem. Phys. **110**, 5029 (1999)

[83] A.D. Becke, J. Chem. Phys. **109**, 2092 (1998)

[84] J.P. Perdew, S. Kurth, A. Zupan, P. Blaha, Phys. Rev. Lett. **82**, 2544 (1999)

[85] A.D. Becke, J. Chem. Phys. **98**, 1372 (1993)

[86] J.P. Perdew, M. Ernzerhof, K. Burke, J. Chem. Phys. **105**, 9982 (1996)

[87] J.P. Perdew, A. Zunger, Phys. Rev. B **23**, 5048 (1981)

[88] F. Jensen, *Introduction to computational chemistry*, 2nd edn. (Wiley, Chichester, 2009), ISBN 978-0-470-01187-4 978-0-470-01186-7, oCLC: 608588374

[89] E. Runge, E.K.U. Gross, Phys. Rev. Lett. **52**, 997 (1984)

[90] L. Hedin, Phys. Rev. **139**, A796 (1965)

[91] F. Bechstedt, *Many-Body Approach to Electronic Excitations*, Vol. 181 of *Springer Series in Solid-State Sciences* (Springer Berlin Heidelberg, Berlin, Heidelberg, 2015), ISBN 978-3-662-44592-1 978-3-662-44593-8

[92] V.M. Galitskii, A.B. Migdal, Sov. Phys. **jetp 7** (1958)

[93] J. Hubbard, P. R. Soc. London **240**, 539 (1957)

[94] J. Schwinger, P. Natl. Acad. Sci. **37**, 452 (1951)

[95] M. Rohlfing, Habilitation Thesis, Universität Münster (2000)

[96] A. Corney, *Atomic and laser spectroscopy*, Oxford classic texts in the physical sciences (Clarendon Press, Oxford, 2006), ISBN 978-0-19-921145-6

[97] R.C. Hilborn, Am. J. Phys. **50**, 982 (1982)

[98] D. Frenkel, B. Smit, *Understanding molecular simulation: from algorithms to applications*, Computational science series, 2nd edn. (Academic Press, San Diego, 2002), ISBN 978-0-12-267351-1

[99] M.P. Allen, Computational soft matter: from synthetic polymers to proteins **23**, 1 (2004)

[100] D. Marx, J. Hutter, *Ab initio molecular dynamics: basic theory and advanced methods* (Cambridge University Press, Cambridge ; New York, 2009), ISBN 978-0-521-89863-8

[101] T.N. Do, PhD Thesis, Scuola Internazionale Superiore di Studi Avanzati (SISSA) (2012)

[102] M. Born, V. Fock, Zeitschrift für Physik **51**, 165 (1928)

[103] A.R. Leach, *Molecular modelling: principles and applications*, 2nd edn. (Prentice Hall, Harlow, England ; New York, 2001), ISBN 978-0-582-38210-7

[104] L. Verlet, Phys. Rev. **159**, 98 (1967)

[105] G.A. Cisneros, M. Karttunen, P. Ren, C. Sagui, Chem. Rev. **114**, 779 (2014)

[106] M. Karttunen, J. Rottler, I. Vattulainen, C. Sagui, in *Computational Modeling of Membrane Bilayers*, edited by S.E. Feller (Academic Press, 2008), Vol. 60 of *Current Topics in Membranes*, pp. 49–89

[107] J.A. Barker, R.O. Watts, Mol. Phys. **26**, 789 (1973)

[108] R. Watts, Mol. Phys. **28**, 1069 (1974)

[109] P.P. Ewald, Annalen der Physik **369**, 253 (1921)

[110] C. Sagui, T.A. Darden, Annu. Rev. Bioph. Biom. **28**, 155 (1999)

[111] T. Darden, D. York, L. Pedersen, J. Chem. Phys. **98**, 10089 (1993)

[112] M. Frigo, S.G. Johnson, In Proceedings of the IEEE **93** (2005)

[113] J.W. Gibbs, Am. J. Sci. **s3-16**, 441 (1878)

[114] M.E. Tuckerman, *Statistical mechanics: theory and molecular simulation* (Oxford University Press, Oxford ; New York, 2010), ISBN 978-0-19-852526-4

[115] H.C. Andersen, J. Chem. Phys. **72**, 2384 (1980)

[116] H.J.C. Berendsen, J.P.M. Postma, W.F. van Gunsteren, A. DiNola, J.R. Haak, J. Chem. Phys. **81**, 3684 (1984)

[117] S. Nosé, J. Chem. Phys. **81**, 511 (1984)

[118] W.G. Hoover, Phys. Rev. A **31**, 1695 (1985)

[119] G. Bussi, D. Donadio, M. Parrinello, J. Chem. Phys. **126**, 014101 (2007)

[120] G.S. Grest, K. Kremer, Phys. Rev. A **33**, 3628 (1986)

[121] M. Parrinello, A. Rahman, Phys. Rev. Lett. **45**, 1196 (1980)

[122] M. Parrinello, J. Appl. Phys. **52**, 7182 (1981)

[123] A. Warshel, M. Levitt, J. Mol. Biol. **103**, 227 (1976)

[124] G. Monard, K.M. Merz, Accounts Chem. Res. **32**, 904 (1999)

[125] A.J. Stone, *The theory of intermolecular forces*, second edition edn. (Oxford University Press, Oxford, 2013), ISBN 978-0-19-967239-4

[126] C.M. Breneman, K.B. Wiberg, J. Comput. Chem. **11**, 361 (1990)

[127] J. Applequist, J.R. Carl, K.K. Fung, J. Am. Chem. Soc. **94**, 2952 (1972)

[128] L. Silberstein, Philosophical Magazine Series 6 **33**, 521 (1917)

[129] B. Thole, Chem. Phys. **59**, 341 (1981)

[130] P.T. van Duijnen, M. Swart, J. Phys. Chem. A **102**, 2399 (1998)

[131] W.L. Jorgensen, J.D. Madura, C.J. Swenson, J. Am. Chem. Soc. **106**, 6638 (1984)

[132] W.L. Jorgensen, D.S. Maxwell, J. Tirado-Rives, J. Am. Chem. Soc. **118**, 11225 (1996)

[133] E.K. Watkins, W.L. Jorgensen, J. Phys. Chem. A **105**, 4118 (2001)

[134] D. Van Der Spoel, E. Lindahl, B. Hess, G. Groenhof, A.E. Mark, H.J.C. Berendsen, J. Comput. Chem. **26**, 1701 (2005)

[135] H. Sun, S.J. Mumby, J.R. Maple, A.T. Hagler, J. Am. Chem. Soc. **116**, 2978 (1994)

[136] H. Sun, Macromolecules **28**(3), 701 (1995)

[137] S. Maskey, N.C. Osti, D. Perahia, G.S. Grest, ACS Macro Letters **2**, 700 (2013)

[138] S. Maskey, F. Pierce, D. Perahia, G.S. Grest, J. Chem. Phys. **134**, 244906 (2011)

[139] U. Essmann, L. Perera, M.L. Berkowitz, T. Darden, H. Lee, L.G. Pedersen, J. Chem. Phys. **103**, 8577 (1995)

[140] A.D. Becke, J. Chem. Phys. **98**, 5648 (1993)

[141] C. Lee, W. Yang, R.G. Parr, Phys. Rev. B **37**, 785 (1988)

[142] S.H. Vosko, L. Wilk, M. Nusair, Can. J. Phys. **58**, 1200 (1980)

[143] P.J. Stephens, F.J. Devlin, C.F. Chabalowski, M.J. Frisch, J. Phys. Chem. **98**, 11623 (1994)

[144] F. Weigend, R. Ahlrichs, Phys. Chem. Chem. Phys. **7**, 3297 (2005)

[145] F. Neese, Wiley Interdisciplinary Reviews: Computational Molecular Science **2**, 73 (2012)

[146] S. Grimme, J. Comput. Chem. **27**, 1787 (2006)

[147] A. Bergner, M. Dolg, W. Küchle, H. Stoll, H. Preuss, Mol. Phys. **80**, 1431 (1993)

[148] R. Krishnan, J.S. Binkley, R. Seeger, J.A. Pople, J. Chem. Phys. **72**, 650 (1980)

[149] Y. Ma, M. Rohlfing, C. Molteni, Phys. Rev. B **80**, 241405 (2009)

[150] V. Rühle, A. Lukyanov, F. May, M. Schrader, T. Vehoff, J. Kirkpatrick, B. Baumeier, D. Andrienko, J. Chem. Theory Comput. **7**, 3335 (2011)

[151] W. Humphrey, A. Dalke, K. Schulten, J. Mol. Graphics **14**, 33 (1996)

[152] Jmol: an open-source Java viewer for chemical structures in 3D. `http://www.jmol.org/`

[153] J.K. Young, J.S. Moore, in *Modern Acetylene Chemistry*, edited by P.J. Stang, F. Diederich (Wiley-VCH Verlag GmbH, Weinheim, Germany, 1995), pp. 415–442, ISBN 978-3-527-61527-8 978-3-527-29084-0

[154] S. Toyota, Chem. Rev. **110**, 5398 (2010)

[155] K. Okuyama, T. Hasegawa, M. Ito, N. Mikami, J. Phys. Chem. **88**, 1711 (1984)

[156] J.P. Ryckaert, A. Bellemans, Faraday Discussions of the Chemical Society **66**, 95 (1978)

[157] H.J.C. Berendsen, J.R. Grigera, T.P. Straatsma, J. Phys. Chem. **91**, 6269 (1987)

[158] J. Wong-ekkabut, M. Karttunen, BBA Biomembranes (2016)

[159] D. Perahia, R. Traiphol, U.H.F. Bunz, Macromolecules **34**, 151 (2001)

[160] H. Kong, G. He, Mol. Simulat. **41**, 1060 (2015)

[161] A. Hariharan, J.G. Harris, J. Chem. Phys. **101**, 4156 (1994)

[162] N. Reuter, A. Dejaegere, B. Maigret, M. Karplus, J. Phys. Chem. A **104**, 1720 (2000)

[163] F. Eisenhaber, P. Lijnzaad, P. Argos, C. Sander, M. Scharf, J. Comput. Chem. **16**, 273 (1995)

[164] A. Lukyanov, A. Malafeev, V. Ivanov, H.L. Chen, K. Kremer, D. Andrienko, J. Mater. Chem. **20**, 10475 (2010)

[165] W. Zhang, E.D. Gomez, S.T. Milner, Macromolecules **47**, 6453 (2014)

[166] G. Jeschke, M. Sajid, M. Schulte, N. Ramezanian, A. Volkov, H. Zimmermann, A. Godt, J. Am. Chem. Soc. **132**, 10107 (2010)

[167] A. Godt, M. Schulte, H. Zimmermann, G. Jeschke, Angew. Chem. Int. Edit. **45**, 7560 (2006)

[168] P.M. Cotts, T.M. Swager, Q. Zhou, Macromolecules **29**, 7323 (1996)

[169] A.V. Shvetsov, A.E. Schmidt, D.V. Lebedev, V.V. Isaev-Ivanov, Journal of Surface Investigation. X-ray, Synchrotron and Neutron Techniques **7**, 1124 (2013)

[170] S.K. Ghosh, Il Nuovo Cimento D **4**, 229 (1984)

[171] S. Wijesinghe, S. Maskey, D. Perahia, G.S. Grest, J. Polym. Sci., Part B: Polym. Phys. **54**, 582 (2016)

[172] M. Praprotnik, L. delle Site, K. Kremer, Ann. Rev. Phys. Chem. **59**, 545 (2008)

[173] M. Praprotnik, L. Delle Site, K. Kremer, J. Chem. Phys. **123**, 224106 (2005)

[174] K. Kreis, R. Potestio, K. Kremer, A.C. Fogarty, J. Chem. Theory Comput. **12**, 4067 (2016)